Raman and Luminescence Investigation of Rare Earth Doped Ferroelectric Crystals and Laser-Induced Crystals-in-Glass

by

Brian Knorr

A Dissertation

Presented to the Graduate Committee

of Lehigh University

in Candidacy for the Degree of

Doctor of Philosophy

in

Physics

Lehigh University

September 2014

Approved and recommended for acceptance as a dissertation in partial fulfillment of the requirements for the degree of Doctor of Philosophy.

Brian Knorr
Raman and Luminescence Investigation of Rare Earth Doped Ferroelectric Crystals and Laser-Induced Crystals-in-Glass

Date

Dr. Volkmar Dierolf, Dissertation Director, Chair

Accepted Date

Committee Members

Dr. Himanshu Jain

Dr. Ivan Biaggio

Dr. Michael Stavola

Dr. Jean Toulouse

Acknowledgements

I would like to thank my advisor, Professor Volkmar Dierolf, for providing me the opportunity to undertake research in his group, through which I was able to participate in a variety of research topics and utilize a number of different techniques. Professor Dierolf was a great source of support, motivation, and guidance while still allowing me to figure things out for myself. His perspective on both my particular research and other general issues were quite valuable and often entertaining.

I am thankful to Professor Himanshu Jain, whose knowledge of crystallization of glass and collaboration with Kyoto University made the bulk of this project possible. I also thank the final members of my committee: Dr. Ivan Biaggio, Dr. Michael Stavola, and Dr. Jean Toulouse for taking time out of their busy schedules to guide my research.

I thank the following funding sources for financially supporting this work: the US Department of Education GAANN program, the National Science Foundation (NSF-DMR 0906763), and the International Materials Institute for New Functionality in Glass (NSF-DMR 0844014).

I am intensely grateful to Dr. Greg Stone, Dr. Adam Stone, and Dr. Dmytro Savytskyy for their contributions towards my education and research. Greg was an all around great guy and an excellent source of guidance concerning Raman spectroscopy and other laboratory techniques, as well as advice concerning research in general. Adam is responsible for the significant progress in the understanding of femtosecond laser-induced crystallization made in the last five years and his wealth of expertise in glass preparation, laser irradiation, and crystal growth dynamics were invaluable to the completion of this research. Similarly, Dmytro's tenacity in the area of CW laser crystallization of chalcogenide glasses was an inspiration, and I learned a great deal of glass science from our discussions of his many papers.

I give thanks to Dr. Brandon Mitchell for his camaraderie, assistance, and support in the office, lab, and softball field. Additionally, I thank him for dragging me to the gym as

often as he was able to overcome my protestations. Thanks are also due to Dr. Carl Faust for introducing me to the joy of launching cantaloupes using pneumatic devices. I also owe many thanks to Carl, as well as to Josh Jones, Massooma Pirbhai, and Ling Cai, for their homework assistance and overall friendship during the past five years.

Finally, I convey my deepest gratitude upon my parents and brother, as well as my amazing wife, for their love, patience, support, and sacrifice throughout this endeavor. I dedicate this dissertation to them.

Contents

List of Tables

List of Figures

Abstract

Rare earth-doped ferroelectric crystals are an interesting and important class of materials due to their wide array of favorable properties. These properties make them attractive for many different applications. However, as smaller, better-performing devices are sought after, novel processes for engineering optical materials must be developed and understood. Additionally, the response of the desirable properties to a reduction in size, and to the fabrication techniques, must be quantified and controlled. This work is aimed at advancing the understanding of two of these materials, namely lithium niobate ($LiNbO_3$) and lanthanum borogermanate ($LaBGeO_5$), and their properties via the development and utilization of multifaceted measurement techniques.

In $LiNbO_3$, Raman spectra collected continuously during application of an external electric field reveal two different effects: (1) the energies of the Raman modes shift linearly in response to the electric field because of the distortion of the crystal via the piezoelectric effect and (2) the zero-field frequencies of the Raman modes are shifted following ferroelectric domain inversion. The former effect may be used as a calibration in order to quantify different phenomenon which produce internal electric fields. The latter effect is due to the presence of polar defects whose dipole moment does not flip during domain inversion. Using effect (1) to quantify effect (2) forces the conclusion that additional polar defects with dipole moment components orthogonal to the spontaneous polarization must exist. This finding has important consequences for the understanding of domain inversion. In a separate set of experiments, space charge fields were produced in $LiNbO_3$ by laser-

induced photoionization of defects at low temperature, and observed via energy shifts of both Raman modes and the erbium fluorescence emission. Occasional electrical breakdown resulted in discharging of these space charge fields. These breakdowns are seemingly random and occur inconsistently, and therefore multiple parameters were investigated in order to determine those responsible.

In $LaBGeO_5$, low temperature Combined Excitation Emission Spectroscopy (CEES) revealed that erbium incorporates into both glass-ceramics and laser-induced crystals-in-glass in predominantly one type of environment (site). However, other minority sites were also observed. The energy levels of the primary site were quantified. The fluorescence characteristics of the erbium ions in any site in the laser-induced crystals were found to be only weakly influenced by the irradiation conditions during growth. On the other hand, a hidden parameter, potentially boron deficiency-related defects, resulted in a significant change of the relative numbers of erbium ions incorporating at the minority sites compared to at the primary site.

Scanning confocal Raman spectroscopy showed that the energies of the Raman modes are shifted across the cross-sections of laser-induced crystals in glass. The source of these shifts is potentially strain due the sharp temperature gradient during the laser-induced crystallization process. Fluorescence spectra collected simultaneously with Raman spectra, which for erbium is possible using a single fixed-wavelength excitation source with a wavelength of $488nm$, showed that the erbium fluorescence intensity is inhomogeneous over the crystal cross-section, despite the host glass being homogeneously doped. These fluctuations were spatially correlated with small shifts in the Raman spectra, which implies that changes to the structure shift the absorption peaks of the erbium sites either toward or away from the energy of the probe laser. Finally, Raman and fluorescence spectra from laser-induced crystals in a $LaBGeO_5$ glass prepared prior to this work exhibited anomalous behavior, including evidence of strong elemental diffusion at the center of the crystal

cross-section which resulted in the crystallization of an unknown $LaBGeO_5$ subphase.

Chapter 1

Introduction

1.1 Motivation for this work

The development of compact multifunctional photonic devices and integrated circuits, which can simultaneously provide the functionality of multiple optical components such as waveguides, splitters, modulators, filters, and amplifiers, is one of the most important steps as the telecommunications and computing industries strive toward smaller, faster, more energy-efficient, more reliable, and lower cost systems and devices. In order to meet these challenges, nonlinear optical ferroelectric crystals must be custom-tailored and engineered with extreme precision. As such, the properties of these crystals, as well as the influences of the fabrication processes and utilization conditions thereon, must be better understood.

This thesis addresses two different facets of this challenge. First, the role of localized internal electric fields due to polar defects in $LiNbO_3$ with respect to the threshold coercive field required for ferroelectric domain inversion, and to the fluorescence properties, is an important area of study due to the consequences for potential applications. Second, one- and multi-photon absorption of ultrafast femtosecond pulsed lasers is a novel fabrication technique capable of inducing highly localized structural changes inside transparent materials, thus enabling the creation of 3D integrated photonic architectures.

While the very early literature concerning femtosecond laser-induced crystallization

was primarily proof-of-concept in nature, more recent work has been directed toward both a deeper understanding of the crystallization mechanism and growth dynamics, and pushing the technique closer to practical applicability [5]. Nevertheless, while ferroelectricity and optical nonlinearity are important properties, even more functionality may be added via rare earth doping of these crystals, allowing them to be used as optical gain media for laser applications. To this point, no systematic studies of the optical properties of laser-induced crystals in rare earth doped glasses have been performed.

1.2 General objectives of this work

The objectives of this work are to answer, using *in situ* Raman spectroscopy during application of an external electric field or spatially resolved simultaneous scanning confocal Raman and fluorescence spectroscopy, the following questions:

1. What is the magnitude of the internal electric field resulting from defects related to lithium vacancies in $LiNbO_3$?

2. How does the defect concentration affect the domain inversion process?

3. What is the nature of the laser-induced space charge field due to photoionization of Fe^{2+} and Nb^{4+} defects in $LiNbO_3$ at low temperature?

4. What conditions allow and/or cause the electrical breakdown responsible for the occasional discharging of this space charge field?

5. What are the incorporation characteristics and fluorescence properties of erbium when doped in $LaBGeO_5$ glass and polycrystalline glass-ceramics?

6. How are these properties altered by the laser-induced crystallization process?

7. How is the crystalline structure across the crystal cross-section influenced by the thermal gradient and other irradiation parameters during the laser-induced crystallization process?

8. Do spatial fluctuations of the structure result in corresponding changes to the erbium incorporation and fluorescence?

Chapter 2

Fundamentals

2.1 Properties of lithium niobate ($LiNbO_3$)

Historically, $LiNbO_3$ is a well studied material system whose properties are well summarized by Weis and Gaylord [7]. As such, only those relevant to the work presented in subsequent chapters will be discussed here.

Lithium niobate is an important optical material with many favorable properties which allow it to be utilized in a wide range of applications. In particular, $LiNbO_3$ is broadly transparent from $350nm$ to $5\mu m$, and is an optically nonlinear and ferroelectric crystal that exhibits large pyroelectric, piezoelectric, acousto-optical, and electro-optical coefficients. These properties allow $LiNbO_3$ to be used in electro-optic and acousto-optic modulators, domain engineered devices for optical frequency conversion, and pyroelectric detectors [8]. Additionally, dopants such as titanium or erbium add significant functionality to $LiNbO_3$ in the form of low-loss waveguides and integrated lasers, respectively [8].

Below the Curie temperature ($T_C \approx 1210^\circ C$), $LiNbO_3$ transitions from a paraelectric phase to a ferroelectric phase due to displacement of the lithium and niobium ions along the c-axis from their symmetric positions in the paraelectric phase. The Li^+ ions are shifted $72pm$ along the c-axis from the plane of the nearest oxygen layer and the Nb^{5+} ions are shifted $26pm$ from the geometric center of their respective surrounding oxygen octahedra.

This results in an asymmetric charge distribution and a permanent electric dipole moment parallel to the c-axis. The direction of this polarization can be reversed if the lithium and niobium ions are displaced in the opposite direction. In order to achieve this reversal, an electric field whose magnitude exceeds the coercive threshold must be applied antiparallel to the spontaneous polarization. This process is frequently referred to as domain inversion or poling. The magnitude of the coercive field required for domain inversion depends primarily on the stoichiometry of the crystal, and, to a lesser extent, the thermal history of the sample. The structure of $LiNbO_3$ in the ferroelectric phase is illustrated in Figure 2.1.

In this regard, $LiNbO_3$ presents significant variability due to its affinity toward lithium deficiency. This affinity makes growing stoichiometric crystals difficult and results in a significant number of intrinsic defects in the form of lithium vacancies. Traditional growth techniques are able to grow $LiNbO_3$ crystals with a ratio of Li/Nb equal to 0.942, instead of the expected value of 1. Attempting to compensate for this phenomenon by adding extra lithium to the melt does not offer significant improvement to the final composition of the crystal. For this reason much effort was expended to develop techniques capable of producing crystals closer to the stoichiometric composition. These techniques include the double crucible Czochralski [9], postgrowth vapor transport equilibration treatment [10], and the top-seeded solution growth [11] methods. However, although these techniques bring the Li/Nb ratio very close to 1, lithium vacancies remain present in the crystal.

The structure of lithium vacancy related defects in $LiNbO_3$ has been studied by X-ray and neutron scattering techniques [12–14] and modeled using density functional theory calculations [15]. These works confirmed that the predominant lithium vacancy defect consists of a niobium atom at a lithium site surrounded by four vacant lithium sites, as was initially suggested by Lerner *et al.* [16]. This arrangement results in an electric dipole moment parallel to the ferroelectric axis of the crystal which interacts with the spontaneous dipole moment produced by the displacements of lithium and niobium atoms.

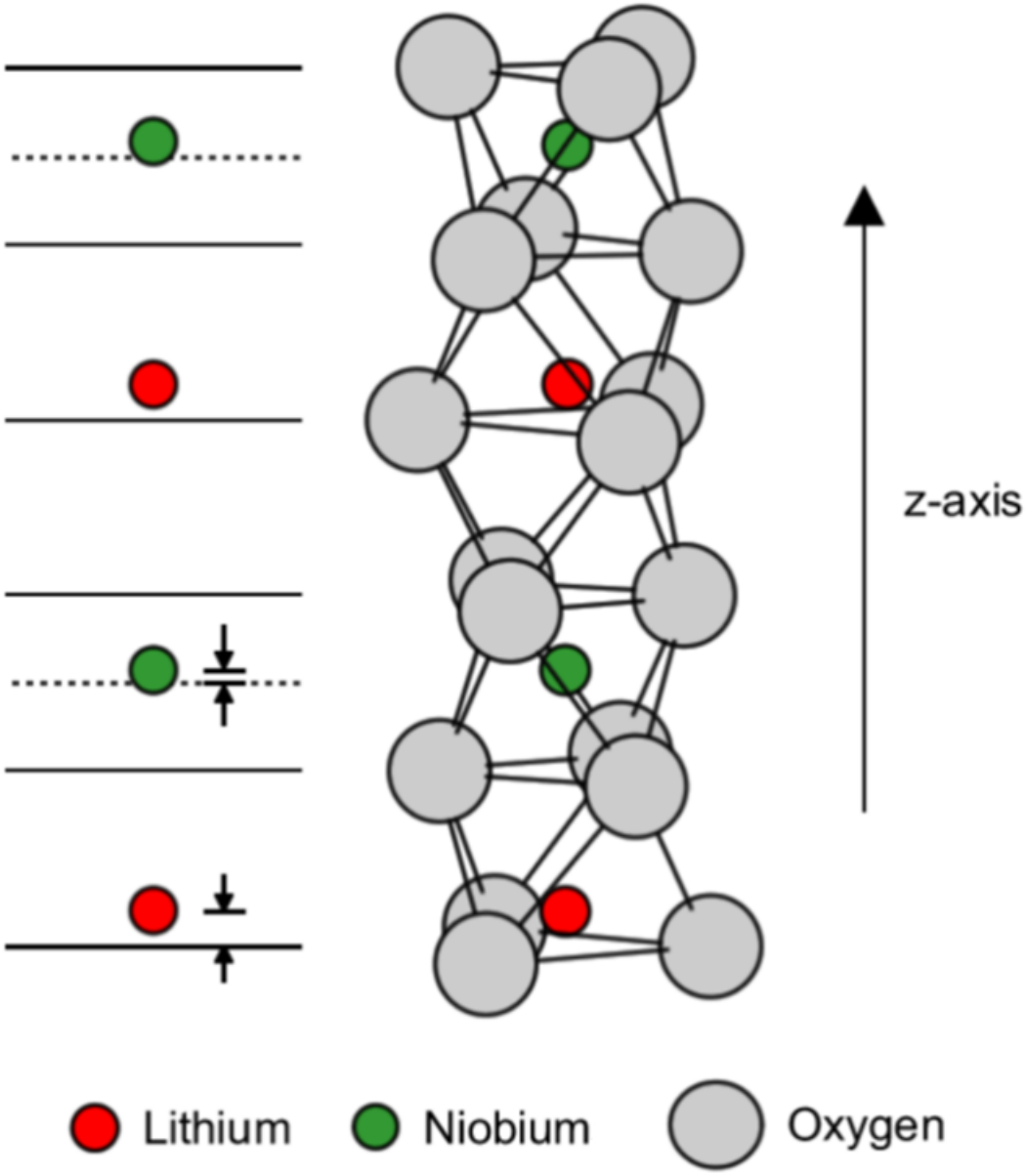

Figure 2.1: Structure of lithium niobate in the ferroelectric phase. Reproduced from G. Stone [3].

Many of the aforementioned desirable properties are dependent on the domain inversion process. Furthermore, domain inversion, as well as some properties in general, are sensitive to both the intrinsic defects, such as lithium vacancies, and extrinsic defects, such as iron or erbium dopants, present the crystal structure. As such, these defects are of significant interest, and the results of various experiments designed to probe their effects are described in Chapter 4.

2.2 Properties of lanthanum borogermanate ($LaBGeO_5$)

2.2.1 Crystal

Crystalline lanthanum borogermanate is an interesting optical material that possesses the stillwellite (Ce, La, Ca)$BSiO_5$ structure [17]. Single crystals are typically grown by the Czochralski method [18] and exhibit low dielectric permittivity ϵ [19], low conductivity σ [19], a high pyroelectric coefficient $\gamma = \frac{P_s}{\Delta T} \sim 5 nC/cm^2K$ [20], and a second harmonic generation efficiency of $\sim$30 units of α-quartz [20]. Notable applications of $LaBGeO_5$ include self-frequency doubling Nd^{3+}-doped lasers [18, 21] and substrates for growing high-quality InN crystalline thin films [22].

$LaBGeO_5$ exhibits a phase transition at its Curie temperature of $530^{\circ}C$ [17]. This transition has been shown to consist primarily of a 2^{nd} order (displacive) transition, while also exhibiting to a lesser extent 1^{st} order (order-disorder) characteristics [17, 23, 24]. Both the low and high temperature phases are noncentrosymmetric trigonal-pyramidal systems. The structure of $LaBGeO_5$ is illustrated in Figure 2.2 and consists of a helical chain of corner-connected BO_4 tetrahedra parallel to the three-fold screw axis in which every three tetrahedra form a ring in the spiral. GeO_4 tetrahedra are connected outside of the spiral to the remaining free vertices of each adjacent BO_4 tetrahedra and to the lanthanide polyhedra. The La ions sit in irregular 9-coordinated polyhedra which interconnect the spiral chains

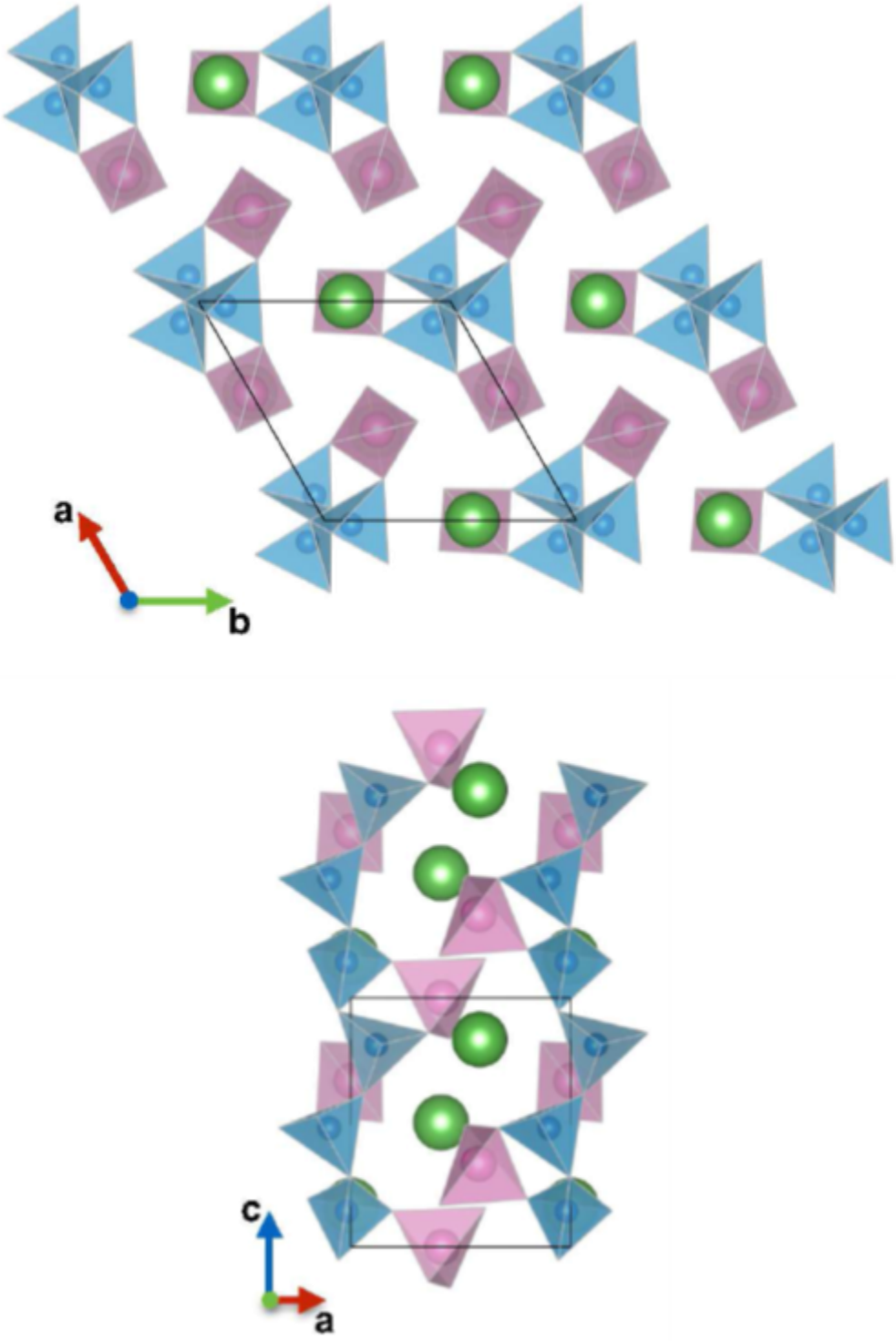

Figure 2.2: Structure of lanthanum borogermanate. La atoms are in green, Ge tetrahedra in pink, and B tetrahedra in blue. Reproduced from Shaltaf *et al.* [4].

[4, 5, 25].

The high temperature phase is paraelectric and in the non-polar space group $P3_121$ (D_3^4) [25]. As the temperature decreases below the Curie temperature, the structure transitions to the polar space group $P3_1$ (C_3^2) [25]. In this phase BO_4 teterahedra are displaced along the z-axis from their positions in the $P3_121$ configuration, resulting in a spontaneous polarization along the [001] axis [23]. This polarization makes $LaBGeO_5$ ferroelectric. At room temperature the spontaneous polarization is approximately $12\mu C/cm^2$ [23].

At room temperature the lattice parameters are $a = 7.0018$Å and $c = 6.8606$Å [17]. Interestingly, as the temperature increases up to the Curie temperature, the c- and a- axes undergo positive and negative linear thermal expansion, respectively [17]. Above the Curie temperature, both axes expand with increasing temperature. The ferroelectric phase has four non-zero nonlinear optical coefficients, d_{11}, d_{22}, d_{33}, and d_{31}, equal to 1.7, -0.6, 1.3, and -0.9pm/V, respectively [26].

2.2.2 Glass

$LaBGeO_5$ glass is optically transparent and can be formed via the standard melt-quenching technique. Sigaev *et al.* [27] studied the effect of slight variations of the composition on the glass-forming ability of $LaBGeO_5$ and found that all of the compositions formed glass easily, though the most lanthanum-rich samples required a higher melting temperature and faster quenching. Importantly, boron-deficient glass compositions lying in the region of the glass formation zone where both $LaBGeO_5$ and $La_2Ge_2O_7$ coexist were found to crystallize to only the stillwellite $LaBGeO_5$ phase. Related to this is the potential difficulty due to the fact that boron oxide is particularly volatile [28, 29]. However, lanthanum oxide was found to suppress the loss of B_2O_3 to only 1.9wt% [27].

For the stoichiometric composition the glass transition temperature, T_g, is approximately $670°C$ [27, 30]. The crystallization onset and peak temperatures for bulk glasses

are 851°C and 902°C, respectively [30]. The coefficient of thermal expansion of the glass, α_g = 76 $\times$ $10^{-7}K^{-1}$, is only slightly different from that of the single crystal, α_c = 65 $\times$ $10^{-7}K^{-1}$ [27].

2.2.3 Rare earth doping

Rare earth doping of $LaBGeO_5$ in both the glassy and crystalline phases has been a topic of interest for the past three decades, particularly in the pursuit of efficient and novel gain media for self-frequency-doubled lasers. Indeed, continuous wave laser radiation using $LaBGeO_5$:Nd^{3+} has been achieved by Capmany *et al.* [31]. However, in general, rare earth doping of $LaBGeO_5$ tends to complicate the situation by altering the structure and, in turn, the crystallization process.

As discussed earlier, $LaBGeO_5$ possesses the stillwellite structure. As lanthanides with higher atomic numbers and smaller atomic radii are added, the structure changes. For La $\rightarrow$ Pr, Nd (low-temperature phase), the structure remains hexagonal (stillwellite). On the other hand, for Nd (high-temperature phase) $\rightarrow$ Er, the structure becomes monoclinic (datolite, isostructural with $CaBSiO_4(OH)$) [17, 32, 33]. The datolite structure is centrosymmetric in the space group $P2_{1/a}$. For the monoclinic phase, the lattice parameters were determined to be $a = 9.80 - 10.03$Å, $b = 7.42 - 7.60$Å, and $c = 4.79 - 4.96$Å, depending on which lanthanide was used [33]. Earlier studies for Tm, Yb, and Lu found that the monoclinic phase did not form, but rather $Ln_2Ge_2O_7$ with a total loss of B_2O_3 [33]. However, a recent study by Zhang *et al.* [34] showed incorporation in $LaBGeO_5$ of Tb^{3+} and Tm^{3+}. Interestingly, these materials exhibited forbidden electric-dipole transitions, suggesting a lack of a center of symmetry. As expected, the dopant ions replace the La^{3+} at one center [18], which in the stillwellite phase has a local symmetry of C_1. As the radii of the dopants decrease, their coordination in $LaBGeO_5$ decreases from 9 to 8, and the surrounding oxygen atoms form a distorted cube [32]. In this case the single point symmetry of the rare earth ion can be

either C_1 or C_i.

Of particular interest for this work are Nd, Pr, and Er. The most detailed analysis of the electronic and optical properties, including tabulation of the energies of the Stark levels, of single crystal rare earth doped $LaBGeO_5$ exists for Nd^{3+} and Pr^{3+} [18]. Less work has been performed on Er:$LaBGeO_5$, though Malashkevich *et al.* did investigate the effects of composition on the lifetimes and quantum yield of the ${}^4I_{13/2} \rightarrow {}^4 I_{15/2}$ transition following non-radiative decay from the ${}^4I_{11/2}$ energy level in $LaBGeO_5$ glasses [35]. According to the work by Malashkevich, the quantum yield for low concentrations of erbium can be approximately 18%, with deactivation via excitation energy exchange into antisymmetric stretching vibrations of boron tetrahedra at $\nu \approx 940 cm^{-1}$ and $1450 cm^{-1}$. For higher dopant concentrations, significant and unexpected quenching was observed and is potentially related to vibrations of impurity OH-groups at $\nu \approx 2270 cm^{-1}$ and $2630 cm^{-1}$ [35].

2.3 Raman spectroscopy

Raman spectroscopy is a powerful tool with which to investigate the structural properties of a material, and as such was one of the primary techniques used in this work. Therefore, an understanding of the principles of Raman spectroscopy is beneficial. Raman spectroscopy is used to probe the vibrational energy levels of a material system, which are dependent upon the types of bonds between constituent atoms, the positions of particular atoms within the lattice, and the different isotopes of the elements in a material. Thus, every material system presents a unique Raman spectrum. Furthermore, small changes to the structure resulting from crystal defects, strain, or an applied electric field (for piezoelectric materials) will alter the vibrational energy levels and may therefore be observed through frequency shifts and/or broadening of the corresponding Raman modes.

Though there are a variety of Raman scattering processes, normal, or non-resonant,

Raman scattering begins with a photon which is incident on a material but does not have enough energy to excite a transition between the material's electronic levels. Instead, the electronic system is briefly excited into a "virtual" state before quickly relaxing back to the electronic ground state. During this process, quanta of energy, $E = \hbar\omega_m\Delta\nu$, where ω_m is the frequency of the m^{th} vibrational mode, and ν is the vibrational quantum number, are transferred between the incident photon and the lattice of the material. Because of the anharmonicity of the electronic potentials, transitions with $\Delta\nu = \pm n$, where n is any integer, are allowed. However, it should be noted that transitions to non-adjacent levels are only weakly allowed. Therefore, the overwhelming majority of transitions occur between states that satisfy the condition $\triangle\nu = \pm 1$. At room temperature, transitions between $\nu = 0$ and $\nu = 1$ dominate due to the fact that they are the most populated according to the Maxwell-Boltzmann distribution law,

$$\frac{N_{\nu=1}}{N_{\nu=0}} = e^{-\Delta E/k_B T},$$

where k_B is the Boltzmann constant, and $N_{\nu=0}$ and $N_{\nu=1}$ are the number of molecules in the ground and first excited vibrational states, respectively.

The relaxation processes from the virtual states that result in Raman scattering therefore predominantly occur in two ways. If the system begins in the ground vibrational state, it will end up in the first excited vibrational state. As a result, the system gains some energy and the scattered photon has less energy than the incident photon. This process is called Stokes scattering. The reverse process, known as Anti-Stokes scattering, involves the molecule beginning in the first excited vibrational level before excitation and relaxation into the ground state upon inelastic scattering of the incident photon. The scattered photon in this case has more energy than the incident photon. These processes, as well as others used to study vibrational energy levels, are shown in Figure 2.3.

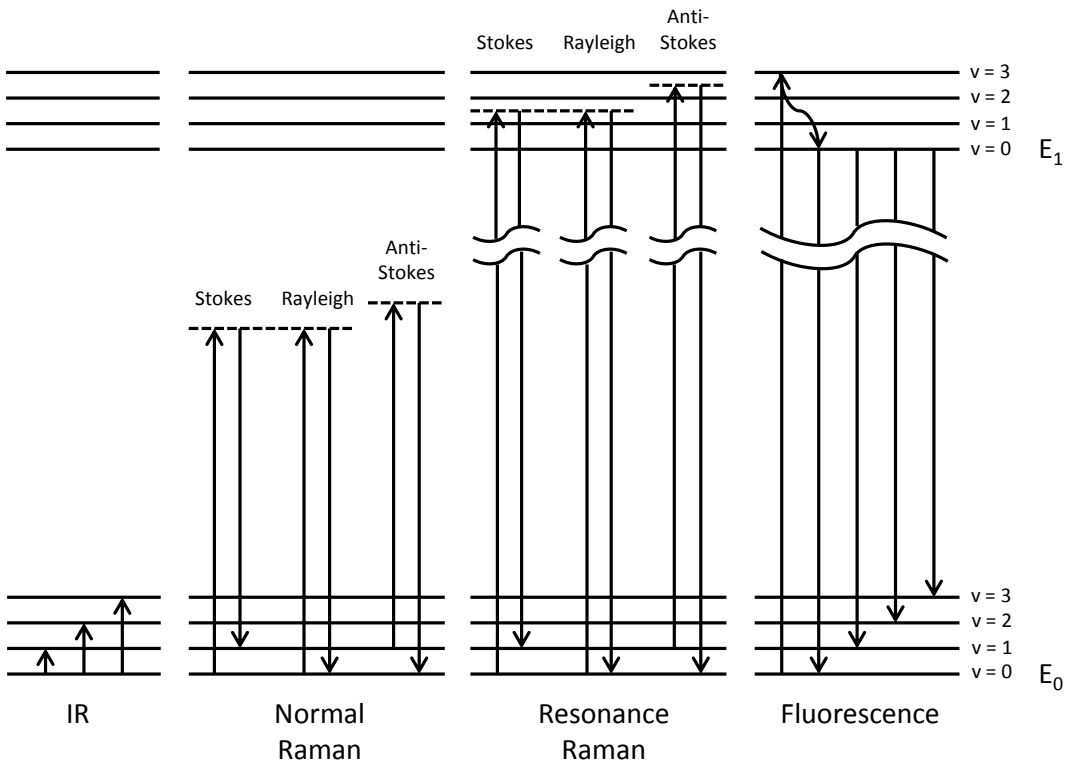

Figure 2.3: Energy level diagrams for infrared (IR), Raman, resonance Raman, and Fluorescence induced transitions. The upward oriented arrows illustrate the effect of the incident photons while the downward oriented arrows illustrate immediate relaxation and scattered photons.

2.3.1 Classical treatment of Raman scattering

The origins and mechanisms for normal Rayleigh (elastic) and Raman scattering can be understood through the classical treatment of both the electromagnetic field (photons) and lattice (material) vibrations. The classical theory begins by considering the first-order electric polarization. The electric dipole moment due to an external electric field is

$$\vec{p} = \vec{\vec{\alpha}} \cdot \vec{E}, \tag{2.1}$$

where $\vec{\vec{\alpha}}$ is the polarizability tensor, which depends on the nuclear coordinates and is therefore frequency dependent, and $\vec{E}$ is the electric field of the incident radiation. For constant α, the frequency at which the polarization oscillates will only depend on the incident radiation, yielding only Rayleigh scattering. However, the polarizability may change with vibrations of the material, and should therefore be expanded in a Taylor series with respect to the normal modes of nuclear displacement, q_k:

$$\alpha_{\rho\sigma} = (\alpha_{\rho\sigma})_0 + \sum_k \left(\frac{\partial \alpha_{\rho\sigma}}{\partial q_k}\right)_0 q_k + \frac{1}{2}\sum_{k,l}\left(\frac{\partial^2 \alpha_{\rho\sigma}}{\partial q_k \partial q_l}\right)_0 q_k q_l + \ldots. \tag{2.2}$$

The displacement of the atom in a particular direction is expressed by

$$q_k = q_{k_0}\cos(\omega_k t). \tag{2.3}$$

Because it was assumed that the lattice vibrations are approximately harmonic, meaning that the restoring force is proportional to the first power of q, the higher order terms in the Taylor series are disregarded. Under illumination by a laser, the electric field felt by the atoms can be expressed as

$$\vec{E} = \vec{E_0}\cos\omega_0 t, \tag{2.4}$$

where ω_0 is the frequency of the laser light and $\vec{E_0}$ gives the amplitude and polarization of the field. By substituting Equation 2.4, and the result of substituting Equation 2.3 into

Equation 2.2, into Equation 2.1, the polarization can be rewritten as

$$\vec{p} = \vec{\vec{\alpha}}_0 \cdot \vec{E}_0 \cos(\omega_0 t) + \left(\frac{\partial \vec{\vec{\alpha}}}{\partial q_k}\right)_0 \cdot \vec{E}_0 q_{k_0} \cos(\omega_0 t) \cos(\omega_k t). \tag{2.5}$$

By applying the trigonometric identity,

$$\cos A \cos B = \frac{1}{2}[\cos(A+B) + \cos(A-B)], \tag{2.6}$$

to the right-most term in Equation 2.5, we arrive at the following expression for the electric polarization:

$$\vec{p} = \vec{\vec{\alpha}}_0 \cdot \vec{E}_0 \cos(\omega_0 t) + \left(\frac{\partial \vec{\vec{\alpha}}}{\partial q_k}\right)_0 \cdot \vec{E}_0 q_{k_0} \cos[(\omega_0 + \omega_m)t] + \left(\frac{\partial \vec{\vec{\alpha}}}{\partial q_k}\right)_0 \cdot \vec{E}_0 q_{k_0} \cos[(\omega_0 - \omega_m)t]. \tag{2.7}$$

This expression for the polarization contains terms for Rayleigh, anti-Stokes Raman, and Stokes Raman scattering respectively. As can be seen from Equation 2.7, when $\left(\frac{\partial \vec{\vec{\alpha}}}{\partial q_k}\right)_0 = 0$, the material is not Raman-active and only Rayleigh scattering will be observed. In general, molecules or systems which have a center of symmetry may exhibit only a few Raman-active optical vibrational modes, if any. For example, diamond has only three triply degenerate vibrational modes, and NaCl has no first-order modes [36]. For materials with low symmetry, most, if not all of the optical vibrational modes are typically Raman-active.

While the vibrational frequency of a diatomic molecule may be easily calculated via Equation 2.8, where k is the force constant and μ is the reduced mass, determining the vibrational frequencies becomes increasingly complicated for complex materials with many atoms.

$$\omega = \frac{1}{2\pi}\sqrt{\frac{k}{\mu}} \tag{2.8}$$

Finally, because the temperature of a sample determines the population of the different vibrational levels, comparison of the Stokes and Anti-Stokes Raman intensities allows the

temperature of the material to be determined according to Equation 2.9.

$$\frac{I_{anti-Stokes}}{I_{Stokes}} = \left(\frac{\omega_0 + \omega_m}{\omega_0 - \omega_m}\right)^4 exp\left(-\frac{\hbar\omega_m}{k_B T}\right) \tag{2.9}$$

At this point, the classical theory becomes insufficient and quantum mechanics must be invoked in order to provide further information concerning the Raman scattering selection rules and the expected intensities of each vibrational mode.

2.3.2 Semiclassical treatment of Raman scattering

A full quantum mechanical treatment is not necessary in order to accurately calculate the intensities and behavior of the Raman modes of a material. In fact, the treatment of the electric field of the incident photons typically remains classical while the vibrational energies of the material system are quantized. This is, in general, a fairly difficult and involved procedure, of which a thorough description may be found in the existing, focused literature, such as "The Raman Effect" by Derek Long [37]. Nevertheless, the main points are summarized here to provide a comparison with the classical treatment.

To begin, time dependent perturbation theory is applied to treat the incident electromagnetic radiation as a perturbation of the states of the material. The transition electric dipole moment may then be represented as

$$\mathbf{p}_{fi} = \langle \Psi_f^{'} | \hat{\mathbf{p}} | \Psi_i^{'} \rangle, \tag{2.10}$$

where $\Psi_f^{'}$ and $\Psi_i^{'}$ are the time-dependent perturbed wavefunctions of the final and initial states of the material, respectively. These perturbed wavefunctions can be represented as series expansions containing the sum of the unperturbed state, $\Psi_i^{(0)}$, and every higher order modification, $\Psi_i^{(n)}$, to the unperturbed state.

To simplify the derivation, a few assumptions are generally made: (1) the perturbation

is first order only, (2) the perturbation, and therefore the interaction Hamiltonian, is solely electric dipole in nature, and (3) the perturbation is produced by the time-dependent electric field associated with a plane monochromatic electromagnetic field of frequency ω_0. The first assumption eliminates all $\Psi_i^{(n)}$ with $n \geq 2$ from the wavefunctions representing the perturbed states. Equation 2.10 then becomes

$$\begin{aligned} \mathbf{p}_{fi}^{(1)} &= \langle (\Psi_f^{(0)} + \Psi_f^{(1)}) | \hat{\mathbf{p}} | (\Psi_i^{(0)} + \Psi_i^{(1)}) \rangle \\ &= \langle \Psi_f^{(1)} | \hat{\mathbf{p}} | \Psi_i^{(0)} \rangle + \langle \Psi_f^{(0)} | \hat{\mathbf{p}} | \Psi_i^{(1)} \rangle + \langle \Psi_f^{(0)} | \hat{\mathbf{p}} | \Psi_i^{(0)} \rangle + \langle \Psi_f^{(1)} | \hat{\mathbf{p}} | \Psi_i^{(1)} \rangle. \end{aligned} \tag{2.11}$$

The third term represents a direct transition between unperturbed states which does not depend on the electric field and is not a scattering process, and is therefore dropped. Similarly, the fourth term is also dropped because it is a second order transition between two perturbed states which depends on the square of the electric field.

For normal Raman scattering, which involves a transition from state ψ_i to state ψ_f through some intermediate state ψ_r, the transition electric dipole moment can be expanded into a weighted sum of transition pairs involving all possible intermediate states, ψ_r. Each term is weighted by either the sum or difference of the respective frequencies involved as appropriate. This information, along with the assumptions stated earlier, allows the time dependent perturbed wavefunctions to be expressed in terms of time independent unperturbed wavefunctions. Then, if only the terms corresponding to Stokes and anti-Stokes Raman scattering are considered, the ρ component (for simplicity) of Equation 2.11 can be expanded as

$$(p_\rho^{(1)})_{fi} = \frac{1}{2\hbar} \sum_{r \neq i,f} \left\{ \frac{\langle \psi_f | \hat{p_\rho} | \psi_r \rangle \langle \psi_r | \hat{p_\sigma} | \psi_i \rangle}{\omega_{ri} - \omega_0 - i\Gamma_r} + \frac{\langle \psi_f | \hat{p_\sigma} | \psi_r \rangle \langle \psi_r | \hat{p_\rho} | \psi_i \rangle}{\omega_{rf} + \omega_0 + i\Gamma_r} \right\} \tilde{E}_{\sigma_0} exp(-i\omega_s t) + complex\ conjugate. \tag{2.12}$$

In Equation 2.12 the wavefunctions $\psi_{i,f,r}$ are time independent and are related to their

respective time dependent wavefunctions according to

$$\Psi_{i,f,r} = \psi_{i,f,r} e^{-i(\omega_{i,f,r} - i\Gamma_{i,f,r})t}, \tag{2.13}$$

where Γ is related to the lifetime, τ, of the state via $\tau_{i,f,r} = 1/(2\Gamma_{i,f,r}(\omega))$. The lifetimes of the initial and final states ψ_i and ψ_f are assumed to be infinite, making $\Gamma_i = \Gamma_f = 0$. Additionally, the double subscript on ω_{ri} and ω_{rf} indicates a frequency difference such that $\omega_{ri} = \omega_r - \omega_i$ and $\omega_{rf} = \omega_r - \omega_f$, respectively. $\tilde{E}_{\sigma_0}$ is the σ component of the complex amplitude of the incident electromagnetic wave. Finally, $\omega_s = \omega_0 - \omega_{fi}$.

It is important to note that for normal Raman scattering, $\hbar\omega_0$ is significantly less than the energy required to excite a transition between electronic levels. Thus, ψ_r is a virtual state and is not a solution of the time-independent Schrödinger equation. As such, the energy is ill-defined and therefore, via the uncertainty principle, the lifetime must be extremely short. Since $\omega_0 << \omega_{ri}, \omega_{rf}$, Γ_r may be safely ignored even in the first term of Equation 2.12. From Equation 2.12, the transition polarizability can be defined as

$$(\alpha_{\rho\sigma})_{fi} = \frac{1}{\hbar} \sum_{r \neq i,f} \left\{ \frac{\langle \psi_f | \hat{p}_\rho | \psi_r \rangle \langle \psi_r | \hat{p}_\sigma | \psi_i \rangle}{\omega_{ri} - \omega_0} + \frac{\langle \psi_f | \hat{p}_\sigma | \psi_r \rangle \langle \psi_r | \hat{p}_\rho | \psi_i \rangle}{\omega_{rf} + \omega_0} \right\}. \tag{2.14}$$

Using this definition, including the complex conjugate, and applying trigonometric identities, a form for $(p_\rho^{(1)})_{fi}$ similar to scattering portion of Equation 2.7 is achieved,

$$(p_\rho^{(1)})_{fi} = (\alpha_{\rho\sigma})_{fi} E_{\sigma_0}(\omega_0) cos\omega_s t, \tag{2.15}$$

which shows that the classical and quantum mechanical treatments are consistent with each other. However, because the quantum mechanical definition of the transition polarizability includes the actual wavefunctions and energy levels of the material system, the relationship governing how the characteristics of the scattered radiation arise from the properties of the scattering material may be established.

2.3.3 Raman scattering in single crystals

Raman scattering in single crystals poses a special, slightly more complicated case of the previous derivations, which assume the material system is a freely rotating, isolated molecule. Indeed, in a single crystal, Raman scattering gives rise to, and interacts with, vibrations which affect the entire lattice. These vibrations are called phonons and have their own polarization, wavevector, and momentum. Complicating the issue even further is the fact that in uniaxial, piezoelectric crystals such as $LiNbO_3$ and $LaBGeO_5$, the long-range electric fields associated with polar vibrations shift the frequencies of some Raman modes away from their $\mathbf{k} = 0$ values, remove the degeneracy of certain lattice vibrations, and result in additional electron-lattice interactions beyond those of simple deformations [38].

The standard nomenclature when discussing polar phonons stipulates that the related Raman mode is transverse when the wavevector of the phonon is orthogonal to its polarization ($\mathbf{k} \cdot \mathbf{P} = 0$) and is longitudinal when the wavevector of the phonon is parallel to its polarization ($\mathbf{k} \cdot \mathbf{P} = kP$) [3, 38]. The abbreviations (TO) and (LO) are used for labeling transverse and longitudinally polarized Raman modes as appropriate. In general, according to Loudon [38], the Raman scattering efficiency can be calculated according to

$$S = A \sum_j |\hat{e_i} \cdot \vec{\vec{\mathbf{R}}}_j \cdot \hat{e_s}|^2, \tag{2.16}$$

where A is a constant, and $\hat{e}_i$ and $\hat{e}_s$ are unit vectors in the directions of the polarizations of the incident and scattered photons, respectively. $\vec{\vec{\mathbf{R}}}_j$ is the Raman tensor of phonon j. The Raman tensors for all of the crystal symmetry classes have been determined by Group Theory and represent the non-vanishing components of the polarizability tensor $\alpha_{\rho\sigma}$. They are tabulated in Loudon [38] or Gardiner [39]. As mentioned previously, uniaxial, piezoelectric crystals possess long-range electric fields due to polar phonons. As a result, corrections to the scattering efficiency must be made. This is best approached component-

wise:

$$S = \left\{ \sum_{\sigma,\rho,\tau=x,y,z} e_i^\sigma R_{\sigma\rho}^\tau (\alpha \xi^\tau + \beta k^\tau) e_s^\rho \right\}^2 , \tag{2.17}$$

where σ, ρ, and τ are the principle axes of the crystal. The correction term includes ξ^τ and k^τ, which are components of the unit vectors along the polarization and propagation directions of the phonon, respectively, relative to the τ axis. α and β are constants.

Equation 2.17, while difficult to compute, can be used to determine which types of Raman modes should be observable for a particular experimental geometry. The experimental geometry is typically noted according to the Porto notation, $a(bc)d$, with respect to the crystal axes. In this notation a and d indicate the orientation of the wavevectors of the incident and scattered electromagnetic waves, respectively, and b and c give the polarizations thereof. In some cases, a bar over either the a or d is used to denote that it is negative.

2.3.4 Raman scattering in $LiNbO_3$

$LiNbO_3$ belongs to the C_{3v} symmetry group and has two formula units per unit cell. This results in three acoustic and 27 optical vibrational modes: four A_1, five A_2 and nine doubly-degenerate E modes. The A_2 modes are Raman inactive. Meanwhile, the A_1 and E modes are polar, with their polarizations being parallel and orthogonal to the c-axis of the crystal, respectively. Additionally, because they are polar, both types are infrared and Raman active. The Raman tensors according to Loudon [38] are

$$A_1(z) = \begin{pmatrix} a & 0 & 0 \\ 0 & a & 0 \\ 0 & 0 & b \end{pmatrix}, \; E(x) = \begin{pmatrix} 0 & c & d \\ c & 0 & 0 \\ d & 0 & 0 \end{pmatrix}, \; E(y) = \begin{pmatrix} c & 0 & 0 \\ 0 & -c & d \\ 0 & d & 0 \end{pmatrix}, \tag{2.18}$$

where a, b, c, and d are constants. Using these tensors and the Raman selection rules, in combination with controlled experimental geometries, the Raman modes observed in $LiNbO_3$ have been identified (refs 25-38 in G. Stone [3]). They are typically labeled as

$\gamma(\mathrm{XO})_n$, with gamma indicating either A or E modes, X indicating either transverse or longitudinal, and n denoting that it is the n^{th} mode of that type as counted from the Rayleigh line. Figure 2.4 displays a typical Raman spectrum for stoichiometric $LiNbO_3$ in which the modes relevant to Chapter 4 are labeled according to this scheme. It should be noted that both A and E modes are present in the spectrum due to both the depolarization of the excitation beam at the focus of the high numerical aperture (NA) microscope objective and the fact that no analyzer was used in the collection beampath.

2.3.5 Raman scattering in $LaBGeO_5$

$LaBGeO_5$ belongs to the trigonal polar space group $P3_1$ (C_3^2) and has three formula units per unit cell. This results in three acoustic and 69 optical vibrational modes. In the low temperature phase there are 23 non-degenerate Raman and IR-active A(z) modes and 23 doubly-degenerate Raman and IR-active E(x,y) modes. The Raman tensors according to Loudon [38] are

$$A_1(z) = \begin{pmatrix} a & 0 & 0 \\ 0 & a & 0 \\ 0 & 0 & b \end{pmatrix}, \; E(x) = \begin{pmatrix} c & d & e \\ d & -c & f \\ e & f & 0 \end{pmatrix}, \; E(y) = \begin{pmatrix} d & -c & -f \\ -c & -d & e \\ -f & e & 0 \end{pmatrix}, \tag{2.19}$$

where a, b, c, d, e, and f are constants. A number of studies have investigated the Raman spectra of $LaBGeO_5$, and by using the tensors of Equation 2.19 in combination with the Raman selection rules and controlled experimental geometries, have determined the frequencies of the A and E modes [24, 40]. However, the $\gamma(\mathrm{XO})_n$ notation used for $LiNbO_3$ has generally not been utilized for $LaBGeO_5$ until very recently [4].

Though earlier works [24, 33] have made reasonably accurate assignments of broad ranges of the Raman spectra in $LaBGeO_5$, Smirnov *et al.* were able to assign individual Raman modes to their respective origins via a valence force field (VFF) model using parameters derived from *ab initio* normal mode calculations [25]. Unfortunately, the exact

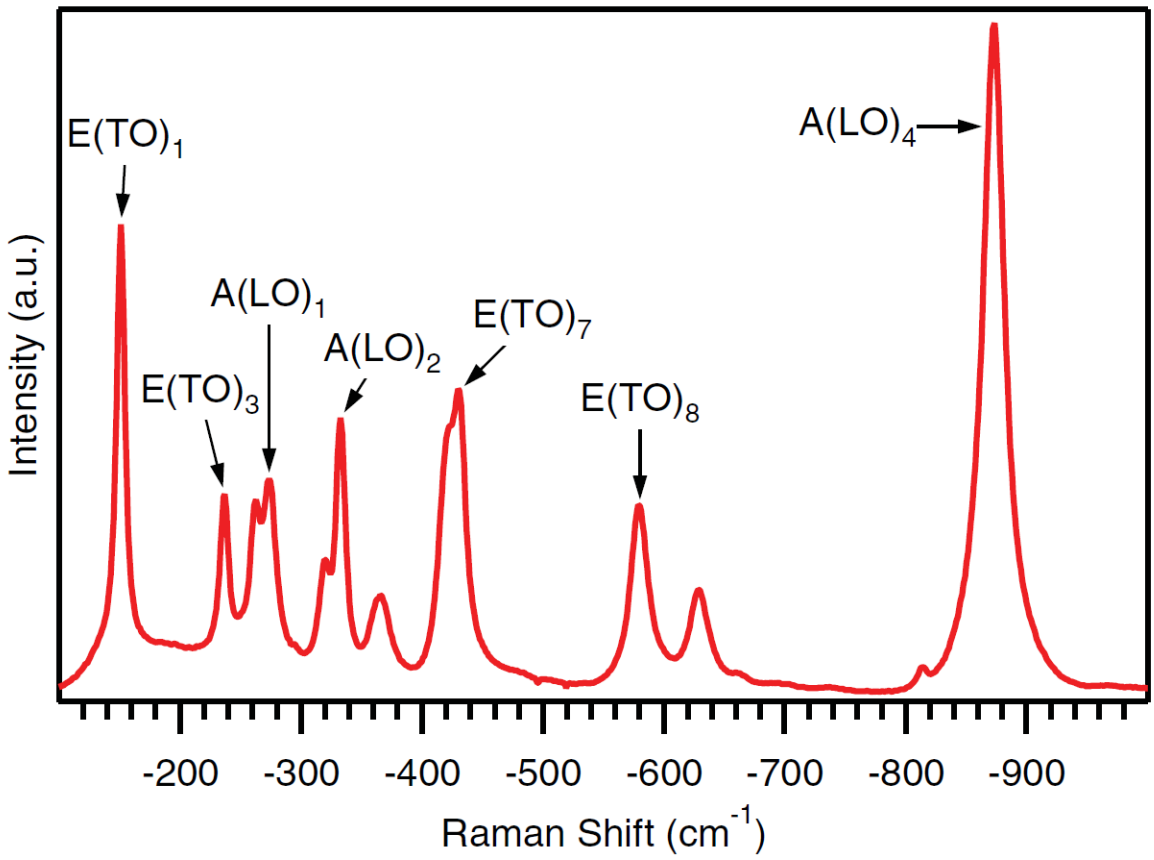

Figure 2.4: Raman spectrum of stoichiometric $LiNbO_3$ with the Raman modes studied in Chapter 4 labeled.

frequencies determined by Smirnov did not perfectly match those experimentally observed. Closer agreement between theoretically predicted and experimentally observed frequencies of the Raman modes in $LaBGeO_5$ was achieved by Shaltaf *et al.* using density functional perturbation theory calculations in which the lattice parameters were fixed at experimentally determined values [4].

Table 2.1 summarizes the findings of the aforementioned theoretical works, as well as the experimental work by Hrubá *et al.* [40]. The notation of the mode assignments is as follows. RUM1 and RUM2 (rigid unit modes) represent intra-chain motions of entire (rigid) tetrehedra. Modes labeled as ν or δ represent stretching or bending vibrations, respectively, and can be either symmetric (s) or anti-symmetric (as). Finally, O2 and O3 represent different oxygen sites within the unit cell, as noted in the source literature [25].

Figure 2.5 displays typical Raman spectra for undoped $LaBGeO_5$ using different scattering geometries, and indicates the specific modes which are discussed in Chapter 6. The frequencies of the observed modes are listed in Table 2.2 and compared to the values reported by Pisarev *et al.* [24].

2.4 Laser-induced crystallization

In this section a brief summary of the fundamental science of laser-induced crystallization is given. Additionally, an overview of the work done by others and the phenomena they observed, is presented. This section is not intended to be comprehensive, and for further information the reader is referred to the dissertation of A. Stone [5].

Photoinduced changes of both the structure and properties of amorphous materials manifest in a variety of ways depending on the composition of the glass and the wavelength, intensity, and duration of exposure to the light source. These phenomena have long been of interest and include refractive index changes, photo-expansion/contraction, and photo-

Table 2.1: List of calculated and observed vibrational mode frequences (in cm^{-1}) in $LaBGeO_5$. See text for definitions of assignment notations.

Ref.	VFF model [25]			Experiment [40]				DFPT [4]			
Mode	**Assignment**	**A(TO)**	**E(TO)**	**A(TO)**	**A(LO)**	**E(TO)**	**E(LO)**	**A(TO)**	**A(LO)**	**E(TO)**	**E(LO)**
1	La x-displacements	105	101	87	89	92	93	91	93	90	90
2	$BGeO_5$ chain rotation	110	119	95	96	109	110	97	97	110	111
3	GeO_4 wagging	122	125	117	119	124	125	118	122	128	128
4	RUM2	142	141	144	145	162	179	148	149	163	176
5	La z-displacements	163	187	173	213	187	200	166	184	183	197
6	La y-displacements	198	214			207	208	184	210	207	211
7	$\delta(GeO_4)$ and $\delta(BO_4)$	221	245	215	222	233	234	210	217	221	222
8		284	289		273	258	262	280	280	259	261
9		304	319		301	301	320	301	302	307	321
10		340	370	306	307	336	352	303	304	333	347
11		375	382	324	329	384	396	322	327	377	391
12		401	456	368	380	423	439	372	381	418	431
13	RUM1	485	518	389	422	454		388	419	446	446
14	$\delta_F(BO_4)$	555	557	503	510	496	502	492	501	485	489
15		599	653	546	552	616	621	539	544	609	611
16	$\nu_{A1}(GeO_4)$+$\nu_{A1}(BO_4)$	697	719	631	633	695	701	624	626	690	690
17	ν_{as}(Ge-O2)	752	717	733	745	722	753	732	744	723	743
18	ν_s(Ge-O3)	792	785	799	803	784	811	810	817	790	824
19	ν_{as}(Ge-O3)	800	809	806	813	826	834	818	819	835	843
20	ν_s(Ge-O2)	848	861	847	852	859	863	850	854	869	872
21	$\nu_F(BO_4)$	930	936	864	866	918	928	860	873	912	923
22		1006	968	941	980	975	1042	948	981	971	1031
23		1034	1043	992	1050	1088	1098	990	1043	1092	1095

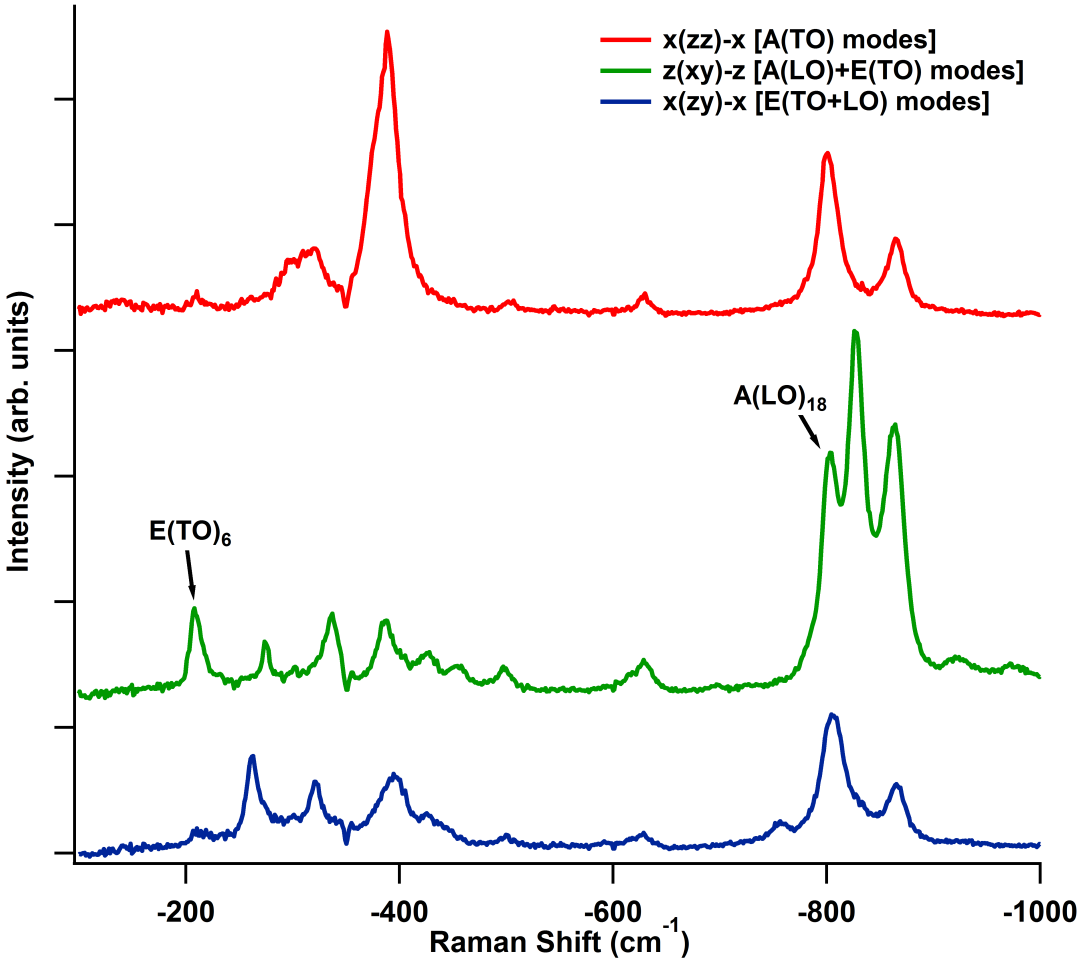

Figure 2.5: Raman spectra of undoped $LaBGeO_5$ in the x(zz)-x, z(xy)-z, and x(zy)-x orientations. The observed Raman mode frequencies for each geometry are listed in Table 2.2

.

Table 2.2: List of observed Raman mode frequencies (in cm^{-1}) in $LaBGeO_5$ for various geometries. The geometries in bold indicate the respective spectrum shown in Figure 2.5 from which the frequencies were determined.

A(TO)		**A(LO)+E(TO)**		**E(TO+LO)**	
x(zz)x y(zz)y x(zz)y		z(xx)z **z(xy)z**		**x(zy)x** y(xz)y x(yz)y x(zx)y	
Ref. [24]	Fig. 2.5	Ref. [24]	Fig. 2.5	Ref. [24]	Fig. 2.5
6		94.5		94.1	
111.3		111.2		111.3	
		121.6			
126.8		126.4		126.8	
146.3		146.2			
		165		164.4	
175					
				180	
		187.7		187.8	
				204.6	
		208.5	207.34	209.1	212.95
217	210.08			216.2	
		224			
		234.5		236	
		260.1	266.05	261.2	261.74
263.9				265.3	
275.1		275.2	274.96	275.6	271.91
303.2	297.36	302.5	304.85	302.3	
310.5	309.33	310.7		311	
326.7	320.3			322.2	321.51
		339.5	336.16	338.5	
				355.5	

Continued on Next Page...

Table 2.2 – Continued

A(TO)		**E(TO)**		**E(TO+LO)**	
x(zz)x y(zz)y x(zz)y		z(xx)z **z(xy)z**		**x(zy)x** y(xz)y x(yz)y x(zx)y	
Ref. [24]	Fig. 2.5	Ref. [24]	Fig. 2.5	Ref. [24]	Fig. 2.5
371	374.38			371.2	
		383			
391.8	389.43	387.7	387.42	389	
				398	394.22
				414	
		425.9	425.1	426.1	426.48
				441.6	440.09
		455.8	455.45		
505.9	503.25	499.3	497.27	502.2	498.48
551.2		555			
		618.4	616.32	621.6	616.16
632.4	628.84	634	630.15	632	628.37
		700	697.04	701	
		726	731.26		
734					
		750		753	
				756	755.65
		785.7		784.8	
801.4	798.01			800	799.15
805.2	802.58	805.9	802.67		
				812	807.16
		826.8	827.71	826.6	
				836	833.62
850.2	854.97				

Continued on Next Page...

Table 2.2 – Continued

A(TO)		**E(TO)**		**E(TO+LO)**	
x(zz)x y(zz)y x(zz)y		z(xx)z **z(xy)z**		**x(zy)x** y(xz)y x(yz)y x(zx)y	
Ref. [24]	Fig. 2.5	Ref. [24]	Fig. 2.5	Ref. [24]	Fig. 2.5
866.1	865.75	860.9	860.72	864.8	865.68
		868	867.44		
		920.4	920.15	925	
				930	
936					
		976.2	977.3	979	
997.2					
				1020	
				1045	
		1090	1087.1	1095	1087.6
				1113	

darkening/bleaching [2]. Since the 1970s, the utilization of focused laser light to create functional microstructures as components of integrated optics and data storage has been studied [5]. Recently (within the last two decades), spatially-selective crystallization of nonlinear optical crystals in glass via laser irradiation was achieved. Because of the fantastic properties of crystals, including ferroelectricity, ferromagnetism, thermoelectricity, and other nonlinear optical effects, the ability to create micro-scale architectures affords the possibility of 3D optical integrated circuits and memory, among other exciting applications. Therefore, significant effort has been expended by a number of groups using a variety of types of both continuous wave (CW) and ultrafast pulsed lasers to crystallize a great number of crystalline phases on the surface of, and within, an even greater number of precursor glasses.

In order to understand how laser-irradiation functions as the phase transformation-inducing mechanism between the glassy and crystalline states, it is helpful to discuss and understand the differences between the two phases and the factors affecting the transformation. In glasses the constituent atomic and molecular structures are disordered and randomly oriented with respect to each other, similar to the situation in a liquid. For this reason, glass, while solid to the touch, is considered to be a liquid which is in a supercooled state. As might be expected, below the melting point this situation is typically less energetically favorable than that where the constituents are organized in a regular and periodic fashion as in a crystalline structure. Nevertheless, materials in a glassy phase are frequently possible due to the fact that arranging all of the atomic and molecular structures takes time, of which there may not be enough as a melt cools, depending on its viscosity and the cooling rate. Therefore, a melt with low viscosity requires a very fast cooling rate in order to avoid devitrification, and vice versa. On the other hand, when crystallization is desired, the quality of the resulting crystal will depend on how well the approach caters to the ability of the constituents to organize themselves. Specifically, the temperature of

easiest crystal nucleation is typically lower than the temperature at which the crystal grows fastest. This means that when heating a glass, as in a conventional furnace, two temperature steps are typically required, with enough time given at each to achieve the desired result. Conversely, when cooling from a melt, as in techniques such as the Czochralski method, a pre-existing seed crystal must be provided since the temperature will reach that of the maximum growth-rate without ever passing through the temperature range where nucleation is possible. In the case of laser-induced crystallization, the situation becomes somewhat more complicated, especially when the laser focus is translated through the bulk of the glass resulting in regions of both heating and cooling.

As mentioned earlier, both CW and pulsed laser irradiation can be used to achieve crystallization. This occurs via localized heating following absorption of the incident photons. Photons in the infrared range have energies comparable to phonon energies in the lattice. In this case the absorbed energy directly excites vibrations and results in heating. For photon energies corresponding to the visible and near-UV range, most insulating and semiconducting materials are transparent due to their larger bandgaps. Thus, for absorption to occur, the energy, $E = \frac{hc}{\lambda}$, of the incident photons must exceed that of the bandgap. If this condition is met, an electron will be promoted from the valence band to the conduction band. Shortly thereafter, if the bandgap is indirect, the electron will non-radiatively decay to the valence band and energy will be transferred to the lattice via electron-phonon coupling. As in the direct excitation of phonons, this results in localized heating of the material.

The general equation describing absorption is

$$\frac{dI}{dl} = -\alpha^{(1)}I - \alpha^{(2)}I^2 - \alpha^{(3)}I^3 - ... = -\sum_{n}^{\infty} \alpha^{(n)}I^n, \tag{2.20}$$

where I is the intensity, l is the length of material traversed, and n is the order of the effect. $\alpha = \sigma N$ is the material- and wavelength-dependent absorption coefficient where σ is the

absorption cross-section and N is the density of absorbers. By truncating Equation 2.20 to include only the first order term, one receives a differential equation which, when solved, produces the well-known Beer-Lambert Law for linear absorption:

$$I = I_0 exp(-\alpha l) = I_0 exp(-\sigma N l). \tag{2.21}$$

Because the bandgap in insulators is large, α for wavelengths in the visible to near-UV region is small. Therefore, it is convenient to dope the glass with rare earth or transition metal ions which have lower-energy electronic transitions in order to effectively lower the bandgap and increase α at longer wavelengths in order to achieve linear absorption of the incident laser light. This process is utilized during CW laser induced crystallization. Conversely, as seen in Equation 2.20, even a small α may be overcome with enough intensity, due to the fact that in higher-order processes the intensity is multiplied in increasing powers. In order for this to happen, n photons must excite the electron at the same time. Normally this is improbable, except when the intensity is very large to begin with, as with the pulses of an ultrafast pulsed laser.

The process of heating as a result of multiphoton absorption is somewhat more complicated than that of simple non-radiative decay as discussed earlier. Once in the conduction band due to multiphoton absorption, electrons can indiscriminantly absorb energy from photons of any wavelength, regardless of whether they exceed the bandgap energy. This allows subsequent linear absorption to take place. If an electron in the conduction band linearly absorbs additional energy in excess of the bandgap, and then collides with, and imparts this excess energy to, an electron still in the valence band, a runaway avalanche ionization cascade can occur. This establishes an electron plasma within the material. As electrons within this plasma shed their energy, they can do so in the form of photons, which produce a white light continuum, and phonons, which result in the desired localized heating.

2.4.1 CW laser induced crystallization

Because the absorption of CW laser radiation is a linear process and therefore a single photon event, the wavelength of the laser radiation is very important as it must be tuned to the appropriate transition energy of the dopant ions. However, once the laser intensity and absorption thereof are sufficient, and other conditions such as glass composition, ambient temperature, and exposure time are favorable, a crystal may be nucleated. It should be noted that because the absorption process is linear in nature, the CW laser-induced crystallization process is inherently limited to the surface of a homogeneously doped sample, as the beam intensity is quickly depleted when focusing below the surface is attempted.

CW laser irradiation was first utilized to achieve crystallization of glass by the group of Takayuki Komatsu in the early 2000s [41]. In this case the authors produced crystals of $Sm_2Te_6O_{15}$ on precursor glasses with compositions of 10RO-10Sm_2O_3-80TeO_2 (R=Mg, Ba) using a Nd:YAG laser with a wavelength of $1064nm$ to excite the f-f transition ($^6H_{5/2} \rightarrow {}^6F_{9/2}$) of the Sm^{3+} ions. Since then, significant progress has been made and an extensive list of crystals have been grown. Table 2.3 provides a summary of glass/crystal/laser combinations which have been successful.

As seen in Table 2.3, many glass systems contain no samarium, as it was found that other rare earths work just as well while providing different functionality. Hence, the approach of using rare earths as absorbers, originally called "selective (samarium) atom heat processing" [42], is now known more generally as "rare earth atom heat (REAH) processing" [43]. Similarly, glass compositions containing a small amount of transition metals were also found to crystallize under CW laser irradiation. This technique was termed "transition metal atom heat (TMAH) processing" and utilizes d-d transitions of the transition metal ions [43]. Compared to rare-earth doped glasses for CW laser-induced crystallization which contain greater than 8 mol%, a relatively small amount (0.3-1 mol%) of transition metal dopants are needed to achieve sufficient absorption [43].

Table 2.3: List of glass compositions successfully crystallized by CW laser irradiation, and references therefor. An even more extensive list may be found in a review paper by Honma [1], and the references therein.

Glass Composition	**Crystal**	**Laser**	**Reference**
21.5Sm_2O_3-63.75MoO_3-15B_2O_3	β'-$Sm_2(MoO_4)_3$	Nd:YAG	[44]
lead and barium vanadate	PbV_2O_5	diode	[45]
50GeO_2-25B_2O_3-17.5La_2O_3-7.5Yb_2O_3	$LaBGeO_5$	Ar^+	[46]
xPbO-(100-x)V_2O_5	PbO-V_2O_5	diode	[47]
$Nd_{0.2}La_{0.8}BGeO_5$	$LaBGeO_5$	Ti:Sapphire	[48]
$Sm_{0.5}La_{0.5}BGeO_5$	$LaBGeO_5$	Nd:YAG	[49]
xGeS_2-(100-x)$SbSI$ (x=0,10,20}	$SbSI$	Ar^+	[50]
10Sm_2O_3-35Bi_2O_3-55B_2O_3	$BiSmBO_3$	Nd:YAG	[42]
10Sm_2O_3-40BaO-50B_2O_3	β'-BaB_2O_4	Nd:YAG	[51]
10Dy_2O_3-45BaO-45B_2O_3	β'-BaB_2O_4	Nd:YAG	[51]
1M-33.3BaO-16.7TiO_2-50XO_2 (M=Fe_2O_3,NiO,V_2O_5) (X=Ge,Si)	$Ba_2TiX_2O_8$	Nd:YAG	[43]
0.5CuO-35Li_2O-30Nb_2O_5-35SiO_2 (and others)	$LiNbO_3$	Yb:YVO_4 fiber	[52, 53]
xCuO-33.3Li_2O-66.7SiO_2 (x=0,1,2)	$Li_2Si_2O_5$	Yb:YVO_4 fiber	[54]
1Cuo-33.3BaO-16.7TiO_2-50GeO_2	Ba_2TiGeO_8	Nd:YAG	[55]
0.5CuO-Li_2O-32Nb_2O_5-10B_2O_3-20SiO_2	$LiNbO_3$	Yb:YVO_4 fiber	[56]
8Sm_2O_3-37Bi_2O_3-55B_2O_3	$Sm_xBi_{1-x}BO_3$	Nd:YAG	[57]
10BaO-xLn_2O_3-(10-x)Sm_2O_3-80TeO_2 (Ln=La,Er)	$Ln_2Te6_6O_{15}$	Nd:/YAG	[58, 59]
10Sm_2O_3-40BaO-50B_2O_3	β'-BaB_2O_4	Nd:YAG	[59]
1CuO-40Li_2O-32Nb_2O_5-28SiO_2	$LiNbO_3$	Nd:YAG	[60]
0.5CuO-4Gd_2O_3-46Bi_2O_3-50B_2O_3	$Gd_xBi_{1-x}BO_3$	Nd:YAG	[61]
10RO-10Sm_2O_3-80TeO_2 (R=Mg,Ba)	$Sm_2Te6_6O_{15}$	Nd:YAG	[41]
$SbSI$	$SbSI$	diode	[62]
1CuO-25Li_2O-25Nb_2O_5-50TeO_2	$LiNbO_3$	Nd:YAG	[63]
32Sm_2O_3-18.25Gd_2O_3-63.75MoO_3-15B_2O_3	β'-$(Sm,Gd)_2(MoO_4)_3$	Yb:YVO_4 fiber	[64]

2.4.2 Femtosecond laser induced crystallization

Compared to CW laser-induced crystallization, pulsed laser crystallization is a nonlinear, multiphoton process. This means that the intensity (power per unit area), pulse duration, and repetition rate are the most important parameters. If the first two are not sufficient, nonlinear absorption cannot occur. If the repetition rate is too low, the heat provided from each pulse will dissipate before the next pulse arrives such that the minimum temperature for crystallization may never be reached. On the other hand, if the repetition rate is too high, too much heat may be accumulated too quickly, leading to cracking or ablation.

Because the absorption process in pulsed laser crystallization is nonlinear, the focal point can theoretically be placed at any point within the volume of the sample due to the fact that absorption will only occur where the intensity is great enough. This ability presents both tremendous benefits and additional complications. In terms of benefits, the first is that normally transparent materials can be affected despite their transparency. The second is the capability to create 3D architectures within the bulk of the material, as first proposed by Glezer [65], Davis [66], and Hirao [67]. Conversely, irradiating within the bulk of the sample poses the complication of focal profile distortion due to spherical aberration caused by the material above the focus [68]. Additionally, the lack of a surface interface or impurity dopants means that there are far fewer crystal nucleation sites than in materials used for CW laser-induced crystallization.

Nevertheless, pulsed laser-induced crystallization inside of glass was achieved by Miura *et al.* [69], who realized the formation of β-BaB_2O_4 crystals in 47.5BaO-5Al_2O_3-47.5B_2O_3 glass. As with CW laser-induced crystallization, pulsed laser-induced crystallization has also been the subject of significant study since its inception. A summary list of successful glass/crystal/laser combinations is presented in Table 2.4.

Table 2.4: List of glass compositions successfully crystallized by pulsed laser irradiation, and references therefor. An even more extensive list may be found in a review paper by Musgraves [2] and the references therein.

Glass Composition	**Crystal**	**Laser**	**Rep. Rate**	**Pulse Width**	**Reference**
33.3BaO-16.7TiO_2-50SiO_2	$Ba_2TiSi_2O_8$	Ti:Sapphire	250kHz	150fs	[71]
40SrO-20TiO_2-40SiO_2	$Sr_2TiSi_2O_8$	Ti:Sapphire	250kHz	150fs	[72]
33.3BaO-16.7TiO_2-50GeO_2	$Ba_2TiSGe_2O_8$	Ti:Sapphire	250kHz	150fs	[73]
Forturan	Forturan	Ti:Sapphire	1kHz	170fs	[74]
32.5BaO-32.5TiO_2-35SiO_2	Ba_2TiO_4	Ti:Sapphire	200kHz	120fs	[75]
47.5BaO-5Al_2O_3-47.5B_2O_3	β-BaB_2O_4	Ti:Sapphire	200kHz	130fs	[69]
25La_2O_3-25B_2O_3-50GeO_2	$LaBGeO_5$	Ti:Sapphire	250kHz	70fs	[79]
various	$LiNbO_3$, $BaTiO_3$	Ti:Sapphire	200kHz	120fs	[77]
0.5Er_2O_3-33.3BaO-16.7TiO_2-50SiO_2	$Ba_2TiSi_2O_8$	Ti:Sapphire	250kHz	150fs	[78]
25La_2O_3-25B_2O_3-50GeO_2	$LaBGeO_5$	KULON-10CU-M (510.6, 578.2nm)	13kHz	10-25ns	[81]

2.4.3 General phenomena of laser induced crystallization

Concerning the patterned crystalline architectures by both CW and pulsed lasers, most work has focused on dots and/or straight lines [41–47, 51, 52, 54, 58–61, 63, 70] and [68, 69, 71–78]. A few have studied abrupt [57, 79, 80] and smooth [49, 57] bends in crystal lines created by altering the laser scanning direction. Finally, Suzuki [64] and Honma [56] have grown 2D planar crystals by rastering the laser focus across the sample surface with sufficient overlap at each pass. In the cases of linear and planar structures, Raman spectroscopy confirms that the crystals are highly oriented, with the c-axis aligned in the plane of the sample surface and parallel to the laser scanning direction [42, 51, 52, 56, 58, 60, 64, 70]. Interestingly, Ihara *et al.* [57] found that when the laser scanning direction is abruptly changed, the orientation gradually and continuously realigns itself in order to remain parallel to the growth direction. This effect was also observed by Stone *et al.* for bend angles less than 27° [79].

A number of interesting and noteworthy effects have been observed during laser-induced crystallization. First, in order to alleviate the steep thermal gradients which occur both spatially and temporally during the irradiation process and thereby prevent cracking of the sample, a number of workers found performing the irradiation in an elevated (150°C-500°C) ambient temperature environment to be helpful [49,51,61,63,79]. Second, the glass surface can provide many heterogeneous nucleation sites and favors crystallization due to its higher cooling rates [48]. This fact forces the requirement of a very tightly focused beam in order to produce single crystal lines. If the focus is broad, then the temperature gradient will not be sharp and competing crystals may nucleate as the crystal is grown [60]. Finally, as might be expected due to the thermal gradient at the laser focus and frequently off-stoichiometric glass compositions, multiple crystalline phases have been observed at different positions within one crystalline spot [45, 47, 76, 79].

The appearance of multiple crystalline phases within the laser-irradiated spot is some-

what unsurprising in the case of femtosecond-laser crystallization, as elemental gradients can be established due to shock waves or pressure waves resulting from the rapid temperature change [82], microexplosions [83], or ponderomotive forces [79] at the laser focus. Stone *et al.* [79] observed an unidentified La-rich, B-depleted crystalline phase within stoichiometric $LaBGeO_5$ glass. Yonesaki *et al.* [77] observed inward migration of Si and outward migration of Nb in one glass composition and inward migration of Al and outward migration of Ba in another glass composition. Though a potential complication, elemental redistribution could also be thoughtfully induced with potential applications in mind. Though no crystallization was observed, Shimizu [84] and Sakakura [85] demonstrated the ability to control and create novel elemental distributions within the laser focus via the use of a spatial light modulator (SLM).

Finally, though rare-earth elements are common components in glasses for CW laser-induced crystallization, they are unnecessary for pulsed laser-induced crystallization.Therefore, only one instance [78] of this type of crystallization in a glass containing rare-earths has been published. Basic fluorescence properties of the respective rare earth ions within either CW or pulsed laser-induced crystals have been reported [52, 59, 78]. Honma *et al.* [52] reported that the fluorescence intensity of the rare earth is less within the crystal compared to that of the surrounding glass. Conversely, Komatsu *et al.* [59] observed brighter fluorescence from the crystallized region. In addition to influencing the optical properties of the resulting crystal, rare earth dopants also have the potential to affect the crystallization process itself during pulsed laser irradiation. Specifically, Zhu *et al.* [78] reported that rare earth-doped glasses required significantly longer irradiation times compared to their undoped counterparts under identical irradiation conditions. This was attributed to energy being siphoned away from the heating process via upconversion luminescence.

2.5 The electronic structure of Er^{3+}

Though Pr, Nd, and Er were all utilized in this work, by far the most effort was expended on erbium. For that reason, it is important to understand the electronic structure of Er and the notation used to describe its energy levels, as well has how the former is influenced by the surrounding environment when in a glass or crystal.

In a neutral erbium atom there are 68 electrons and the full electron configuration is $1s^2 2s^2 2p^6 3s^2 3p^6 3d^{10} 4s^2 4p^6 4d^{10} 5s^2 5p^6 4f^{12} 6s^2$, which is typically shortened to $[Xe]4f^{12}6s^2$, where [Xe] denotes the electron configuration of xenon. In reality, it is much more common for the erbium to be in the triply-ionized, or trivalent, state, in which both 6s electrons and one 4f electron are removed. This leaves the configuration as $[Xe]4f^{11}$. It is important to note that the 5s and 5p shells, which have a larger radial extension than the 4f shell, remain fully filled. This serves to shield the 4f electrons from extra-ionic influences, and therefore, when erbium is incorporated in a crystal, the crystal field is only able to weakly affect them. Thus, rather sharp emission lines from erbium, and all other rare earth ions, are observed in crystals.

To begin to qualitatively understand the energy level structure, a good starting point is the Hartree approximation, which considers the influence on an optically active electron due to the average of all the Coulomb interactions with other electrons in the system. However, the Hartree approximation ignores many weaker interactions which remove degeneracies. In order to compensate for this, the residual Coulomb interaction and the spin-orbit interaction must be accounted for. When the former is stronger, the individual orbital angular momenta of the optically active electrons couple to form a total orbital angular momentum for the system. Similarly, the individual spin angular momenta couple to form a total spin angular momentum for the system. The effect of this is that the magnitude of both the total orbital and spin angular momenta remain constant, and the lowest energy states

are usually those with the largest spin angular momentum and largest total orbital angular momentum. This situation is referred to as *LS*-coupling, or Russell-Saunders coupling. As the atomic number of the atom being considered increases, the spin-orbit interaction needs to be considered. This interaction couples the total orbital angular momentum to the spin angular momentum such that the magnitude of their vectorial sum, the total angular momentum, is constant. This is referred to as *JJ*-coupling and in this case the states with lowest energy have the smallest total angular momentum.

Unfortunately, for Er^{3+}, neither interaction dominates and both must be considered. Additionally, because the 4f shell is more than half-filled in erbium, the optically active entities are actually the three holes. This is an important distinction when determining which states have the lowest energy as the behaviors will be reversed. For the three f-shell holes under *LS*-coupling, the total orbital angular momentum can be $L = 0, 1, 2, ..., 8, 9$. However, the Pauli exclusion principle states that no two fermions can have the same set of quantum numbers, and thus $L = 9$ must be eliminated. Similarly, the total spin angular momentum can be $S = \frac{1}{2}, \frac{3}{2}$. This results in the 4f configuration being split into several Coulomb interaction terms. These terms are subsequently split into multiplets by the spin-orbit interaction based on the total angular momentum, J, which has possible values in the range $|L - S| \leq J \leq |L + S|$. The multiplets are typically denoted as $^{2S+1}L_J$. Given the values discussed earlier, erbium has 42 multiplets. Those relevant to this work are shown schematically in Figure 2.6. As seen in the figure, the lowest energy state is the $^4I_{15/2}$ multiplet. This corresponds to the largest combination of $L = 6$ and $S = \frac{3}{2}$ as predicted by the Coulomb interaction and the largest $J = \frac{15}{2}$ as predicted by the spin-orbit interaction, and the fact that the optically active entities are holes. Also shown in Figure 2.6 are the splittings of the multiplets into their Stark sublevels due to the small perturbation felt when in a crystal field. The number of Stark sublevels into which the multiplets split, and the energy differences between them, depends on the structure and symmetry of the crystal,

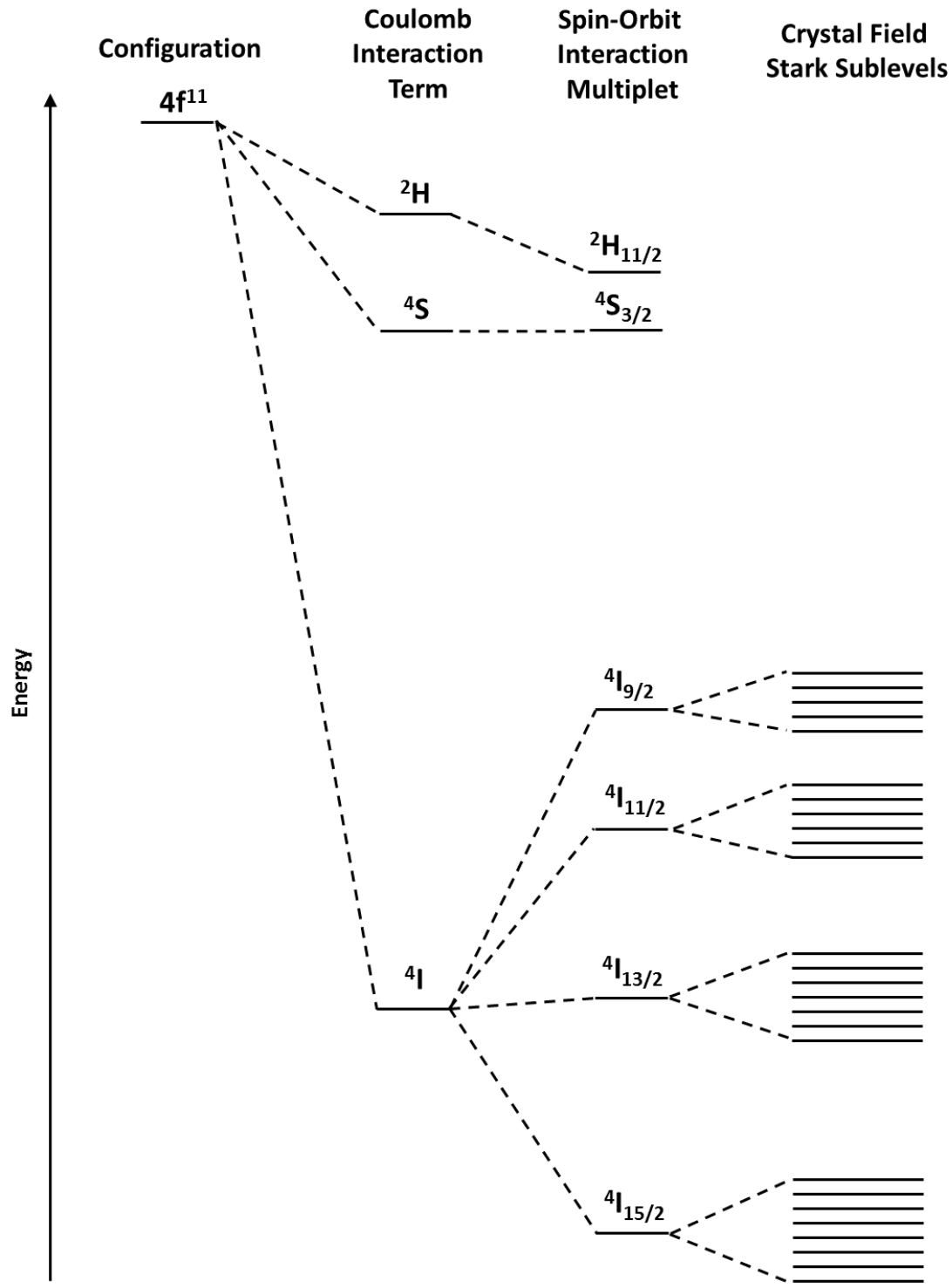

Figure 2.6: Energy scheme of the relevant levels of Er^{3+}. The energy differences are not to scale and are for reference only.

but is at maximum $J + \frac{1}{2}$ when J is a half integer, as in erbium.

2.6 Confocal microscopy

Confocal microscopy is a powerful imaging technique due to its ability to improve image quality by preventing light originating from outside the plane of focus from being collected. This is particularly useful for studying samples in which the region of interest lies within the bulk of the sample, as in laser-induced crystals in glass. By scanning the sample, high resolution 3D maps of an interior volume of a sample can be created point-by-point. The difficulty with this technique is therefore that it is extremely time consuming to both collect and analyze hundreds of thousands of spectra per scan. Nevertheless, this technique was utilized because important structural information can be found within the level of detail it provides, though scans were limited to 2D to save time.

Figure 2.7 illustrates the working principle of a confocal microscope. Typically, a monochromatic light source is directed through a pinhole in order to create a point source. This point source is then imaged onto the sample by an objective. However, due to aberration and the diffraction limit, the image of the point source is not a perfect point. Instead, the point becomes a three-dimensional intensity distribution, referred to as a point spread function (PSF). According to Abbe [86], two points are resolved when the maximum of the PSF of one point coincides with the first minimum of the PSF of another point. The separation distance turns out to be the radius defining the position of the first dark circular ring surrounding the central Airy disc, which, in turn, corresponds to the first zero of the first-order Bessel function. Performing these calculations, the lateral resolution of the microscope is

$$r_{lateral} = 0.6098\frac{\lambda}{NA}, \tag{2.22}$$

with λ being the wavelength of the excitation light and NA being the numerical aperture of

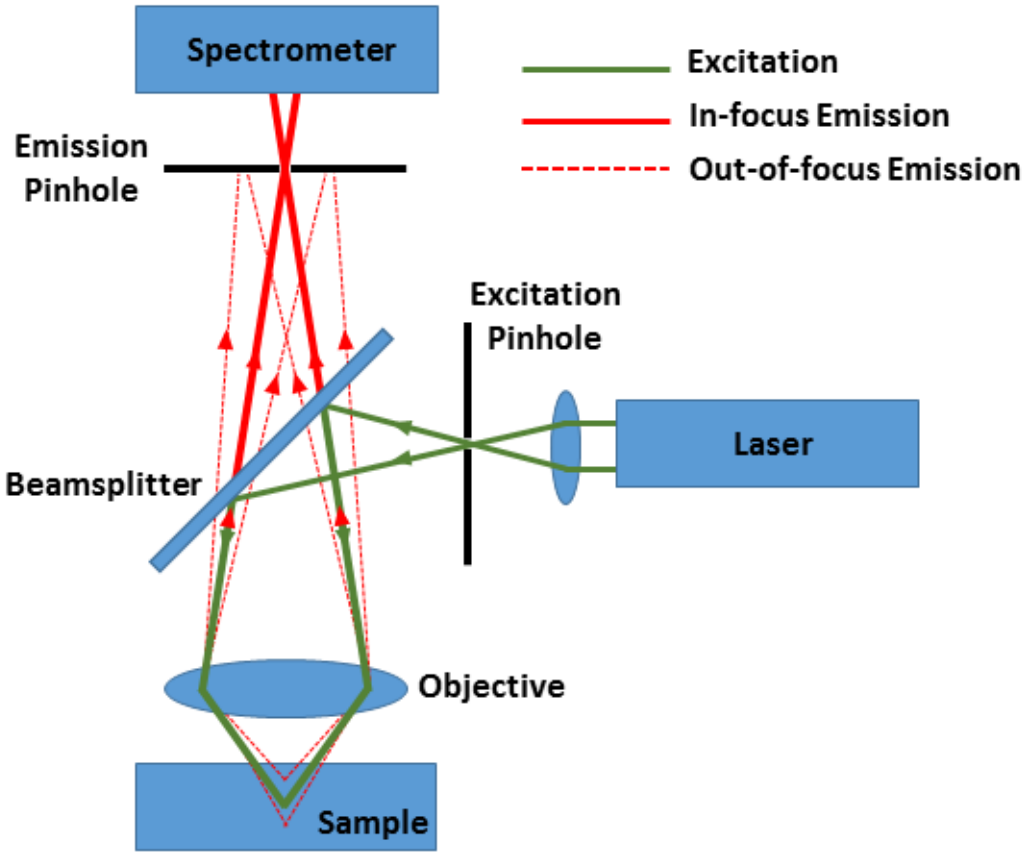

Figure 2.7: Schematic of a confocal microscope illustrating how spatial filtering by pinholes limits axial resolution by removing out-of-focus light.

the objective lens.

In widefield microscopy, there is no well-defined axial resolution. However, by placing a pinhole into the emission beampath before the detector, axial resolution may be realized. In the idealized case where the excitation and emission wavelengths are the same, the PSF of the emission pinhole will be identical to that of the excitation pinhole and will overlap, making the microscope confocal. The effect of this second pinhole is therefore to spatially filter the emission in order to eliminate out-of-focus light. This yields an axial resolution [87] of

$$r_{axial} = 2\frac{n\lambda}{NA^2}, \tag{2.23}$$

where n is the index of refraction of the material.

Chapter 3

Experimental Techniques

3.1 Raman spectroscopy and electric fields

Due to the fact that ferroelectric materials are also piezoelectric, the presence of an electric field induces a distortion of the crystal structure, which thereby induces a corresponding shift in energy of the Raman modes. Therefore, by measuring this effect quantitatively via the magnitude and direction of the shifting of particular Raman modes under different experimental conditions, information concerning the internal structure of the unperturbed material may be gained. Two different approaches toward this goal were utilized, including the application of an external electric field at room temperature, or allowing a space charge-induced electric field to accumulate due to the probe laser at low temperature.

In both cases the excitation source is an argon ion laser operating at $488nm$. The laser is coupled into a single mode fiber which guides the laser to the microscope, at which point it is collimated and a laser line filter eliminates unwanted wavelengths created in the fiber. The beam passes through a 50:50 beamsplitter and is focused onto the sample by a 100x/0.5NA microscope objective. The emission is collected in the backscattering geometry by the same objective and is reflected by the beamsplitter. A $488nm$ long-pass filter removes the Rayleigh scattered light before the emission is coupled into a multi-mode fiber and brought to a $50cm$ focal length spectrometer and CCD detector.

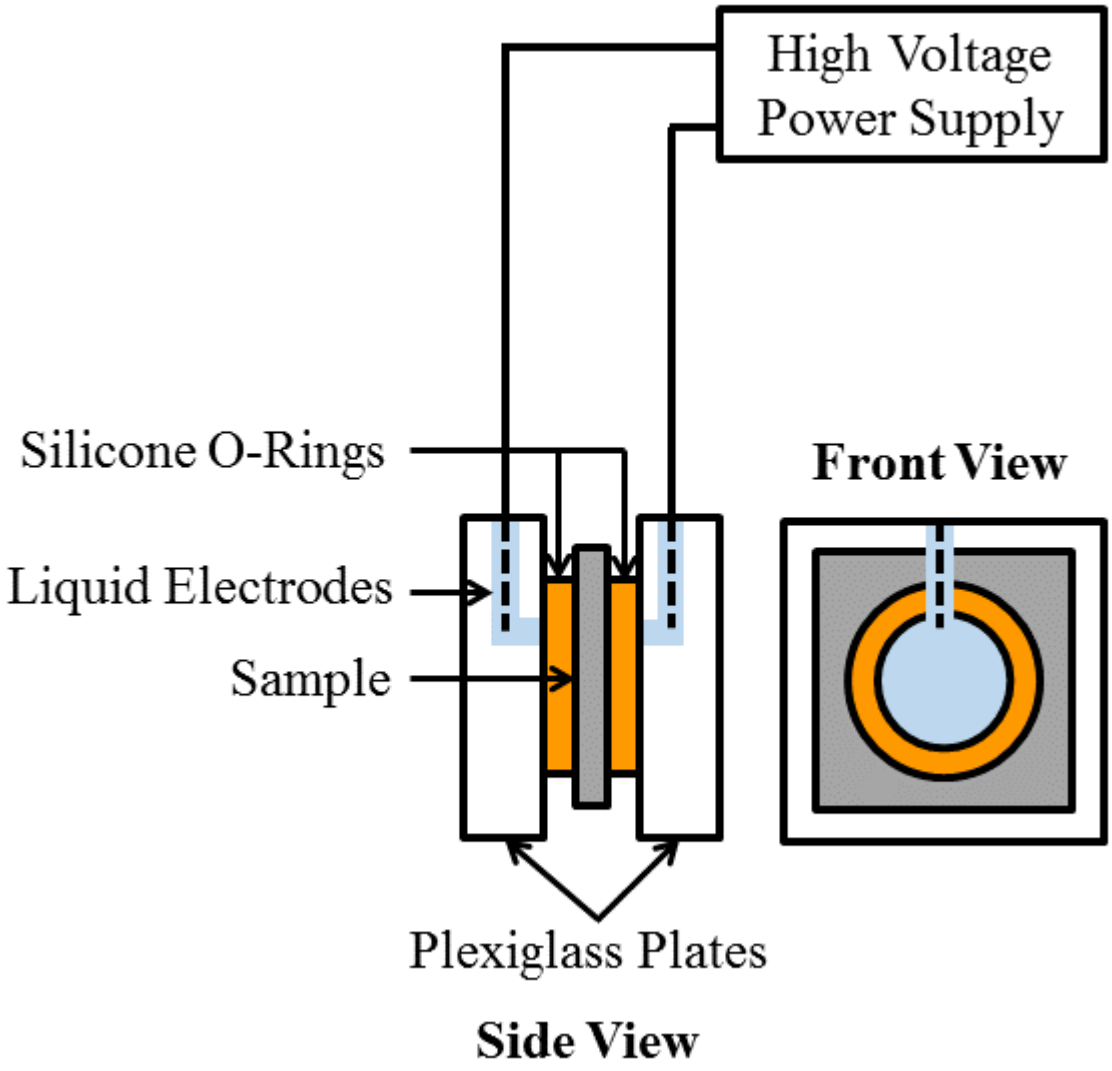

Figure 3.1: Schematic diagram of the sample holder used to apply an electric field to a sample while simultaneously performing spectroscopy.

3.1.1 Applied electric fields and domain inversion

In order to apply an electric field to the sample a custom sample holder which allows *in-situ* Raman spectroscopy was designed and built by Dr. Christian Sandmann. This sample holder is sketched in Figure 3.1. The sample is sandwiched between two silicone o-rings which, in turn, are sandwiched between two transparent plexiglass plates. Holes drilled from the top-down and face-in in the plexiglass plates are filled with tap water. The water, which contains sufficient impurity ions to be slightly conducting, fills the cavity within the center of the o-ring between the plexiglass and the sample and thus serves as the electrodes. Leads from a high voltage power supply are inserted into the water within the plexiglass. This configuration allows an electric field to be applied while maintaining a sizable viewing window through which to perform spectroscopy. The high voltage is passed through a $100M\Omega$ resistor in order to limit the current through the sample. In general, the voltage is ramped up at a rate of $0.045kV/s$ while spectra are continuously collected with very short exposure times.

3.1.2 Probing space charge fields

For probing space charge-induced electric fields, the samples are brought to low temperature in a high vacuum environment in order to prevent the charge from dissipating. Therefore, the samples are mounted to a copper cold finger inside of a liquid helium-cooled cryostat and brought to around $10K$. Spectra are continuously collected as the probing/modifying laser is turned on and allowed to irradiate the sample for a length of time. In order to prepare the sample for subsequent experiments, the temperature is raised to $200K$ and then lowered back to $10K$ to allow the accumulated charge to dissipate.

3.2 Scanning confocal Raman and fluorescence microscopy

Figure 3.2 depicts the schematic of the experimental setup designed and built by Dr. Greg Stone for the purposes of performing scanning confocal Raman spectroscopy. The excitation source is an argon ion laser operating at $488nm$. The laser is coupled into a single mode fiber which guides the laser to the microscope. This fiber is wound through fiber paddles which are used to apply strain in order to rotate the orientation of the polarization of the light exiting the fiber. Upon exiting the fiber, which serves as the first pinhole of the confocal microscope, the beam is collimated and passes through a laser line filter and a polarizer. The laser line filter eliminates unwanted wavelengths created in the fiber and the polarizer sets the polarization to the desired orientation with respect to the sample (with the aforementioned paddles being used to maximize throughput at that polarization orientation). A 45° dichroic mirror reflects greater than 99% of the beam into the back aperture of a 50x/0.75NA microscope objective which focuses the beam onto the sample. The remaining portion of the laser beam which passes through the dichroic mirror is coupled into a multimode fiber and brought to a power meter. The emission is collected in the 180° backscattering geometry by the same objective, and that with wavelengths longer than the cutoff wavelength of the dichroic mirror, corresponding to the Stokes lines, is permitted to pass through. Based on the choice of the 50x/0.75NA objective, the excitation wavelength of $488nm$, and Equations 2.22 and 2.23, the theoretical lateral and axial resolutions of the microscope are $400nm$ and $1.74\mu m$, respectively.

The sample rests on a glass slide supported by a nano-positioning piezoelectric stage which allows for precise movement in the x-, y-, and z-directions. Each direction of travel is capable of step sizes down to $1nm$ over a range of $100um$ The glass slide allows the sample to be backlit by a white light source. This white light is also collected by the objective and passes through the dichroic mirror with the Stokes Raman emission, at which

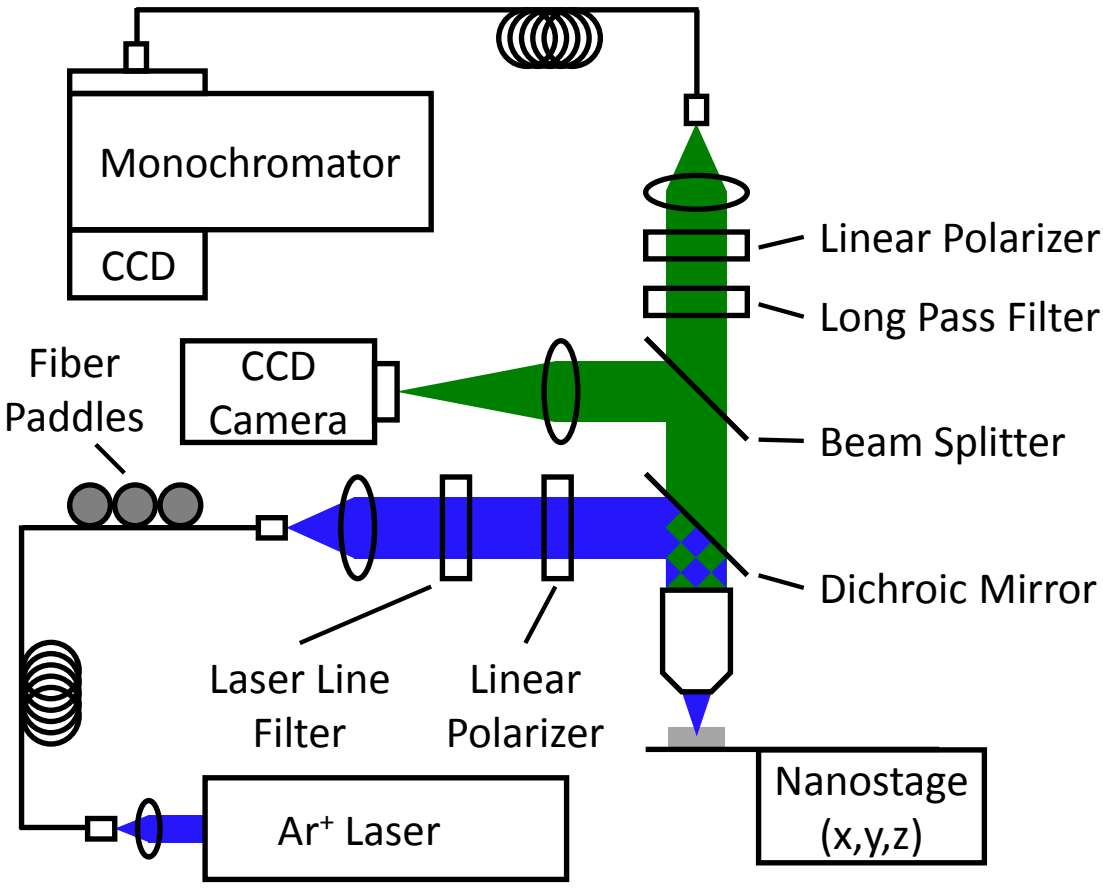

Figure 3.2: Diagram of the scanning confocal Raman and fluorescence microscope.

point a 92:8 beamsplitter reflects 8% of the white light toward a lens and CCD camera. The CCD camera allows the features of the sample to be visualized and positioned appropriately relative to the scan area. During a scan the white light is turned off. A long-pass Raman filter removes any laser light that made it through the dichroic mirror and passes the Stokes Raman emission. An optional polarizer may be placed into the beampath to selectively collect emission with a particular polarization orientation. The emission is then coupled into a single mode fiber, which acts as the second pinhole of the confocal microscope. The fiber guides the emission to a spectrometer and CCD array (see note at end of section). The light exiting the fiber is focused onto the entrance slit of the spectrometer. Since the slit width and length of the spectrometer determine the spectral resolution, the slit width was generally matched to the core diameter of the fiber. All of the equipment was controlled by a computer using LabView software. The emission wavelength scale for each scan was calibrated using known emission wavelengths of both neon and xenon gas arc lamps.

Note on spectrometer/CCD change

Due to the low intensities of Raman scattering emission, long integration times are necessary. Coupling this with the relatively large dimensions of the areas to be scanned, it was determined that it would be beneficial to switch from a liquid nitrogen cooled CCD array which had to be periodically refilled to a thermoelectrically cooled model which could run continuously. The pixel array size for both models is 1300 $\times$ 100. On the other hand, the spectrometer used with the liquid nitrogen cooled CCD has a length of $50cm$, while the spectrometer used with the thermoelectrically cooled CCD has a length of $15cm$. Since both spectrometers have gratings with $1200g/mm$, the spectral resolution of the latter is somewhat poorer. However, since we were interested in comparing the spatial profiles of the crystallinity (via the Raman emission) to the rare earth dopant profile (via fluorescence), the shorter spectrometer was deemed appropriate because it offers a wider spectral range within a single spectrum. The reader should therefore note that the data concerning

$LiNbO_3$ presented in Chapter 4, as well as some of the preliminary observations concerning laser-induced crystals in $Er_{.002}La_{.998}BGeO_5$, were collected using the $50cm$ spectrometer. Unless otherwise noted, all of the room temperature Raman and fluorescence data concerning RE:$LaBGeO_5$ were collected using the $15cm$ spectrometer.

3.3 Combined Excitation Emission Spectroscopy (CEES)

CEES measurements were performed on both furnace crystallized glasses and laser-induced crystals in glass. A tunable diode laser is coupled into a single mode fiber. A glass slide before this fiber reflects a small fraction of the beam toward a separate fiber coupler and multimode fiber. This multimode fiber is attached to a wavemeter which is used to read the wavelength of the laser as it is changed throughout the course of a CEES scan. After the main portion of the beam exits the single-mode fiber at the microscope, it is collimated and then reflected by an $1150nm$ long-pass dichroic mirror. A 20x/0.4NA microscope objective focuses the beam onto the sample. The emission is collected in the backscattering geometry by the same objective, passes through the dichroic mirror, and is coupled into either a multimode or single mode fiber, depending on the situation. The light exiting this fiber is focused onto the entrance slit of a $50cm$ focal length spectrometer. An InGaAs detector records the spectra.

The sample is mounted onto a cold finger inside of a helium-cooled cryostat and brought to a temperature around $10K$. Once the sample is at low temperature, the excitation laser wavelength is changed in steps of $0.02nm$, and an emission spectrum is collected at each step. For erbium doped samples, the excitation wavelength is typically tuned from $963nm$ ($1.2876eV$) to $988nm$ ($1.2550eV$). Because the spectral range provided by the combination of the $50cm$ spectrometer and $600g/mm$ grating is insufficient to capture the entire emission range, each scan is performed twice such that the total emission range spans from

1578.07nm (0.78577eV) to 1513.76nm (0.81915eV). A semiconductor tunable external cavity laser is used to calibrate the emission wavelength scale.

Using this technique, a 2D map of the incorporation environments (also commonly referred to as "sites") of the emitting ion of interest in excitation/emission space can be created. In this mapping scheme, a single emission line resulting from a single absorption will appear as a lone, circular bright spot. If the ion is incorporated at a single type of environment within the structure of a crystal, the anisotropic electric field arising from the long-range order of the crystal will induce Stark splitting of the single excitation/emission peak. This splitting manifests in a CEES map as a regularly spaced matrix of bright spots, the number of which is determined by Group Theory according to the symmetry of the incorporation environment. Each row or column of the matrix will have an identical profile, respectively. If, on the other hand, the ion of interest is incorporated in multiple environments, then the crystal field felt in each case will be different and thereby induce different Stark splittings. The CEES map in this case will exhibit different excitation, or emission, profiles. It should be noted that different sites can be caused by incorporation at different lattice positions or by different perturbing ions in different positions which are in close proximity to the ion of interest. Finally, circular peaks occur only when no sources of inhomogeneous broadening are present. When the material is strained, the excitation/emission peaks will undergo fluorescence line narrowing, and the CEES map will show tilted, elliptical bright spots. This occurs because the strain shifts certain transitions within certain subsets of ions such that their selective excitation is possible. Thus, depending on the excitation photon energy, it is possible to receive emission from either all fluorescing ions, or only a subset. Similarly, the opposite is also true, and a particular excitation energy can result in emission at one energy which comes from all fluorescing ions and emission at another energy which comes from a subset. Figure 3.4 illustrates the effect of fluorescence line narrowing.

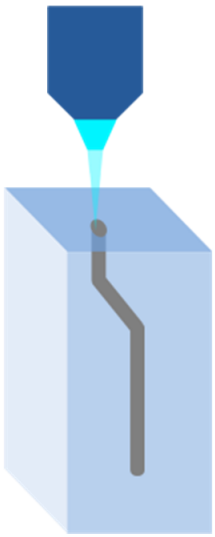

Figure 3.3: Illustration of the geometry used for both scanning confocal Raman and fluorescence microscopy and CEES measurements. The samples were diced perpendicular to the growth direction of the laser-induced crystals such that the probe laser was incident parallel to the growth axis (c-axis).

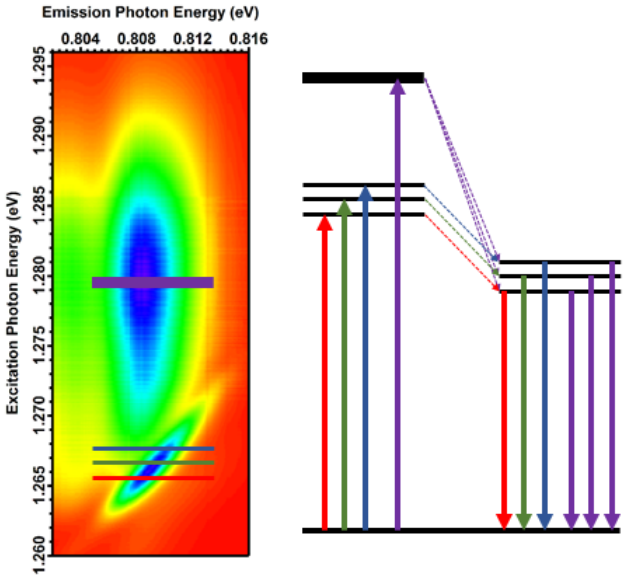

Figure 3.4: An example of fluorescence line narrowing. Depending on the excitation energy, emission from either all (purple) or only certain subsets (red, green, blue) of the fluorescing ions will be observed.

3.4 Laser induced crystallization

3.4.1 Sample preparation

Glass samples of various compositions were prepared via the normal melt-quenching technique. High purity La_2O_3, H_3BO_3, GeO_2, Er_2O_3, Nd_2O_3, and Pr_2O_3 reagents were used. Reagent powder weights were determined in order to produce final glass weights of $20g$ with the desired composition while also compensating for the $1.9wt\%$ B_2O_3 loss reported by Sigaev *et al.* [27]. Each batch was mechanically mixed for at least five hours and the same melting, pouring, and annealing procedure was used for each composition. Melting was performed in a platinum crucible. The temperature was increased at a rate of $10°C/min$ to 1250°C with 30 minute holds at 800°C and 1250°C. The melt was then quenched between two steel plates pre-heated to 500°C and annealed for two hours at 650°C. The resulting glasses were then cut using a diamond wafering blade and polished to optical quality using a progression of SiC polishing discs and diamond lapping films. The final polishing step utilized a cloth pad and CeO_2 abrasive powder in water. Once the laser crystallization process had been performed such that crystal lines were grown through the samples, the samples were cut perpendicular to the line growth direction so as to expose the crystalline cross-sections and polished using the same procedure as before laser irradiation.

In order to compare the laser crystallization process to more conventional bulk crystallization techniques, small pieces of the each glass composition produced were placed back into the furnace and heated to 670°C for two hours in order to stimulate crystal nucleation. The temperature was then ramped to 850°C for seven hours to allow the nucleated crystals to grow throughout the entire sample. This process yielded the bulk polycrystalline samples shown in Figure 3.5.

Figure 3.5: RE:LBGO glasses before (left) and after (right) furnace crystallization. Compositions (L to R): Row 1: Erbium, 1%, 4%, 10%, 20%, Row 2: Praseodymium, 0.2%, 1%, 4%, 10%, 20%, Row 3: Neodymium, 0.2%, 1%, 4%, Row 4: Neodymium, 10%, 20%

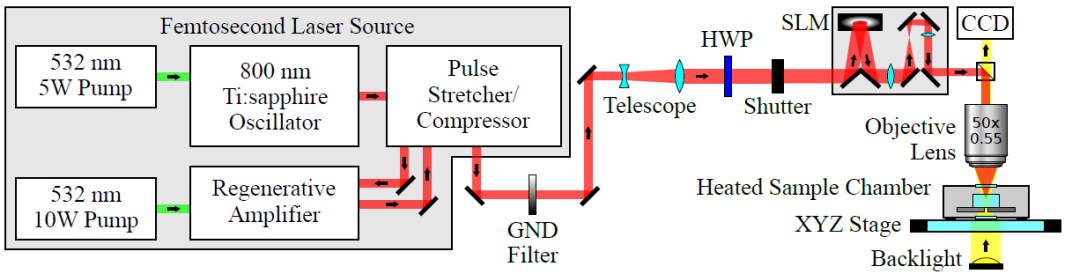

Figure 3.6: Diagram of the setup for aberration-corrected pulsed laser irradiation. Reproduced from A. Stone [5].

3.4.2 Laser Irradiation

The laser irradiation process occurred at Kyoto University in Kyoto, Japan, using the setup diagrammed in Figure 3.6. A regeneratively amplified Ti:Sapphire pulsed laser with a wavelength of $800nm$, a pulse rate of $250kHz$, and a pulse width around $60fs$ was used. A graduated neutral density filter provided coarse control of the laser intensity. Beam expanding optics and a half-waveplate allowed the use of a liquid crystal on silicon spatial light modulator (LCOS-SLM). The SLM was used to induce compensatory phase shifts throughout the radial distribution of the beam in order to correct for spherical aberration caused by the heating chamber window and the sample material above the desired focal point. Following the SLM, a 50x/0.55NA microscope objective focused the beam onto the sample, which was mounted inside a heating chamber. During irradiation, the sample was heated to $500^{\circ}C$ in order to help relieve thermal stress and prevent cracking. A small fan was used to reduce the effects of hot air convection above the heating stage on beam stability. Finally, the heating stage was mounted to an XYZ translational stage. A backlight and CCD camera allowed *in-situ* observation of the sample. Further details concerning the laser irradiation technique may be found in the Ph.D. dissertation of A. Stone [5].

In each new sample, a seed crystal was created by continuously irradiating a single spot until nucleation occurred. The conditions which resulted in crystal nucleation in the erbium-doped $LaBGeO_5$ glasses described in Section 3.4.1 are presented in Table A.1 in Appendix A. Somewhat surprisingly, the conditions required for this process varied not only from composition to composition, but between samples of the same composition. Once a crystal had been nucleated, a seed line from which all other lines were grown was produced. Subsequent to the appearance of the initial seed crystal, the conditions under which crystal growth could be achieved were much more flexible. Crystalline lines were grown from these seed lines while systematically varying the laser power, focal depth, and sample translation speed. Series of experiments were performed in which these three pa-

rameters were varied for both aberration-uncorrected and aberration-corrected conditions.

3.5 Data evaluation with IGOR Pro

The data resulting from the experimental techniques described in this chapter were evaluated using a variety of OEM and custom procedures in the IGOR Pro software package. These procedures enabled easy visualization of the very large amount of information contained in the acquired data sets such that they could be qualitatively compared and quantitatively analyzed. In particular, the curve fitting feature was invaluable in almost every aspect of this work.

In theory, the observed Raman and fluorescence peaks should exhibit a Voigt profile, which is the convolution of a Gaussian profile and a Lorentzian profile. Raman modes within a crystal are homogeneously broadened according to their finite lifetimes and any strain present. On the other hand, the excitation laser linewidth is influenced by inhomogeneous broadening effects. Additionally, other experimental parameters including the optics and CCD detector will result in a final linewidth which is broadened. However, since the homogeneous broadening is approximately two orders of magnitude greater than the inhomogeneous broadening, and the convolution of the two different profiles is computationally expensive, peaks were fitted to a simple Lorentzian profile according to

$$f(x) = A + B\frac{D^2}{(x-C)^2 + D^2}, \tag{3.1}$$

where A,B,C, and D are the fitting parameters. For the purposes of assigning peak characteristics, D must be positive. Thus A is the baseline, $\pi \cdot B \cdot D$ is the area under the peak, C is the position of the peak, and $2 \cdot D$ is the full width-half max (FWHM) of the peak.

By defining a fitting function to accommodate an arbitrary number of Lorentzian peaks of the form in Equation 3.1 and then iteratively fitting the spectra from each point in a 2D

scan, the spatial behavior of each fitting parameter could be mapped. This allowed instant visualization of how the peak position and FWHM, and correspondingly the structure, varied across a crystal cross-section. Furthermore, by comparing these maps to similar maps of the integrated erbium fluorescence, variations in the latter could be correlated, or not, to changes in the crystal structure.

Chapter 4

Electric Fields in $LiNbO_3$

4.1 Externally applied electric fields

In-situ Raman spectroscopy was performed on various $LiNbO_3$ samples during application of an external electric field which induced ferroelectric domain inversion. While the external electric field was being applied the frequencies of the Raman modes were observed to shift proportionally to the field strength. Following domain inversion the zero-field frequencies of the Raman modes were shifted from their values in the as-grown state. The former effect is a simple consequence of the piezoelectricity of $LiNbO_3$, and can be used as a calibration of other effects in other situations. The zero-field frequency shift is related to the existence of an intrinsic internal electric field due to intrinsic defects such as the lithium vacancy model discussed in Section 2.1.

The lithium vacancies possess dipole moments parallel to the spontaneous polarization along the ferroelectric axis of the crystal. However, while the spontaneous polarization may be reversed during domain inversion, the defect dipole moments are not. This means that the spontaneous polarization and net sum of the defect polarizations will combine constructively in the as-grown state and destructively in the domain inverted state. In order to better understand this effect, it is convenient to consider a mono-domain crystal in the as-grown state which contains a number of defects. This state is labeled V and has a

spontaneous polarization, $+P_S$, as well as a defect polarization, $+P_D$, which is the net sum of the contributions from every defect present. The domain inverted state is labeled R and has a spontaneous polarization, $-P_S$. In this case, however, the defect polarization remains $+P_S$. The nomenclature of forward poling refers to switching state V to state R, while backward poling switches state R to state V.

Based on the notion that the spontaneous and defect polarizations can add either constructively or destructively, the coercive fields required to induce forward or backward poling will inevitably be different for crystals with large numbers of defects. Using this information, the internal electric field due to the defects can be determined according to

$$E_{defect} \sim \frac{E_F - E_B}{2}, \tag{4.1}$$

in which E_F and E_B are the threshold coercive fields required for forward and backward poling, respectively [88]. This method for determining the internal defect electric field provides a reasonable estimate, but suffers overall because of its dependence on the value of the coercive fields, which in turn depend on the domain nucleation rate and motion of the domain wall. In order to determine a more accurate value of the internal defect field, changes to the electronic structure of rare earth dopants following domain inversion were calibrated against changes during application of an external electric field by Dierolf *et al.* [89,90]. Unfortunately, introducing erbium ions as probes results in additional polar defects within the crystal. Thus, while the determined value of the internal field is likely extremely accurate, it cannot also be attributed to crystals without erbium. Therefore, the purpose of this work was to use Raman spectroscopy, which is non-destructive and does not require the inclusion of additional polar defects, in the same manner as Dierolf *et al.* used fluorescence spectroscopy in order to probe the magnitude of the internal defect polarization.

Beyond the details discussed in Section 3.1.1, the experiments proceeded as follows. The crystals used were z-cut wafers of congruent and stoichiometric $LiNbO_3$ with dimen-

sions 10mm $\times$ 10mm $\times$ 0.5mm which were purchased from MTI Corporation and Deltronic Crystal Industries, respectively. Before being placed into the poling setup shown in Figure 3.1, the direction of the ferroelectric polarization within each crystal was determined by measuring the induced voltage along the c-axis when heated. Using this information, the electric field could be applied in the correct direction during each step of the experiment. Each sample was subjected to the same series of steps, denoted as R1, R2, R3, and R4. The initial and final states of the crystal, as well as the direction of the external electric field during each step, are listed in Table 4.1. In the table, all signs are relative to the direction of the ferroelectric axis in the virgin crystal. In each step the applied voltage began at $0kV$ and was ramped at $0.045kV/s$ to a predetermined value or until domain inversion occurred (in steps R2 and R4), after which the field was quickly removed. During each step, Raman spectra were collected continuously at two second intervals. Forward poling was observed when the applied electric field reached $23.4kV/mm$ and $4.2kV/mm$ in congruent and stoichiometric $LiNbO_3$, respectively. Backward poling occurred at $17.8kV/mm$ and $3.6kV/mm$, respectively.

Table 4.1: Initial and final states of the crystal, as well as the orientation of the applied electric field relative to the ferroelectric axis in the virgin crystal, for each step of the experiment.

Step	Initial State	Applied Field	Final State
R1	$V\ (+P_S, +P_D)$	$+E_{ext}$	$V\ (+P_S, +P_D)$
R2	$V\ (+P_S, +P_D)$	$-E_{ext}$	$R\ (-P_S, +P_D)$
R3	$R\ (-P_S, +P_D)$	$-E_{ext}$	$R\ (-P_S, +P_D)$
R4	$R\ (-P_S, +P_D)$	$+E_{ext}$	$V\ (+P_S, +P_D)$

As an example, the behavior of the $E(TO)_1$ Raman mode frequency over the entire sequence is shown in Figure 4.1. Similarly, the frequency of each Raman mode could be plotted as a function of the applied electric field, as in Figure 4.2. The data of Figure 4.2 was fit to the function $y = \alpha + \beta E_{ext}$, where α is the zero-field frequency of the Raman mode

of interest and the slope, β, quantifies the frequency response due to the applied field, E_{ext}. The coefficients for the chosen Raman modes in both the as-grown and domain-inverted states are tabulated in Table 4.2.

Interestingly, Figure 4.2 and Table 4.2 show that the response of some Raman modes is characterized by a positive slope, while others exhibit a negative slope. Additionally, the zero-field frequencies of the Raman modes are shifted from their as-grown values following domain inversion. It is important to note that these frequencies return to their original values following a second domain inversion which returns the crystal to its as-grown state, as this is a necessary requirement in order for the technique to be reliable.

Table 4.3 compares the frequency shifts due to domain inversion observed experimentally (calculated as the difference between $\alpha_{as-grown}$ and $\alpha_{domain-inverted}$ in Table 4.2) to the "theoretical" value (calculated by entering the experimentally observed coercive fields into Equation 4.1 and multiplying by the appropriate β) for each Raman mode. While Table 4.2 shows that β is virtually unaffected between congruent or stoichiometric samples, the same cannot be said concerning the magnitude of the frequency shifts due to domain inversion, which are an order of magnitude larger in congruent $LiNbO_3$. Furthermore, there is a significant difference between the experimentally observed shifts and the calculated value based on the coercive fields that cannot be explained by experimental error.

In order to understand the source of this discrepancy, it is instructive to reverse the calculation to determine the magnitude of the internal electric field required to produce the experimentally observed frequency shifts. The results of this calculation are presented in Table 4.4 and indicate that a different field strength for each Raman mode in a particular sample is required. However, because the dipole axes of the proposed defect models lies completely parallel to the ferroelectric axis of the crystal, the required field should be the same for every mode. Furthermore, this field should not exceed the coercive threshold. Therefore, the simple model used to develop Equation 4.1 is necessarily incomplete. Fi-

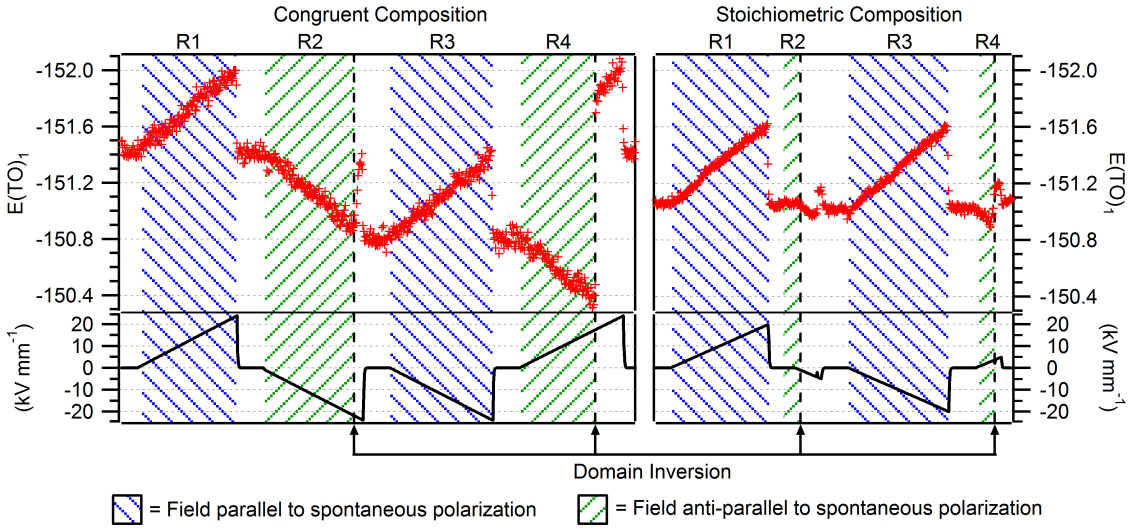

Figure 4.1: Frequency (in cm^{-1}) of the E(TO)$_1$ Raman mode and the applied external electric field during the entire sequence of experimental steps for both congruent and stoichiometric $LiNbO_3$. The vertical dashed lines indicate the points at which the crystal underwent domain inversion.

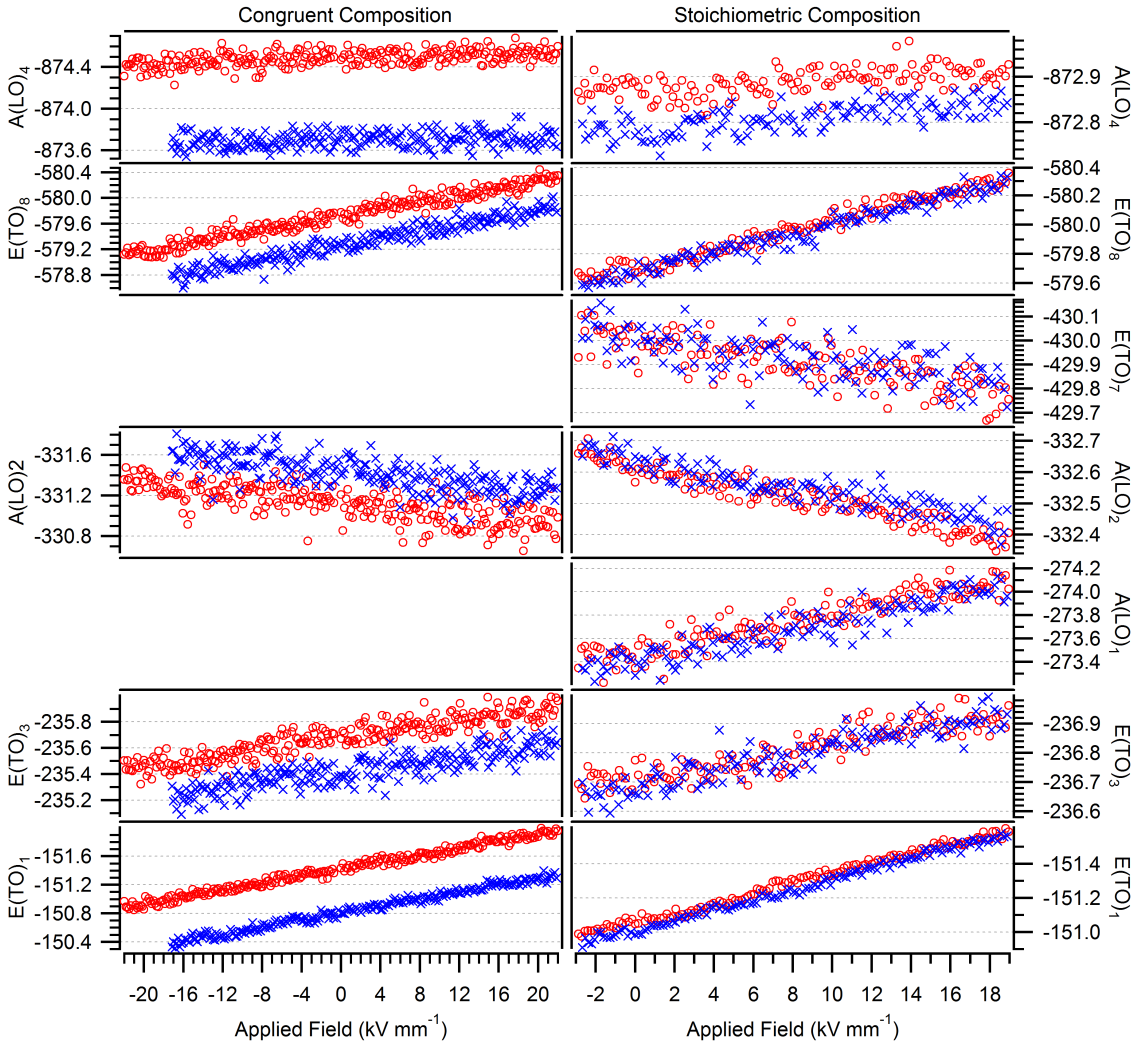

Figure 4.2: Frequency (in cm^{-1}) of the investigated Raman modes as a function of the applied external electric field in the as-grown (red $\circ$) and domain inverted (blue $\times$). The data corresponding to the as-grown state is taken from steps R1 and R2 in Figure 4.1, while the data corresponding to the domain inverted state is taken from steps R3 and R4. A positive electric field indicates that the applied voltage is parallel to the spontaneous polarization as in steps R1 and R3, and vice versa as in steps R2 and R4.

Table 4.2: Zero-field peak positions (α in cm^{-1}) and linear frequency response coefficients (β in $cm^{-1}/(kV/mm^{-1})$ obtained from fitting the Raman mode data of Figure 4.2 to the equation $y = \alpha + \beta E_{ext}$. The fitting errors for α and β are $\pm 0.005 cm^{-1}$ and $\pm 0.001 cm^{-1}/(kV/mm^{-1})$, respectively.

		Congruent		Stoichiometric	
Mode		α	β	α	β
	As-grown	−151.42	−0.024	−151.06	−0.028
$E(TO)_1$	Domain inverted	−150.81	−0.025	−151.01	−0.030
	As-grown	−235.68	−0.011	−236.71	−0.012
$E(TO)_3$	Domain inverted	−235.41	−0.010	−236.69	−0.013
	As-grown			−273.49	−0.033
$A(LO)_1$	Domain inverted			−273.41	−0.033
	As-grown	−331.12	0.010	−332.62	0.012
$A(LO)_2$	Domain inverted	−331.45	0.010	−332.64	0.011
	As-grown			−430.00	0.011
$E(TO)_7$	Domain inverted			−430.01	0.009
	As-grown	−579.72	−0.027	−579.70	−0.032
$E(TO)_8$	Domain inverted	−579.26	−0.028	−579.67	−0.033
	As-grown	−874.48	−0.003	−872.87	−0.002
$A(LO)_4$	Domain inverted	−873.70	−0.002	−872.78	−0.003

Table 4.3: Comparison of the total experimentally observed shifts of the Raman modes (in cm^{-1}) between the as-grown and domain inverted states to the value predicted by $(E_F - E_B) \times \beta_{mode}$.

	Congruent		Stoichiometric	
Mode	Calc.	Expt.	Calc.	Expt.
$E(TO)_1$	0.14	0.61	0.02	0.05
$E(TO)_3$	0.06	0.27	0.01	0.02
$A(LO)_1$	×	×	0.02	0.08
$A(LO)_2$	−0.06	−0.33	−0.01	−0.02
$E(TO)_7$	×	×	−0.01	−0.01
$E(TO)_8$	0.15	0.46	0.02	0.03
$A(LO)_4$	0.01	0.78	0.00	0.09

Table 4.4: Magnitude of the internal electric field (in kV/mm) along the ferroelectric axis required to produce the observed frequency shifts following domain inversion.

Mode	Congruent	Stoichiometric
$E(TO)_1$	24.8	1.8
$E(TO)_3$	25.8	1.6
$A(LO)_1$	×	2.4
$A(LO)_2$	33.0	1.8
$E(TO)_7$	×	1.0
$E(TO)_8$	16.6	1.0
$A(LO)_4$	352.2	32.0

nally, it must be concluded that the existing defect models produce a local field component which is not parallel to the ferroelectric axis and/or there are additional, undetermined defects which possess dipoles not parallel to the ferroelectric axis. Further details concerning this work may be found in Stone *et al.* [91].

4.2 Laser-induced space charge fields

In addition to an applied external electric field, the frequencies of the Raman modes were also found to shift merely due to exposure of the sample to the probe laser at low temperature. This effect was first observed by Sandmann within the erbium fluorescence spectrum of $LiNbO_3$ [6]. As the sample was continuously irradiated the peak positions of the erbium fluorescence emission were found to gradually shift until reaching a steady state. Illuminating the sample with different laser powers resulted in a shift of the initial peak position, followed by the same relative shift until steady state was reached. The initial frequency shift versus power behaved exponentially while the relative frequency shift versus time exhibited a stretched exponential profile. The initial frequency shift was reversed after illumination was terminated, while the gradual, time-dependent shift persisted even after the laser was turned off and until the sample was warmed. No differences in this behavior were observed whether the +c or -c surfaces of the crystal were illuminated. Finally, occasional "discharges" during continued illumination, in which the energy of the peak would quickly revert back toward its initial value before resuming its gradual shift away, were observed in the peak position, as shown in Figure 4.3.

As this illumination was found to reduce the coercive field required to induce domain inversion, the shifts of the Raman modes were determined to be the result of a "space charge" field established at the focus of the laser due to photoionization of defects. In this model electrons are photoexcited and move toward the +c surface, leaving behind positively

charged ions, as shown in Figure 4.4. This creates a localized dipole moment which, similar to the intrinsic defect dipole moments discussed in the previous section, can interact with the spontaneous polarization of the material.

While the details concerning the defects which are ionized and the nature of the instantaneous and slower charging effects are well described by Sandmann [6], the cause of the occasional discharging is yet unresolved. Indeed, subsequent to Sandmann's work, further experiments yielded many inconsistencies. For example, Figures 4.5 to 4.8 present erbium fluorescence data from experiments performed on the same two Er:CLN and Fe:Er:CLN samples on two different days. Ostensibly, the experimental conditions were identical. Nevertheless, both samples reverse their behavior. Figure 4.5 shows that the Er:CLN sample exhibits two discharges during the first experiment and none during the second. Additionally, the charging is quick during the first experiment and slow during the second. Conversely, Figure 4.7 shows that the Fe:Er:CLN sample exhibits no discharges during the first experiment while experiencing 10 during the second. Finally, Figures 4.6 and 4.8 reveal that additional fluorescence peaks which appeared in both samples during illumination in the first experiment never appeared during the second experiment.

That these new peaks appeared almost instantly upon illumination and disappeared once the illumination was removed, in addition to not being influenced by the buildup and discharging of the space charge field, suggested that they arose due to laser-modification of Fe-related defects local to the erbium ions. Nevertheless, as these peaks are at other times absent, this theory must be questioned or modified.

In order to determine the apparently hidden parameter responsible for these inconsistencies, further experiments were performed using Raman spectroscopy and the setup described in Section 3.1.2. The position of the $E(TO)_1$ Raman mode was tracked as the sample was illuminated for an extended period of time. A variety of alterations to the experimental conditions were tested. These included mounting the sample to the copper cold

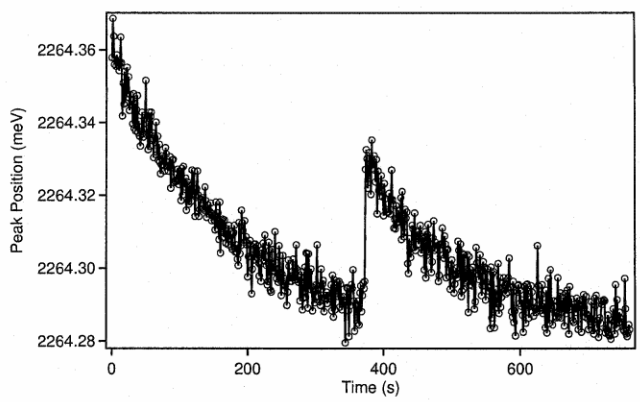

Figure 4.3: Example of the influence of a discharge during continuous illumination on the energy of an erbium fluorescence peak in Er:CLN. Reproduced from Sandmann [6].

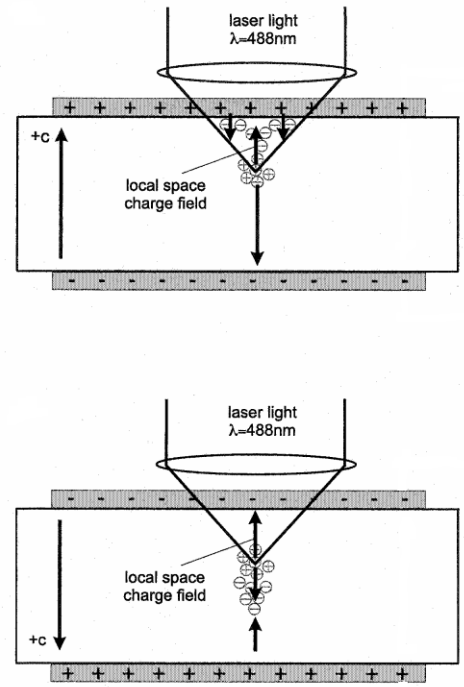

Figure 4.4: Illustration of the electric field due to a laser-induced space charge field in a ferroelectric crystal caused by photoionization of defects. Reproduced from Sandmann [6].

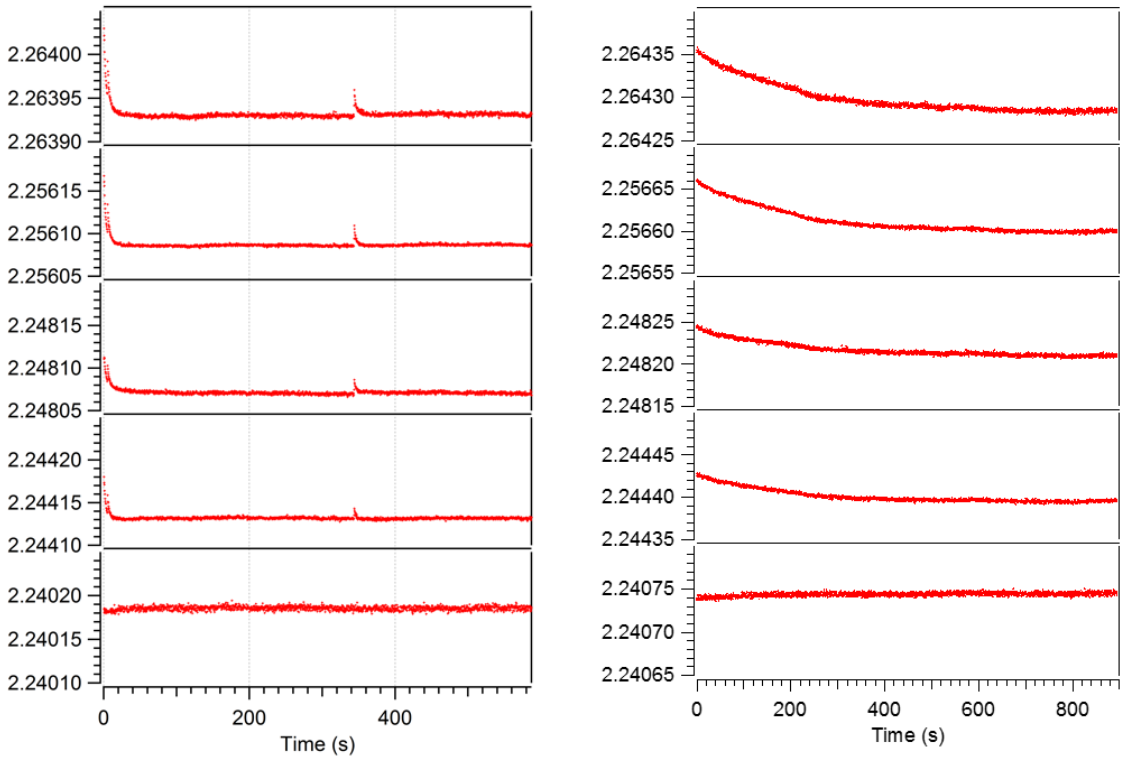

Figure 4.5: Response of multiple erbium fluorescence peaks due to the buildup of a space charge field in Er:CLN. Left: First experiment, discharges were observed. Right: Second experiment, no discharges were observed.

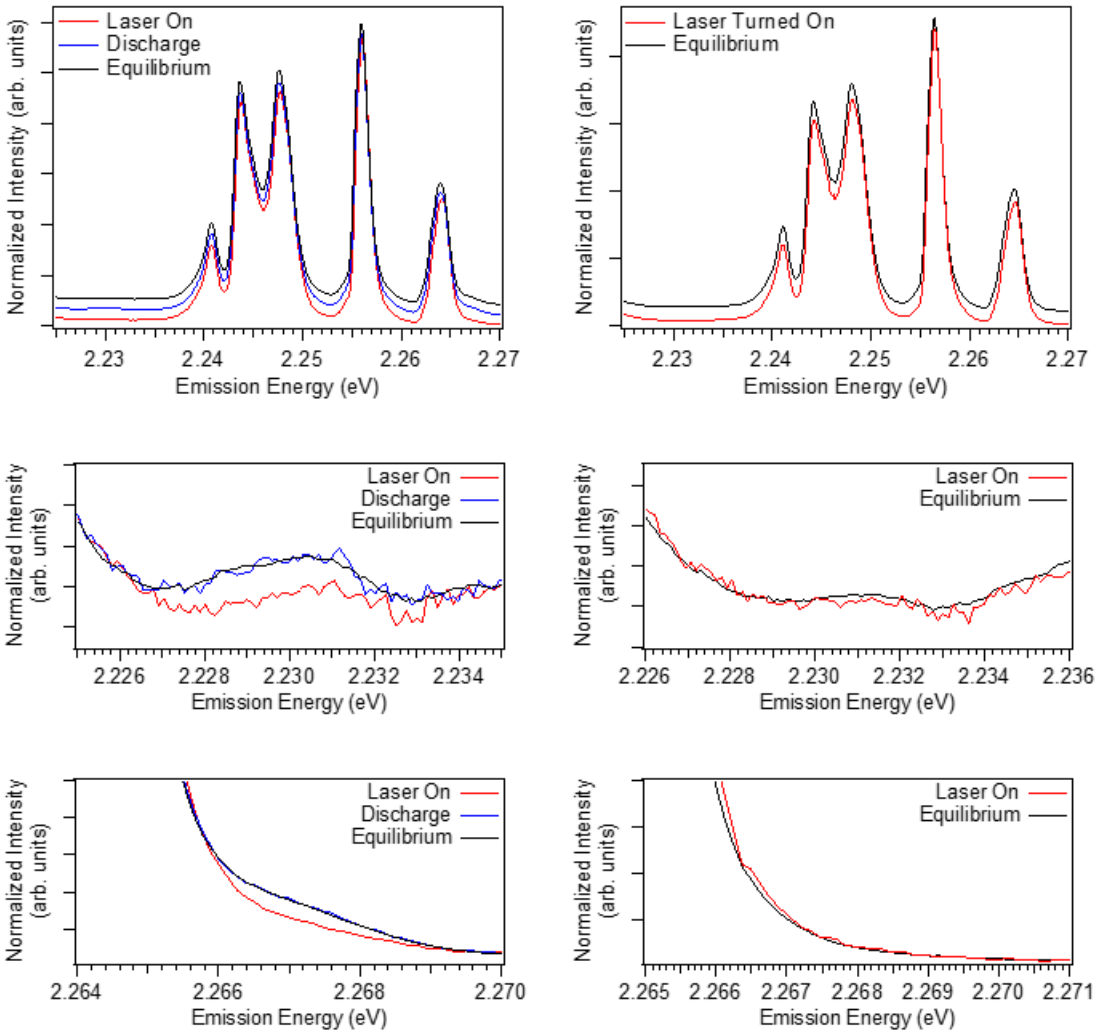

Figure 4.6: Left: First experiment. Right: Second experiment. Top Row: Comparison of individual spectra at different times. Middle and Bottom Rows: Closeup of spectral regions where additional peaks which were not sensitive to the space charge field were observed.

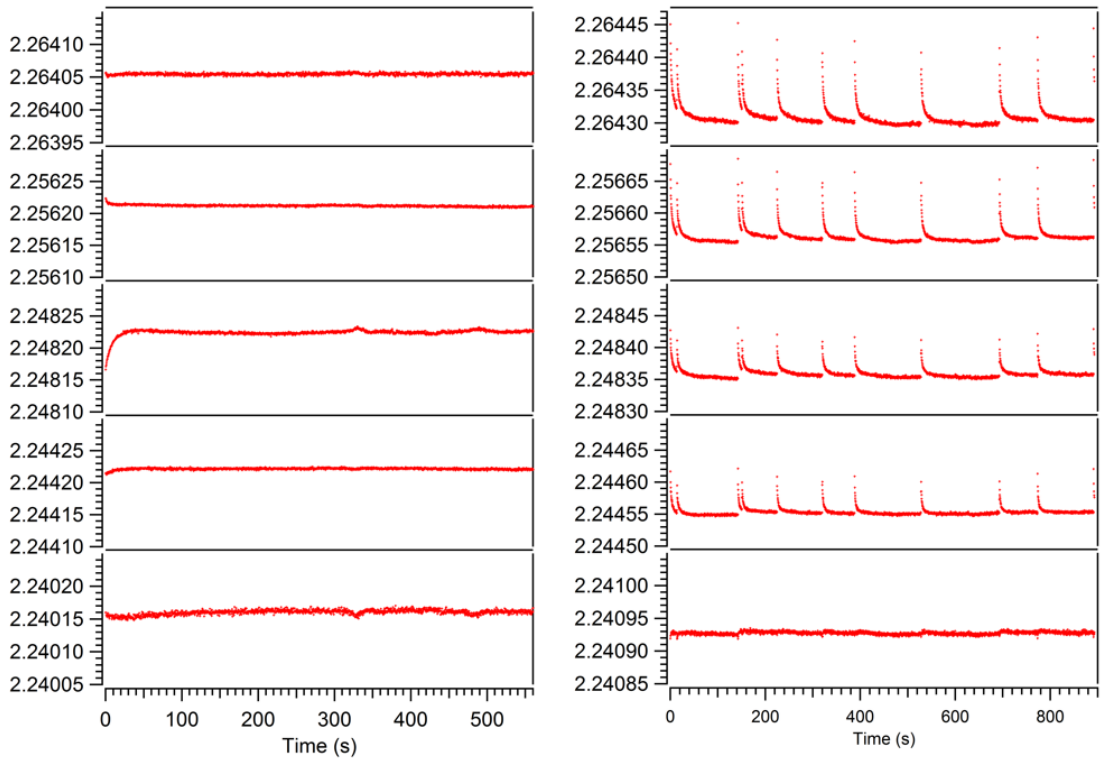

Figure 4.7: Response of multiple erbium fluorescence peaks due to the buildup of a space charge field in Fe:Er:CLN. Left: First experiment, discharges were observed. Right: Second experiment, no discharges observed.

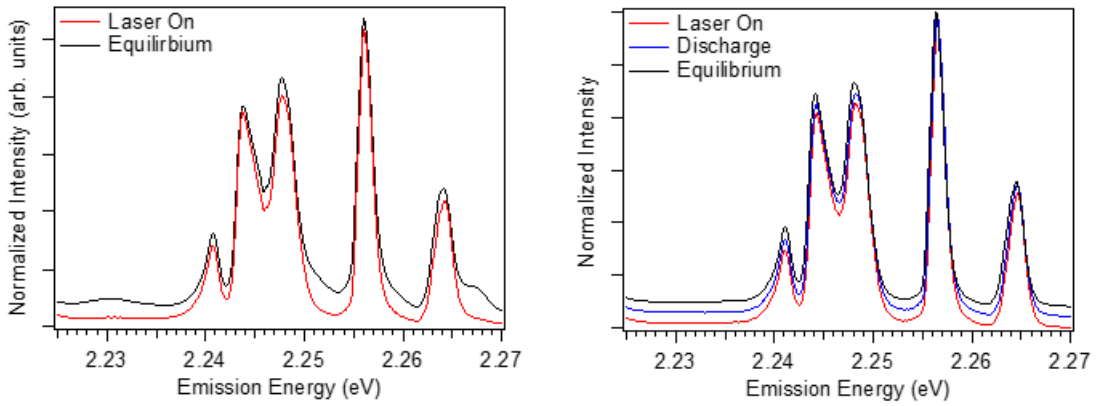

Figure 4.8: Comparison of individual spectra of Fe:Er:CLN at different times during the experiments.

finger using conductive copper tape or silver paint, illuminating both the +c and -c surfaces, varying the power of the laser, and focusing at different depths with respect to the surface.

These experiments showed that there is no dependence of the discharging behavior on the mounting medium, as discharges were observed using both copper tape and silver paint. Additionally, there seemed to be a sample-dependent laser power threshold below which no discharges could occur. Beyond this, the data were frustratingly inconclusive. The most likely conclusion based on the available data, though additional data is required in order to assign it, is that not only do different samples have different thresholds for discharging, but within a sample, the +c and -c have different thresholds as well. Finally, focusing deeper into the sample increases the threshold in all cases. Figure 4.9 presents data in partial support of the first and third conclusion and shows the behavior of the $E(TO)_1$ Raman mode frequency in Fe:Er:CLN and CLN samples during illumination under different laser power and focal depth conditions. Note that in this figure the left and right sides correspond to experiments which were performed at the same time and using identical sets of conditions. The second conclusion is unsupported at this time, but could potentially explain the original discrepancy observed in Figures 4.5 and 4.7, as the $t = 0$ peak energies are different, suggesting that opposite surfaces were illuminated.

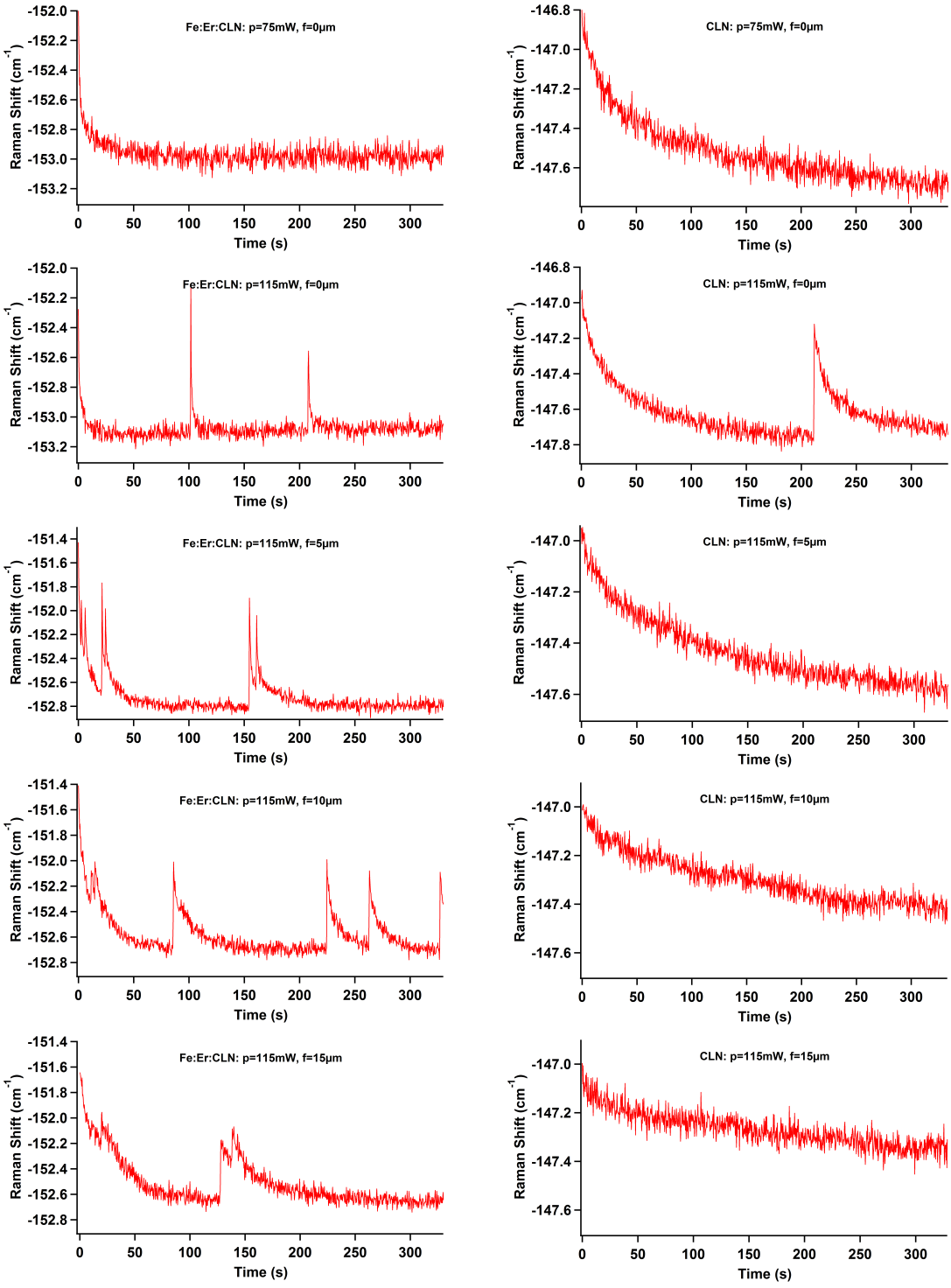

Figure 4.9: Behavior of the $E(TO)_1$ Raman mode during continuous illumination of Fe:Er:CLN and CLN under various experimental conditions.

Chapter 5

Fluorescence Properties of Er:$LaBGeO_5$ Under Resonant Excitation

While the optical properties of crystalline Nd^{3+}- and Pr^{3+}-doped $LaBGeO_5$ have been extensively studied, no such work exists for Er^{3+}. Indeed, as mentioned in Section 2.2.3, only Malashkevich *et al.* have worked with Er:$LaBGeO_5$, and even then the materials were only glasses co-doped with Yb^{3+} [35]. Nevertheless, erbium is an important and interesting dopant ion due to its potential applications arising from its emission around $1.54\mu m$, which is conveniently within the transmission window of silica fibers. Additionally, erbium also makes an excellent probe of the local structure, especially in a material such as $LaBGeO_5$, in which it is expected to substitute easily for lanthanum.

In order for eventual applications to be realized in laser-induced crystals-in-glass doped with erbium, the properties of the erbium ions in both the glass and crystal phases must be understood. This chapter presents a quantitative analysis of the fluorescence properties of Er:$LaBGeO_5$, as well as comparisons with conventional glass-ceramics and laser-induced crystals of varying erbium concentrations. Finally, the influence of different laser irradiation parameters is discussed.

5.1 Baseline study of $Er_{.01}La_{.99}BGeO_5$ glass-ceramic

As a first step toward understanding the properties of the erbium ion in $LaBGeO_5$, CEES maps were collected from both $Er_{.01}La_{.99}BGeO_5$ glass and glass-ceramics prepared according to the procedures described in Section 3.4.1. Figure 5.1 presents the CEES map of the ${}^4I_{\frac{15}{2}} \rightarrow {}^4 I_{\frac{11}{2}}$ and ${}^4I_{\frac{13}{2}} \rightarrow {}^4 I_{\frac{15}{2}}$ transitions in excitation and emission, respectively, for the glass. As expected, the amorphous structure of a glass results in a CEES map which shows only a broad excitation and emission peak.

In contrast to the glass, the crystal is anisotropic and possesses long range fields which break the degeneracy of the Stark levels within the spin-orbit multiplets. For $LaBGeO_5$, the local symmetry of every lattice site, including the lanthanum site which erbium is expected to occupy, is C_1. Because C_1 is a very low symmetry point group, all of the degeneracy is lifted and each multiplet splits into the full $J + \frac{1}{2}$ levels. This should yield 8, 7, 6, and 5 Stark sublevels for the four ${}^4I$ terms, respectively. Figure 5.2 shows a CEES map of the ${}^4I_{\frac{15}{2}} \rightarrow {}^4 I_{\frac{11}{2}}$ and ${}^4I_{\frac{13}{2}} \rightarrow {}^4 I_{\frac{15}{2}}$ transitions in excitation and emission, respectively, while Figure 5.4 maps the ${}^4I_{\frac{15}{2}} \rightarrow {}^4 I_{\frac{9}{2}}$ and ${}^4I_{\frac{11}{2}} \rightarrow {}^4 I_{\frac{15}{2}}$ transitions in excitation and emission, respectively, for the glass-ceramic.

Importantly, the CEES maps for the glass-ceramic show that the material is indeed anisotropic and crystalline due to the splitting of the original broad excitation and emission peak into many discrete, sharp peaks. The emission exhibits predominantly one excitation profile and one emission profile, each of which is repeated at the different emission and excitation energies, respectively. However, upon very close inspection, at least one other set of unique excitation and emission profiles is observed. This indicates that the erbium ions occupy multiple different incorporation environments (sites). Emission profiles for these two sites are shown in Figure 5.7. Due to the dominant nature of the one site, it is assumed that this site consists of an unperturbed erbium ion at the nominal lanthanum site,

and that most of the erbium ions experience this environment. The nature of the second site is unknown, but could potentially be related to an erbium ion at a boron vacancy, or some other defect. Because this secondary site is very weak, the focus of the following level assignment will be on the dominant, primary site.

In order to appreciate the process of assigning the observed fluorescence to transitions between particular sublevels of each multiplet, consider first a simple hypothetical system with only three spin-orbit multiplets, each of which can split into only two Stark levels when a crystal field is present. In this case the excitation is from the lowest energy multiplet to the highest energy multiplet. The system then non-radiatively decays into the middle multiplet, from which emission back to the lowest energy multiplet is observed. Figure 5.6 presents an energy level diagram and mock CEES map for this hypothetical case. The CEES map is color-coded to the energy level diagram such that each peak may be correlated with a specific excitation/emission route. When the host material is in the glassy phase, no Stark splitting is observed and the CEES map consists of only the large red/orange peak. In the presence of a crystal field, the spin-orbit multiplets split into a total of 6 Stark levels. Taking into consideration the prescribed non-radiative decay, and assuming the symmetry is low enough such that no selection rules come into play, this allows 16 possible transitions. However, in order to observe all 16 transitions, enough thermal energy must be present to populate the higher higher-energy sublevels of the bottom and middle multiplets. In general, the experimental conditions under which the real data presented later in this chapter were collected were such that sufficient thermal energy to populate the first few sublevels of each multiplet was present.

Figure 5.6 shows 16 peaks whose positions correspond to the energies of the transitions for processes involving only photons. Although they are not shown, it is possible for this set of 16 peaks to be identically repeated at slightly greater excitation energies and slightly lower emission energies due to electron-phonon coupling, which is described elsewhere

[92, 93]. However, due to the well-shielded nature of the electrons of erbium, the electron-phonon coupling in erbium-doped $LaBGeO_5$ is extremely weak and therefore negligible.

For the hypothetical case of Figure 5.6, assigning the levels is straightforward since each excitation and emission "spectrum" has only four peaks and each multiplet has only two levels. In excitation, there are two different repeated energy difference values within the set of four peaks. One of these values corresponds to the spacing between the Stark sublevels of the lowest-energy multiplet (denoted as spacing A), while the other corresponds to the spacing between the sublevels of the highest-energy multiplet (denoted as spacing C). Because spacing C has nothing to do with the emission due to the non-radiative decay, whichever quantitative spacing is also found in emission can be assigned as spacing A. Using this information, the higher-energy pair of peaks in excitation with spacing C can be assigned to transitions from the lowest Stark sublevel of the lowest-energy multiplet into each level of the highest-energy multiplet. Similarly, the other set of peaks with spacing C in excitation corresponds to transitions from the thermally excited sublevel of the lowest-energy multiplet. Finally, the same logic can be applied to the emission to assign the levels of the middle-energy multiplet. In emission, the second repeated energy difference (denoted as spacing B) corresponds to the spacing between the sublevels of the middle energy multiplet. Thus, the pair of peaks with spacing B, beginning with the highest-energy emission peak, can be assigned to transitions from the thermally excited sublevel of the middle-energy multiplet to the two levels of the lowest-energy multiplet. And similarly, the other pair of emission peaks with spacing B, which is shifted from the first pair by spacing A, can be assigned to transitions from the lower-energy sublevel of the middle-energy multiplet to the two levels of the lowest-energy multiplet.

Assignment of the energy levels of erbium in $LaBGeO_5$ is significantly more complicated than this hypothetical case due to the fact that there are many more sublevels in each multiplet. Thus the process is necessarily more complex in the beginning as the first pairs

are chosen and confirmed to be self-consistent. First, an excitation spectrum is extracted from the CEES map. The brightest peak is assumed to represent some highly probable transition from a low-sublevel in the ground multiplet to a low-sublevel in the excited multiplet. On that assumption, the same peak of a corresponding emission spectrum from a CEES map collected at a higher temperature is scaled to equal intensity. Since the temperature has changed, the relative intensities of most of the other peaks will be different compared to their counterparts in the low temperature CEES. However, since at low temperature both the lowest sublevel and the first thermally excited level of the ground multiplet are occupied, the intensity of the two peaks corresponding to the transition from these sublevels should change proportionally to each other. Therefore, there should be another peak at either slightly higher or lower energy than the first whose intensity after scaling is also fairly equal to that of its low-temperature counterpart. For simplicity, these two peaks are assumed to represent transitions from the lowest two sublevels of the ground multiplet to the lowest sublevel of the excited multiplet. For this to be correct, the energy difference between these two excitation peaks must be repeated between other pairs in the excitation spectrum at higher energies, as well as in the emission spectrum. If this is found to be true, and no other repeated pairs have a smaller energy difference, then the initial assignment is correct.

Thus, by using the excitation spectrum, the sublevels of the excited multiplet can be assigned energy values by noting the higher-energy value of each repeated pair. Once this has been done, the sublevels of the ground multiplet can be assigned by looking for repeated sets of peaks spaced at the distances prescribed by the assignment of the excited multiplet, and noting the separation between each of the sets. Similarly, once the levels of the ground multiplet are known, repeated sets of peaks spaced accordingly within the emission spectrum will represent respective transitions from each sublevel of the corresponding intermediate excited multiplet.

Figures 5.3 and 5.5 show the results of the level assignment analysis overlayed on Figures 5.2 and 5.4, respectively. In each figure there are multiple sets of differently-colored horizontal and vertical lines. Each set of horizontal lines of the same color indicate transitions from a single Stark level of the $^4I_{15/2}$ multiplet to all of the observed sublevels of the $^4I_{9/2}$ (Figure 5.5) and $^4I_{13/2}$ (Figure 5.3) multiplets. Similarly, each set of vertical lines of the same color indicate transitions from all of the observed sublevels of the $^4I_{13/2}$ (Figure 5.5) and $^4I_{11/2}$ (Figure 5.3) multiplets to a single sublevel of the $^4I_{15/2}$ multiplet. Table 5.1 lists the possible Stark sublevels of the ^4I multiplets and their respective energies. Due to the symmetry of the site and experimental geometry, transitions between all possible states are allowed. However, due to the low probability of some transitions, as well as insufficient thermal energy, not all transitions were observed.

5.2 $LaBGeO_5$ glass-ceramics with different Er concentrations

As a next step, CEES maps were collected for $LaBGeO_5$ glass-ceramics with erbium concentrations corresponding to 4%, 10%, and 20% molar replacement of lanthanum and are shown alongside the data from the 1% sample in Figure 5.8 for comparison. From this data it is apparent that as the erbium concentration is increased, the energy level structure is maintained, and erbium continues to incorporate at predominantly one site.

However, while the overall intensity of the fluorescence emission somewhat follows the composition in erbium doped $LaBGeO_5$ glasses for which data is available, the intensity from the glass-ceramics behaves in the opposite manner, as shown in Figure 5.9. It should be noted that although the trend in the glasses is as expected, the ratio of intensities is slightly less than 1:5:20 for the 0.2%, 1%, and 4% samples. The glass-ceramics show diminishing fluorescence intensity with increased erbium composition up to 10%. The

Multiplet	m_J	Energy (eV)
$^4I_{9/2}$	$1/2$	-
	$3/2$	1.5646
	$5/2$	1.5545
	$7/2$	1.5447
	$9/2$	1.5365
$^4I_{11/2}$	$1/2$	1.2934
	$3/2$	1.2819
	$5/2$	1.2760
	$7/2$	1.2723
	$9/2$	1.2687
	$11/2$	1.2661
$^4I_{13/2}$	$1/2$	-
	$3/2$	-
	$5/2$	-
	$7/2$	-
	$9/2$	0.81659
	$11/2$	0.81272
	$13/2$	0.81081
$^4I_{15/2}$	$1/2$	-
	$3/2$	-
	$5/2$	-
	$7/2$	0.02001
	$9/2$	0.01373
	$11/2$	0.00804
	$13/2$	0.00265
	$15/2$	0

Table 5.1: Assigned energy levels for erbium in $Er_{.01}La_{.99}BGeO_5$. Levels without energy values are predicted but were not observed.

20% sample yields slightly more intensity that the 10% sample.

Besides the decrease in the peak intensity for each transition, the most obvious effect of the increased erbium concentration is the gradual broadening of the peaks. As described in Section 3.4.1, all of the samples were processed at the same temperature. Likely, increasing the erbium concentration increases the crystal nucleation and growth temperatures, and thus, given the growth conditions, the crystals with higher concentrations of erbium may be incompletely crystallized. However, though this may seem to be a reasonable conclusion, it is not supported by the Raman data presented in Chapter 6, Figure 6.2.

The more likely explanation for the broadening is that as the erbium concentration increases, it becomes more and more likely that each erbium ion has another erbium ion nearby. In this case the local symmetry of each erbium incorporation site remains the same, but the number of possible perturbations increases substantially due to interactions between different numbers of erbium ions. This results in the broadening of the energy levels involved in both excitation and emission.

The broadening of the absorption should reduce the amount of light absorbed. However, as the glass-ceramics are polycrystalline, they contain many grain boundaries which can serve to scatter the excitation light back and forth such that it passes through the collection volume many times. During these trips, most of the light will eventually be absorbed, and therefore the emission should be the same as, or greater than, that of the glass, which is partially transparent. Nevertheless the overall emission is reduced due to the relatively long lifetime of the excited state making energy transfer to non-radiative decay pathways, which may be more abundant in higher-doped crystals, more likely. Also, as mentioned in Chapter 2, the energy levels involved with the erbium emission at $1.54\mu m$ are susceptible to non-radiative decay via excitation energy exchange into antisymmetric stretching vibrations of boron tetrahedra and/or vibrations of impurity OH-groups. In samples with higher erbium concentrations, it becomes easier for one erbium ion to transfer its energy

to a different erbium ion and so on. As the number of these transfers increase, the total time spent in the excited state also increases, and the likelihood of the energy being lost to non-radiative decay increases, resulting in less radiative emission. This effectively removes the proportionality between the fluorescence intensity and the erbium concentration. It should be noted that the overall effect is different in the glass-ceramics case compared to the glass. In the glass the broadening is governed by the disorder present. The effect of erbium-erbium interactions is much weaker than that of the disorder, which should be roughly the same in all compositions. Additionally, the glass lacks grain boundaries which serve as scattering centers. So while the absorption and emission in glass also involve only a subset of the erbium ions, the number of ions in each subset remains proportional to the total number of ions present in a given concentration.

An interesting related issue is that of the fluorescence line narrowing, which is described toward the end of Section 3.3, observed in these crystals. Figure 5.10 shows a selected portion of a CEES map containing a fluorescence line narrowed peak, and individual spectra taken at different excitation photon energies for glass-ceramic samples with different erbium concentrations. As the concentration of erbium increases, the emission broadens and the amount of FLN seemingly decreases. This effect could arise as the FLN is overwhelmed by the broadening due to the increased erbium, or potentially be related to a lessening of strain as the structure approaches that of $ErBGeO_5$.

5.3 Comparison of laser-induced crystals

CEES maps were collected from laser-induced crystalline lines in glass using the scanning geometry shown in Figure 3.3. Initially, the CEES microscope used a multimode collection fiber and was therefore not confocal. However, when this setup was used for measuring the laser-induced crystals, the collection area included too much of the surrounding glass and

the spectra were dominated by emission from the glass. In an attempt to improve the spectra, a single-mode fiber was used to collect the emission and make the microscope confocal. While this helped somewhat, and the spectra became easily identifiable as that of a crystal, a small contribution from the surrounding glass remained. Therefore, two things should be noted. First, the CEES maps for the glass-ceramics and laser-induced crystals cannot be directly compared with respect to intensity, as the collection volumes were significantly different. Second, in order to visually enhance the CEES maps from the laser-induced crystals and draw attention to their properties, a small fraction of the CEES map of the corresponding glass was subtracted.

Figure 5.11 shows a CEES map of a laser-induced crystal in $Er_{.01}La_{.99}BGeO_5$ glass. The particular crystal to which this map corresponds is er1-s2l1, and its growth parameters are listed in Table A.2. Despite having less intensity and showing significant broadening, the map is easily comparable with that of the glass-ceramic in Figure 5.2. Importantly, the extreme conditions at the laser focus in which the crystal must grow do not appear to alter the ratio of the primary and secondary erbium incorporation sites, or produce additional sites. Figure 5.13 compares emission and excitation spectra extracted from the CEES maps in Figures 5.2 and 5.11. While these spectra certainly reinforce the conclusion that the erbium incorporation is the same in both the glass-ceramics and laser-induced crystals, they are difficult to interpret with respect to the source of the exhibited broadening. Specifically, as previously mentioned, the collection volume may contain some of the surrounding glass, and the spectra will therefore include its contribution. Alternatively, the broadening could instead be an indication that the glass has not fully crystallized, resulting a great number of perturbations to the erbium site.

Finally, Figure 5.14 shows excitation spectra extracted from CEES maps collected from laser-induced crystals grown in $Er_{.01}La_{.99}BGeO_5$ glass under various conditions. All of the crystals exhibit the same characteristic spectrum, indicating that the growth conditions

do not significantly influence the erbium incorporation site. However, it is interesting to note that depending on the growth conditions, the spectra exhibit different ratios of certain transitions, particularly with respect to the ${}^4I_{15/2}, m_J = {}^{15}/_2 \rightarrow {}^4 I_{11/2}, m_J = {}^1/_2$ transition at $1.2934eV$. Consideration of which transitions, according to the level assignment presented earlier in this chapter, are stronger or weaker, leads to the conclusion that the more ideal the laser irradiation conditions (i.e. more homogeneous temperature profile due to a shallower focal depth and aberration correction), the lower the temperature of the crystal during the CEES measurement. Given that each CEES map was collected under identical conditions, the fact that the crystals themselves are at different temperatures implies that the growth conditions affect the structure in such a way as to influence the thermal conductivity of the crystal. Thus, a better quality crystal, produced through irradiation conditions which are more ideal to crystal growth, will have a better thermal conductivity and thereby better conduct heat caused by the probe laser away from the collection volume.

5.3.1 Anomalous behavior of $\mathbf{Er_{.002}La_{.998}BGeO_5}$

Much of the motivation for this work originated from studying laser-induced crystal lines in $Er_{.002}La_{.998}BGeO_5$ glass which were grown by Adam Stone. These crystals were written using similar laser powers and focal depths as those in the newer, more heavily doped glasses. The write speed was $30\mu m/s$ and the focal profile was not aberration-corrected. However, in attempting to compare the fluorescence properties of the two sets of samples, it became apparent that the crystals prepared by A. Stone present anomalous behavior.

CEES maps were collected from these crystals, as well as a furnace crystallized glass-ceramic made from the same glass, and are shown in the bottom and top of Figure 5.15, respectively. It should be noted that the glass-ceramic of this composition was created from a pre-existing glass using slightly different conditions than those described in Section 3.4.1, instead being held at 670° and 850° for five hours each. This likely means that

this glass-ceramic has more crystal grains, and therefore more strain. Nevertheless, at first glance the CEES map of the glass-ceramic is overall almost identical in character to those corresponding to greater erbium concentrations, albeit with greater FLN. However, the ratio of the primary site to the secondary site is diminished compared to the other compositions, which suggests that the relative number of erbium ions occupying this site is greater in this composition than in other compositions. Emission spectra from each site are shown in Figure 5.16.

In comparison to the all of the other CEES maps from either glass-ceramics or laser-induced crystals, the CEES map of the laser-induced crystal is strikingly complicated. Multiple erbium incorporation sites are present, and although some broad similarities with the glass-ceramic exist, closer inspection of the individual spectra reveals that even the primary site is strongly modified. Figure 5.17 shows excitation spectra of the laser-induced crystal at two different emission energies, as well as the corresponding excitation spectra of the 0.2% glass-ceramics for comparison. Neither spectrum of the laser-induced crystal matches perfectly to its glass-ceramic counterpart, and interestingly, whereas the secondary site in the glass-ceramic is weak compared to the primary site, both sites yield approximately the same emission in the laser-induced crystal. This anomalous behavior is discussed further in Chapter 6.

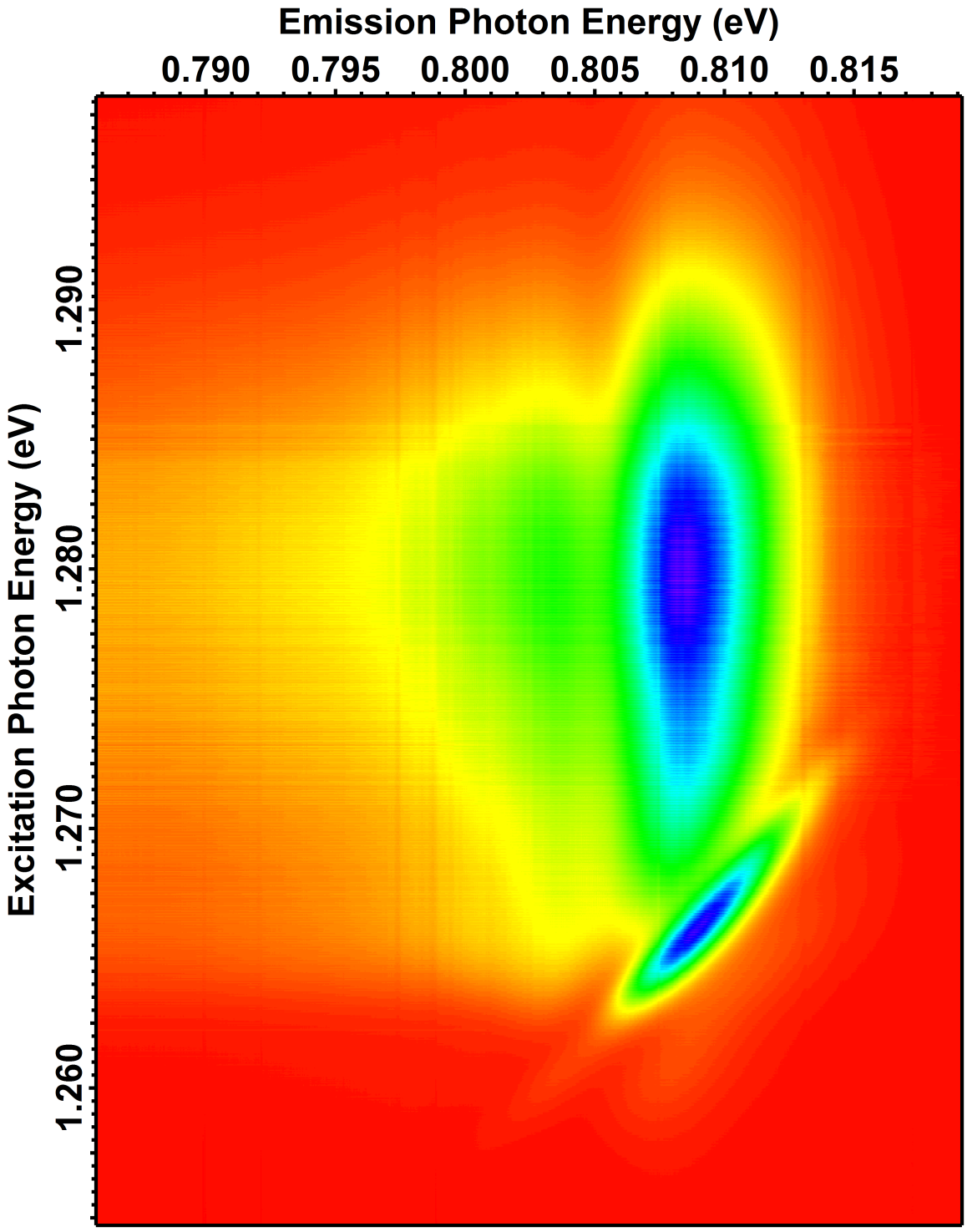

Figure 5.1: CEES map of 980nm excitation and 1550nm emission in $Er_{.01}La_{.99}BGeO_5$ glass.

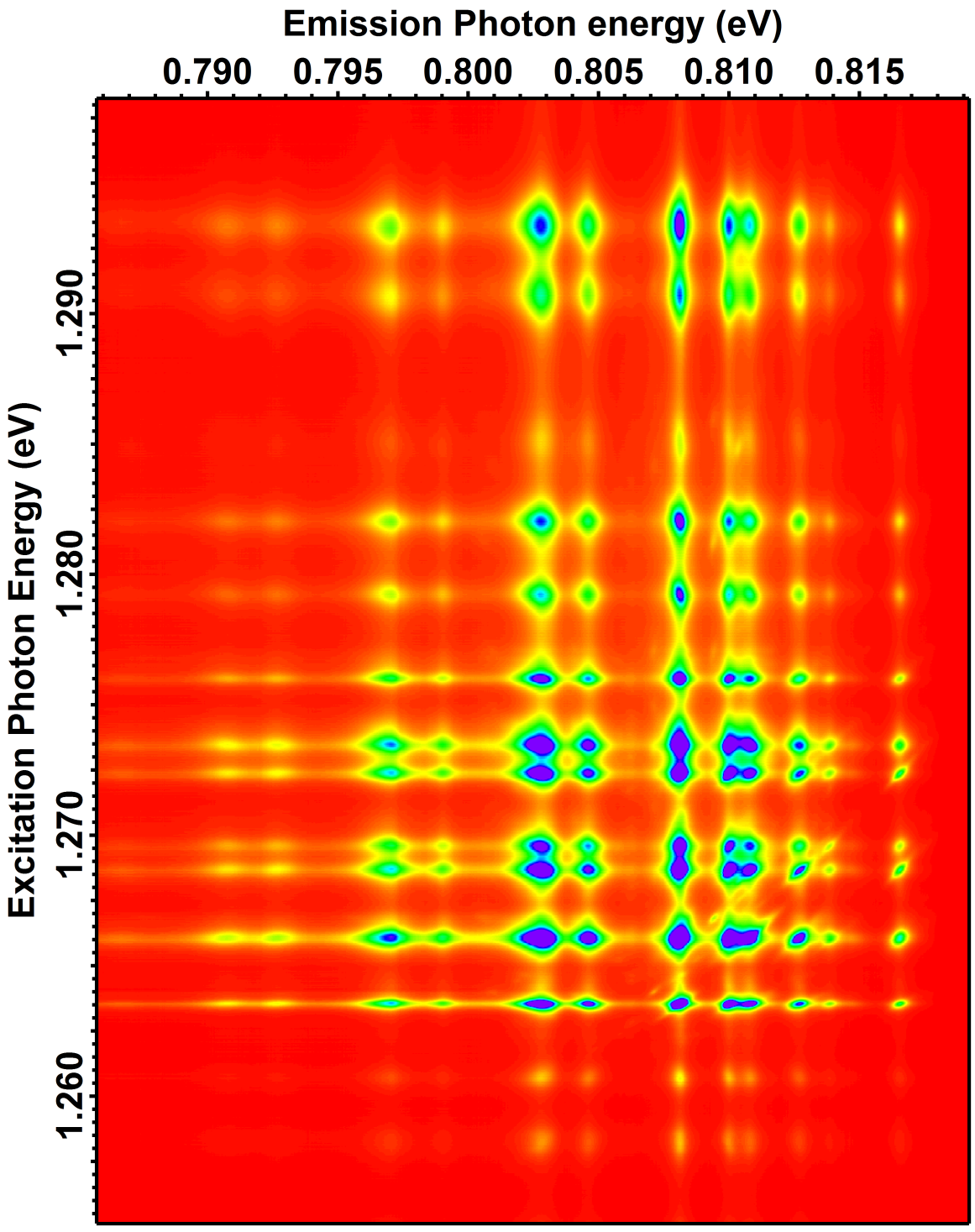

Figure 5.2: CEES map of 980nm excitation and 1550nm emission in the $Er_{.01}La_{.99}BGeO_5$ polycrystalline glass-ceramic.

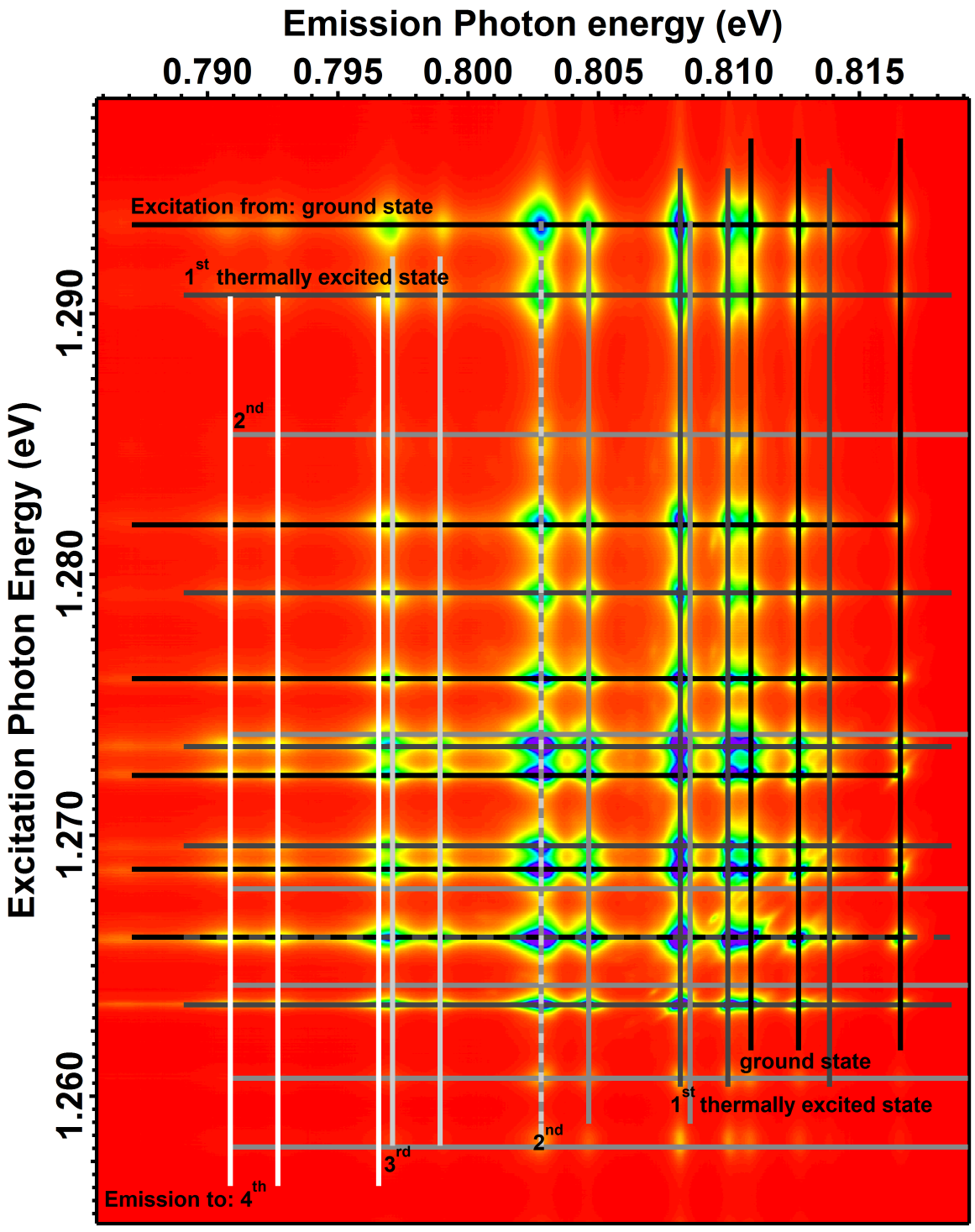

Figure 5.3: Overlay of Figure 5.2 with the level assignment grid.

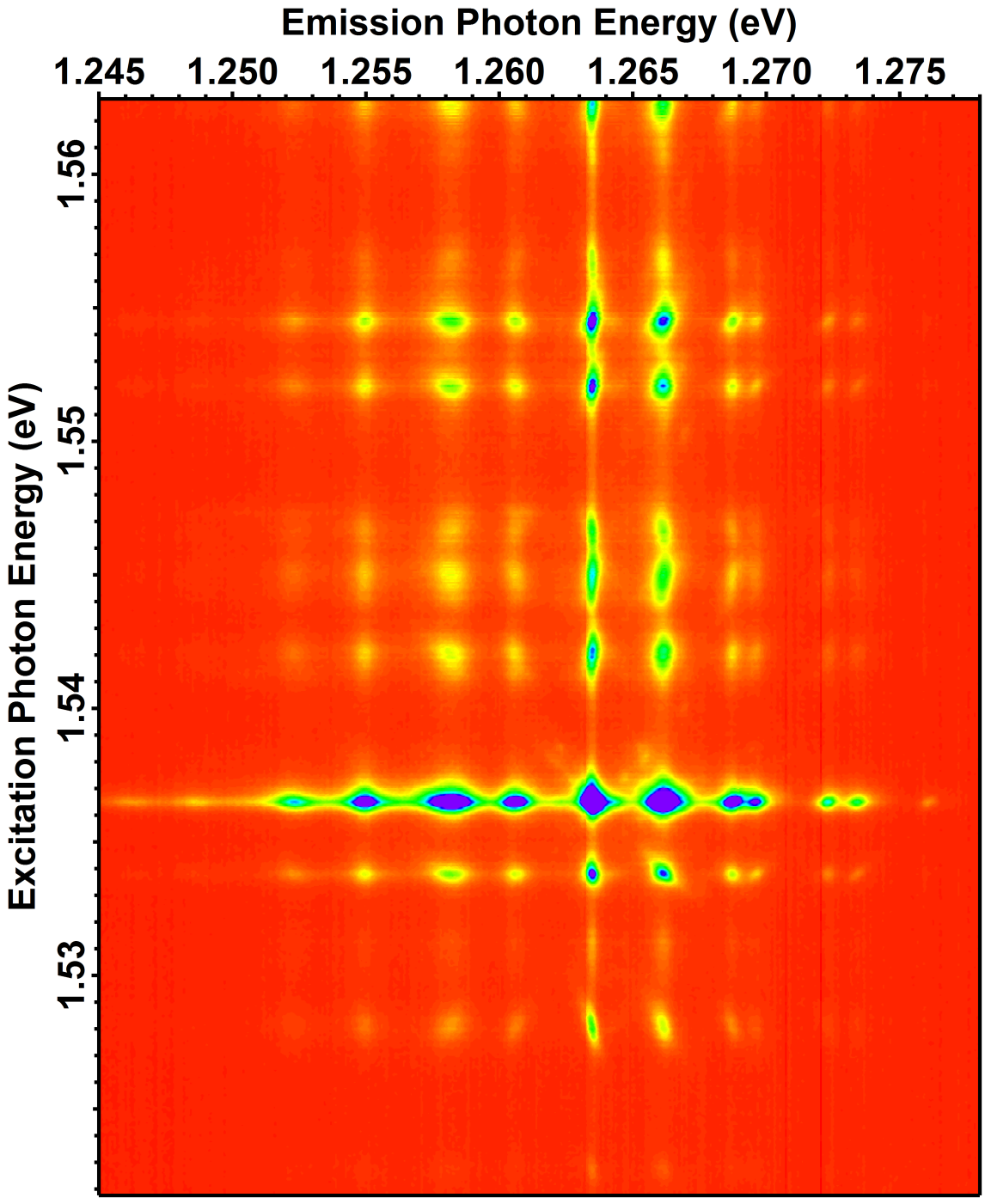

Figure 5.4: CEES map of $800nm$ excitation and $980nm$ emission in the $Er_{.01}La_{.99}BGeO_5$ polycrystalline glass-ceramic.

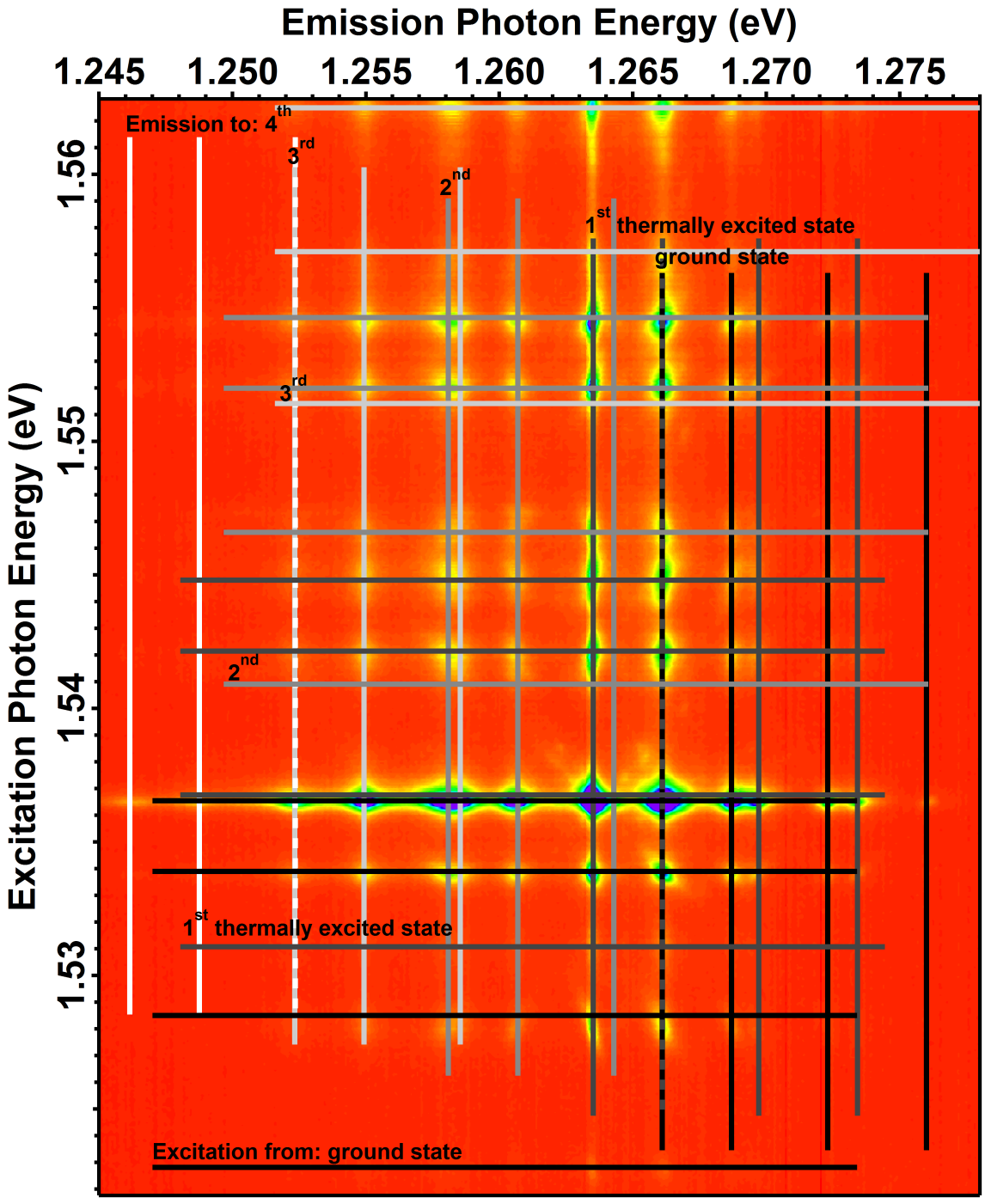

Figure 5.5: Overlay of Figure 5.4 with the level assignment grid.

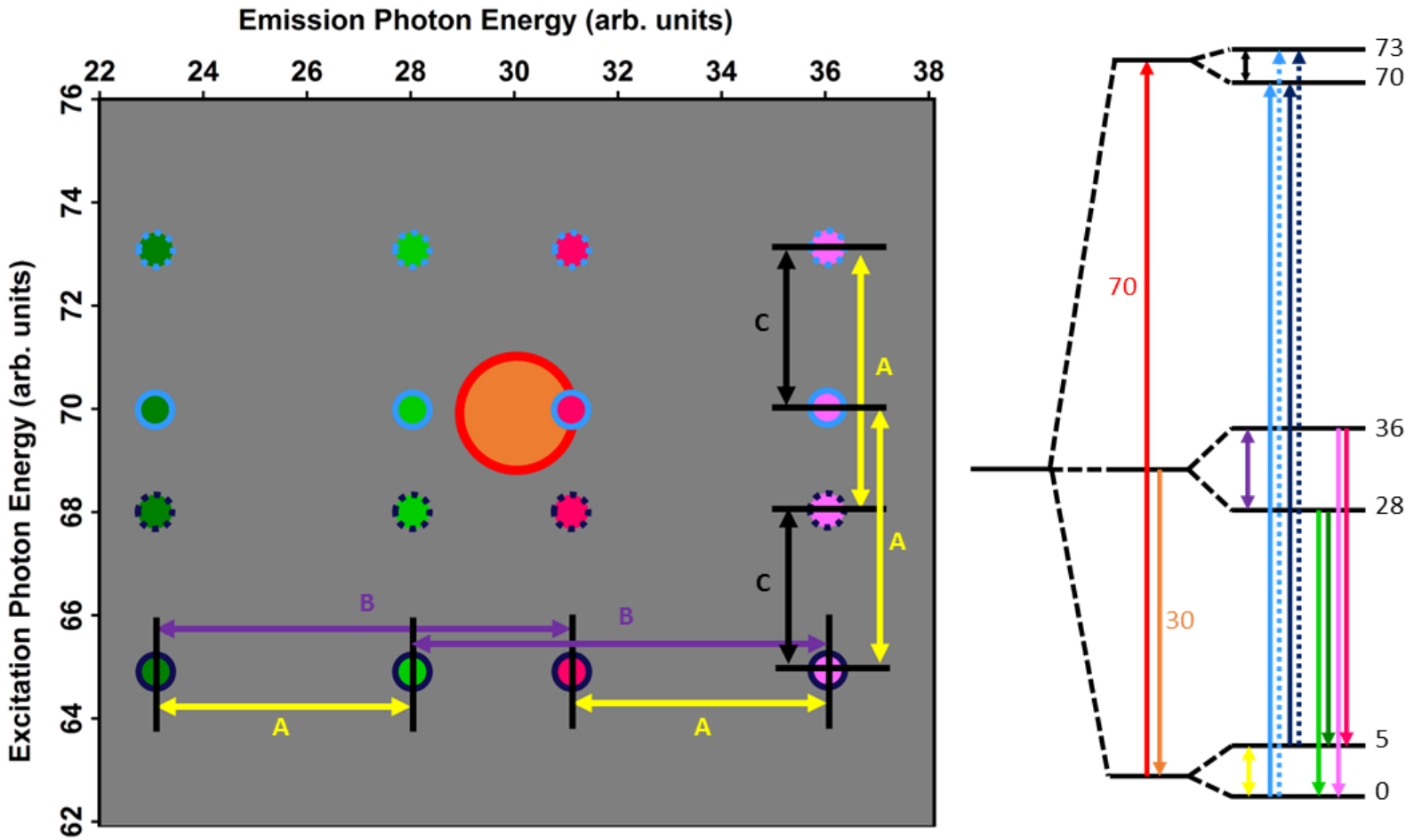

Figure 5.6: A CEES map and energy level diagram for a hypothetical system which illustrates the process of assigning the observed fluorescence peaks to the respective transitions from which they originate.

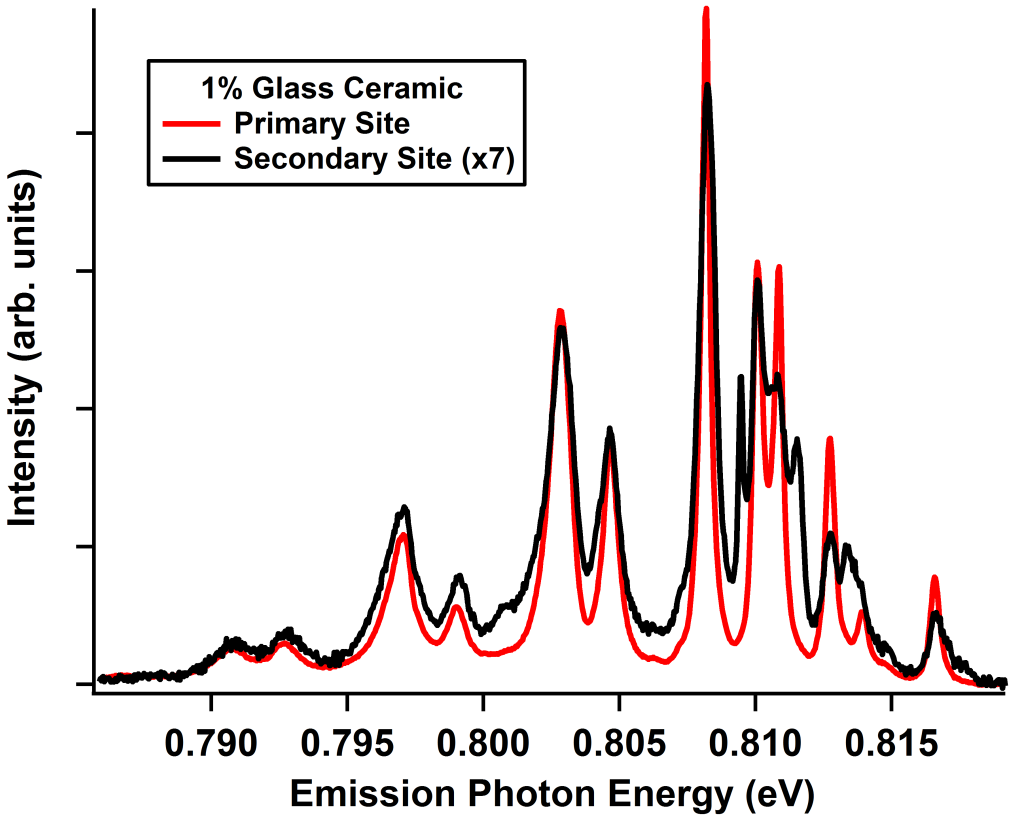

Figure 5.7: Emission profiles of the two different sites in the $Er_{.01}La_{.99}BGeO_5$ polycrystalline glass-ceramic.

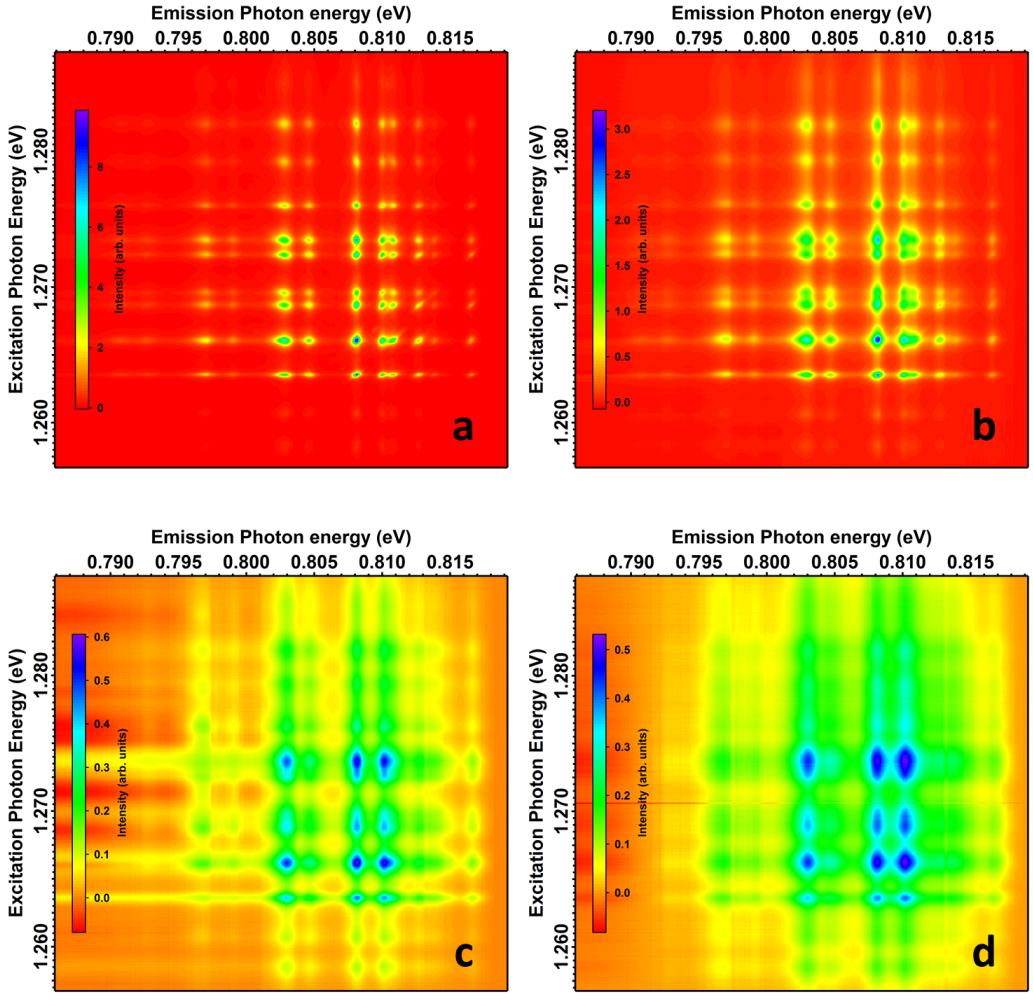

Figure 5.8: CEES maps for polycrystalline glass-ceramics with compositions of $Er_xLa_{1-x}BGeO_5$ where $x = .01$ (a), $x = .04$ (b), $x = .10$ (c), and $x = .20$ (d).

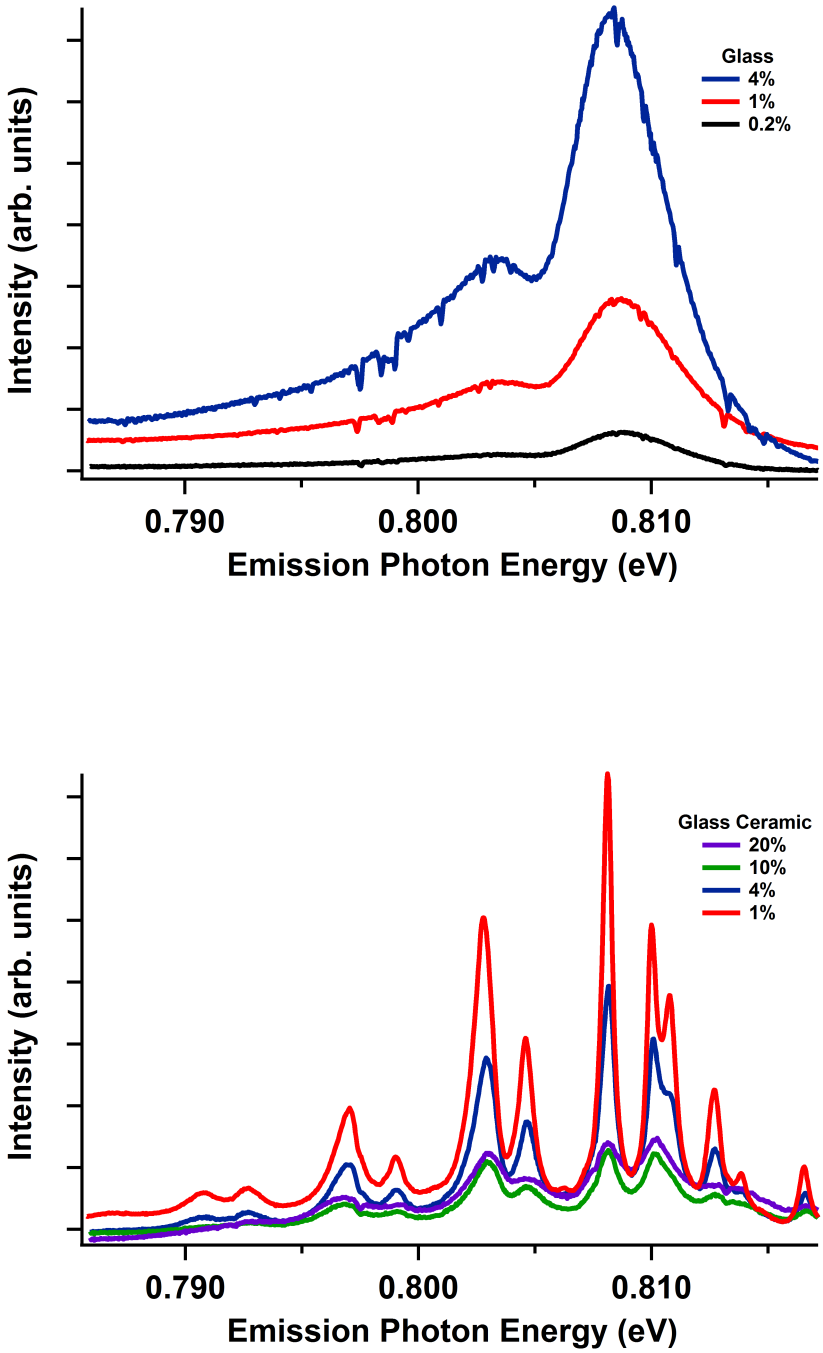

Figure 5.9: Top: Unscaled fluorescence emission spectra extracted from CEES maps of $Er_xLa_{1-x}BGeO_5$ glasses. Bottom: Unscaled fluorescence emission spectra extracted from CEES maps of polycrystalline glass-ceramics.

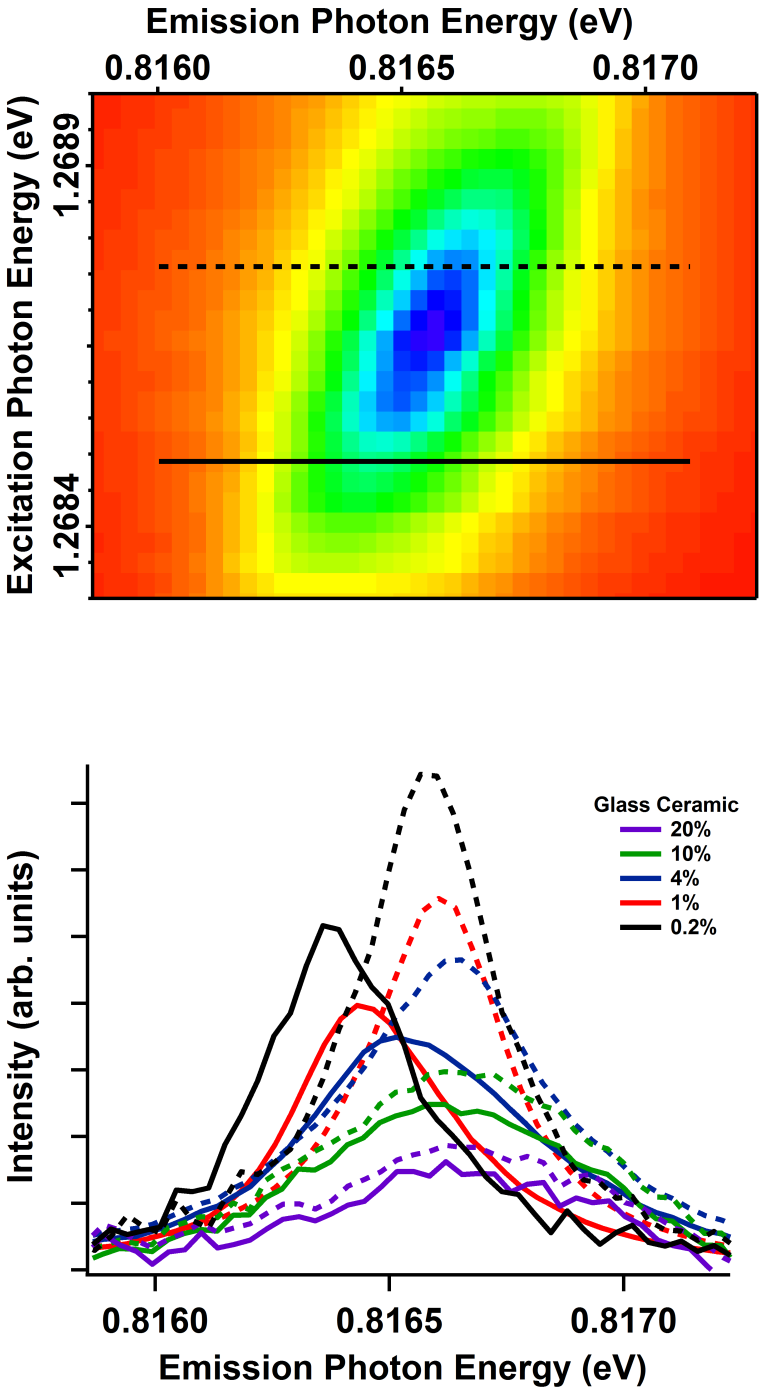

Figure 5.10: Top: Selected region of a CEES map showing fluorescence line narrowing. Bottom: Corresponding range of emission spectra from each difference composition. FLN is not observed in the glass-ceramics with greater erbium concentration, and the emission peak broadens significantly.

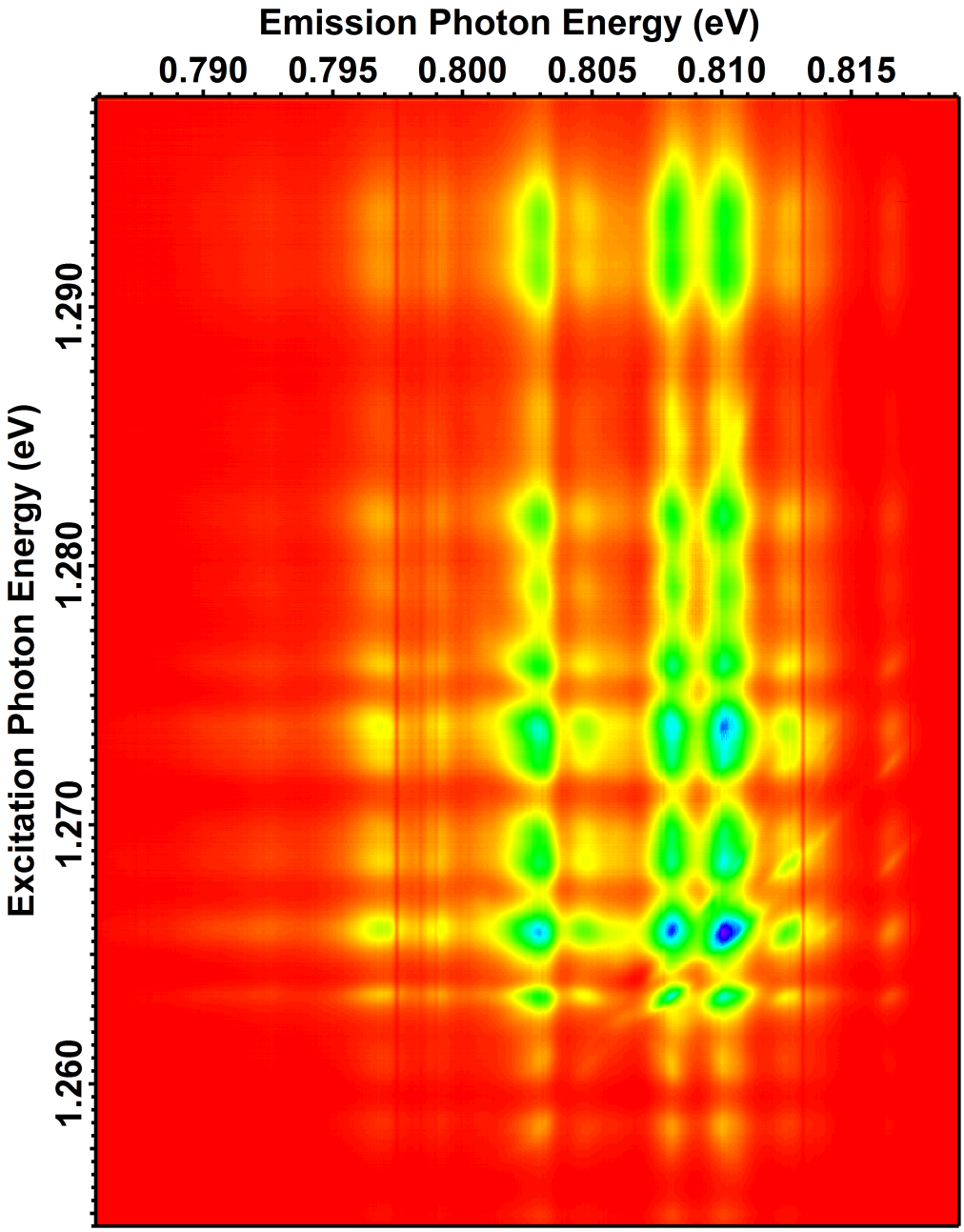

Figure 5.11: CEES map of 980nm excitation and 1550nm emission in a laser-induced crystal in $Er_{.01}La_{.99}BGeO_5$ glass.

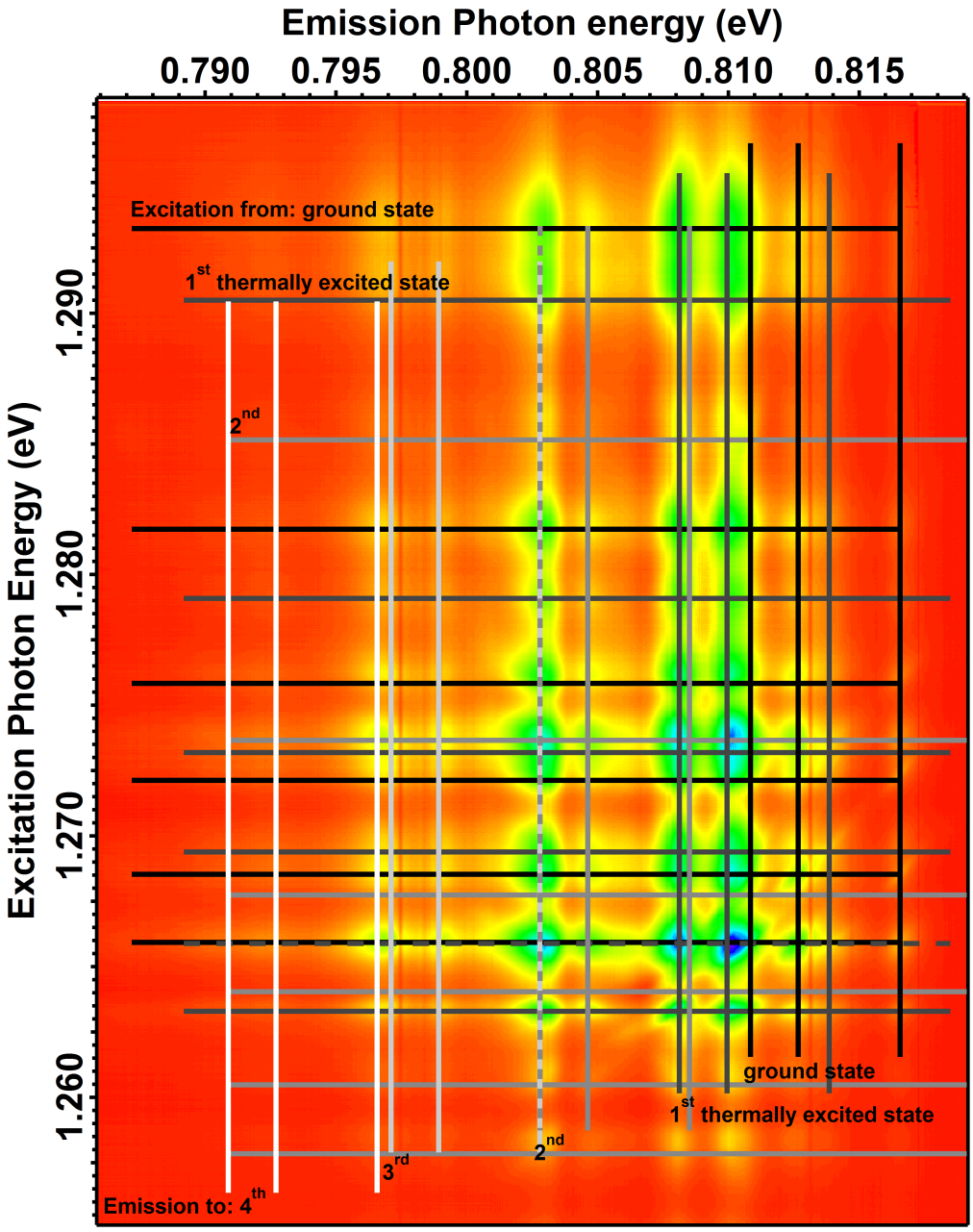

Figure 5.12: Overlay of Figure 5.11 with the same level assignment grid used for the glass-ceramic samples.

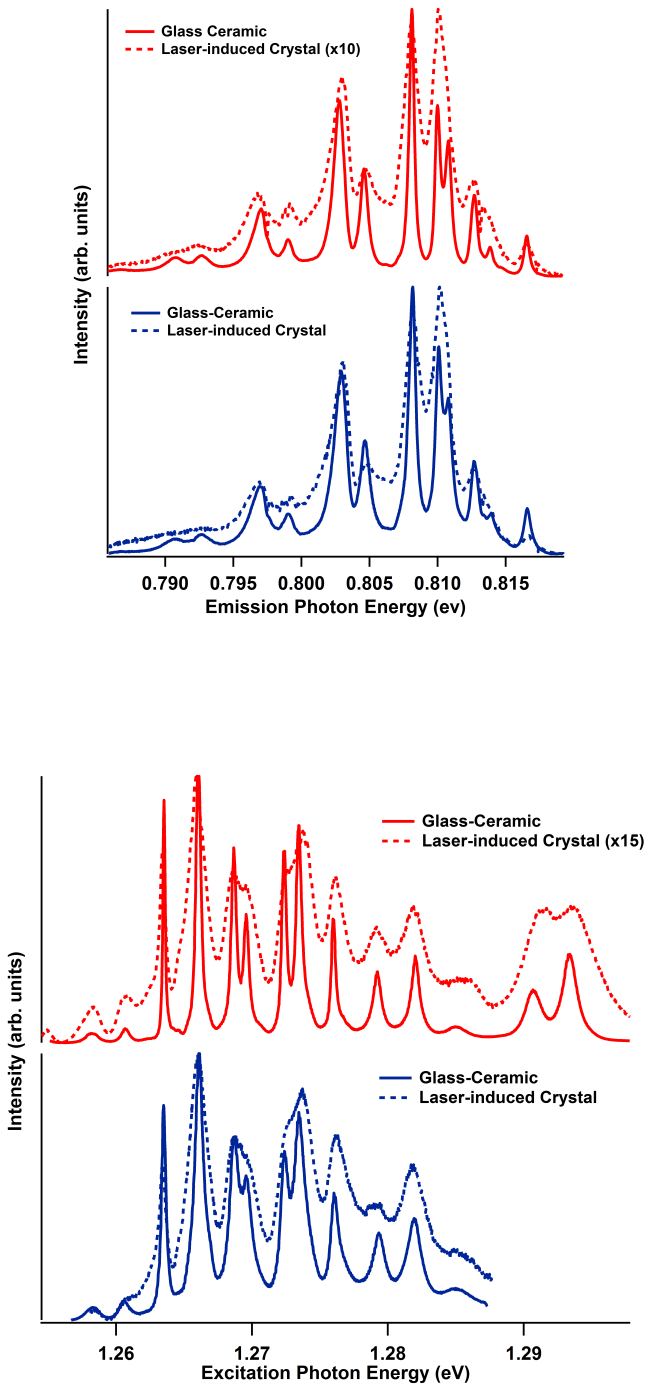

Figure 5.13: Emission (top) and excitation (bottom) spectra extracted from CEES maps of $Er_{.01}La_{.99}BGeO_5$ (red) and $Er_{.04}La_{.96}BGeO_5$ (blue) polycrystalline glass-ceramics (solid) and laser-induced crystals in glass (dashed). In all cases the spectra compare favorably.

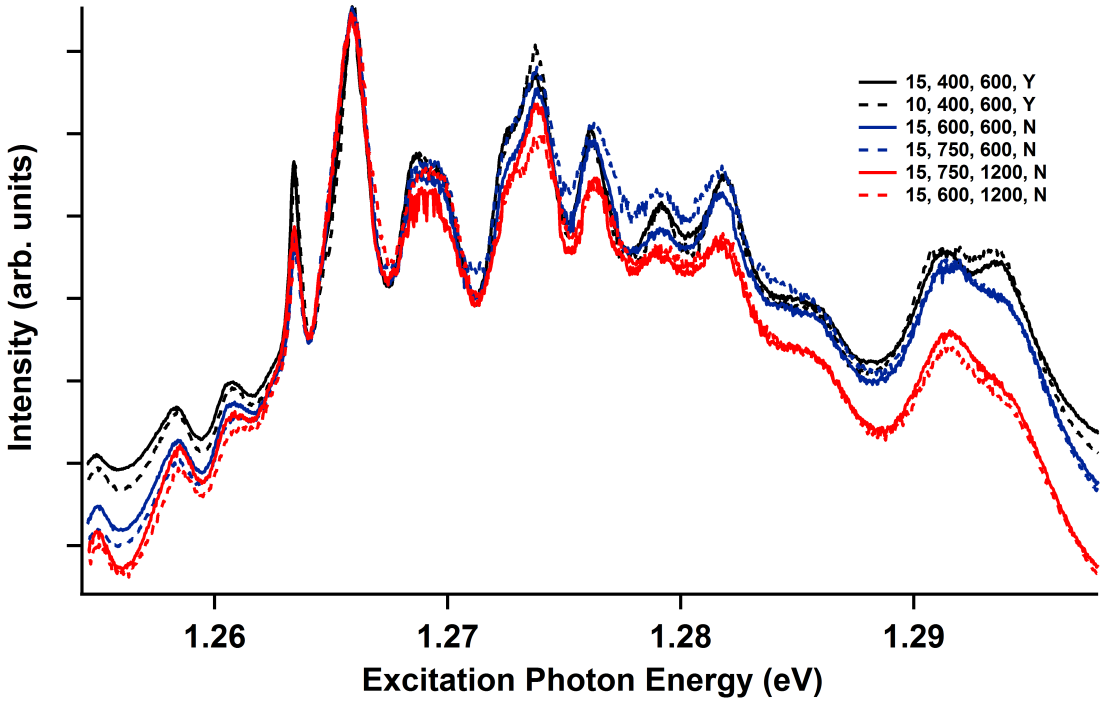

Figure 5.14: Fluorescence excitation spectra extracted from CEES maps collected from laser-induced crystals in $Er_{.01}La_{.99}BGeO_5$ glass grown under different conditions. The legend indicates the parameter values: write speed ($\mu m/s$), laser power (mW), focal depth (μm), and aberration correction (yes or no). In the order of the legend, from top to bottom, the crystals are er1-s2l1, er1-s2l3, er1-s1l9, er1-s1l7, er1-s1l2, and er1-s1l5, with respect to Table A.2.

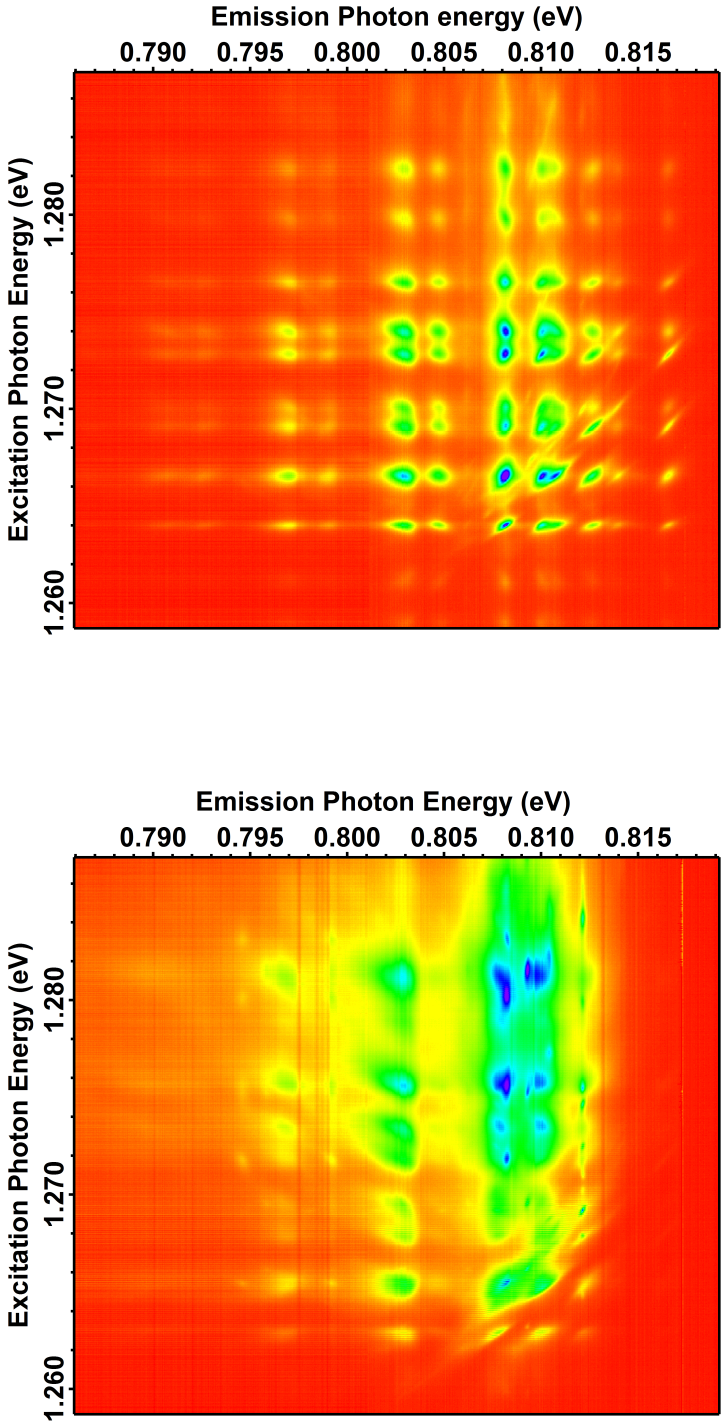

Figure 5.15: CEES maps of 980nm excitation and 1550nm emission in a polycrystalline glass-ceramic (top) and a laser-induced crystal in $Er_{.002}La_{.998}BGeO_5$ glass (bottom).

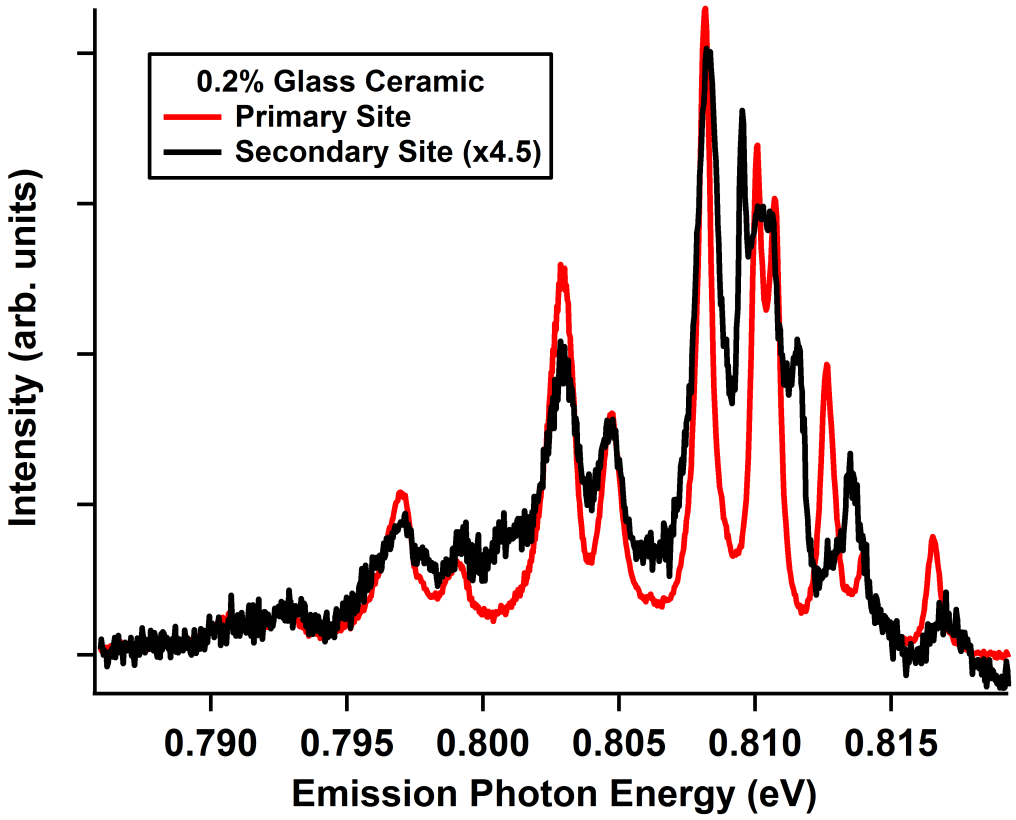

Figure 5.16: Emission profiles of the two different sites in the $Er_{.002}La_{.998}BGeO_5$ polycrystalline glass-ceramic.

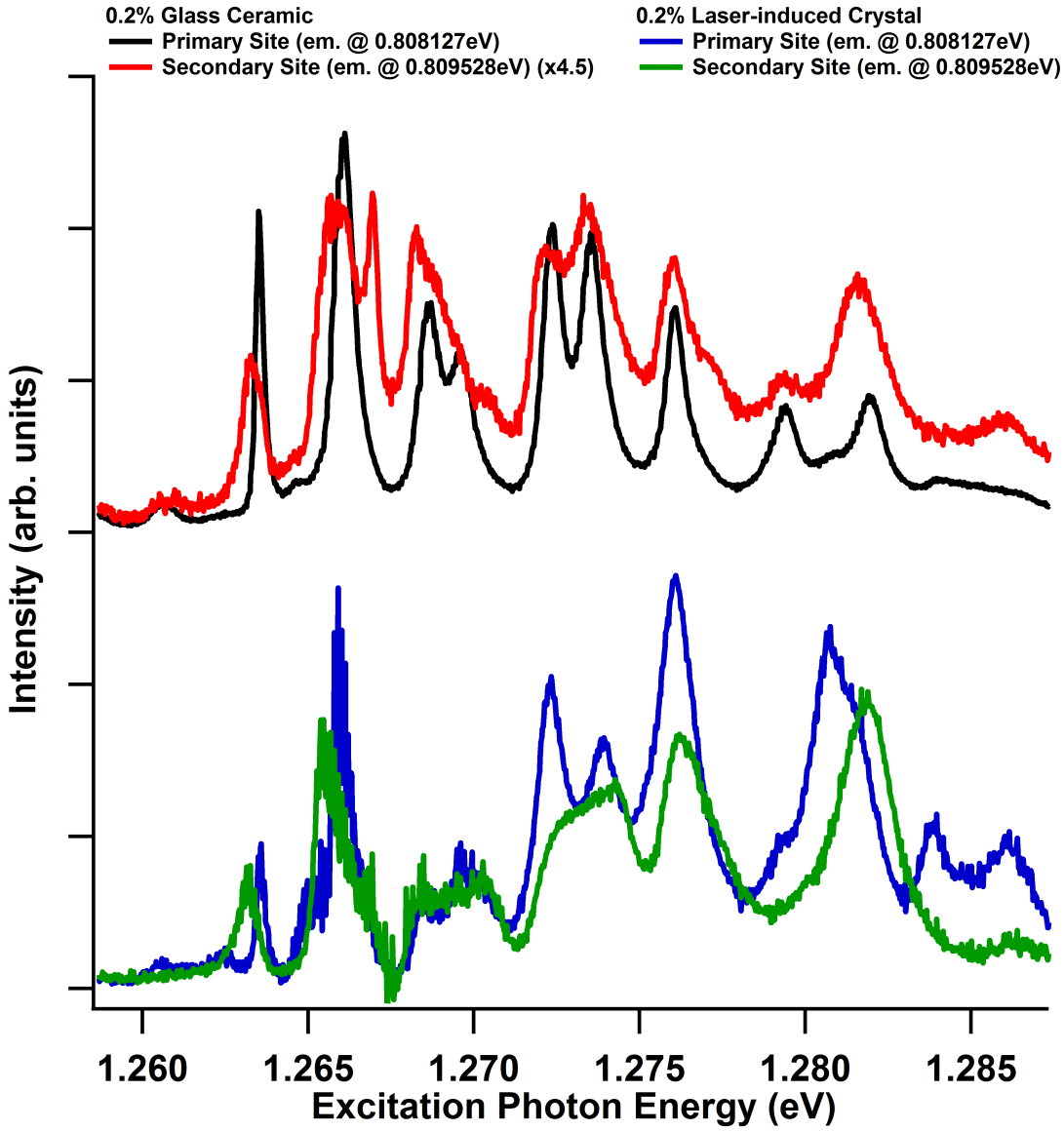

Figure 5.17: Excitation spectra of two different sites within the 0.2% laser-induced crystal (blue and green). The corresponding excitation spectra of the 0.2% glass-ceramic (black and red) are presented for comparison.

Chapter 6

Spatially Resolved Simultaneous Raman and Fluorescence Spectroscopy of Laser-Induced Crystals in Glass

The nature of the laser-irradiation technique necessarily results in a thermal gradient which covers a relatively large volume. Depending on the irradiation conditions, this gradient can vary from very steep to fairly flat. Thus, depending on the position within the volume, a crystal may more or less easily grow. This means that certain points within the final crystallized volume may have more or less strain than others. Coupled to this effect is the fact that the glass and crystal have different coefficients of thermal expansion. So not only will different points within the radial heat distribution expand by different amounts due to the thermal gradient, but following crystallization the crystalline region will contract by a different amount compared to the surrounding glass.

All of these issues create a potentially complicated spatial behavior for the structural and fluorescence properties of the crystal. Therefore, this section explores these properties via spatially resolved simultaneous Raman and fluorescence spectroscopy. It should be noted however, that because this data was collected using the scanning geometry depicted in Figure 3.3, the cross-sections of the crystalline lines were exposed, and thus potentially

relieved of some longitudinal strain.

Because of the cross-sectional area of the laser-induced crystals being investigated, collecting spectra at intervals which produce high spatial resolution results in an immense amount of data. This makes showing individual spectra impractical. Therefore, in order to visualize the occurring phenomena, two-dimensional maps of the crystal cross-sections were created in which a single spectral feature of interest is presented in color-space. The spectral features are, unless otherwise noted, the peak position and full-width half-max of the -803cm^{-1} and -207cm^{-1} Raman vibrational modes. These modes will hereafter be referred to as A(LO)$_{18}$ and E(TO)$_6$, respectively. According to Table 2.1, these modes correspond to symmetric Ge-O stretching and La displacement, respectively. The former was chosen for examination primarily due to its strength and the ease with which it is fitted. The latter was chosen due to the involvement of lanthanum, and therefore its potential sensitivity to the presence of erbium. Finally the total integrated erbium fluorescence intensity (EFI) from 515nm-572nm, which corresponds to emission from both the $^4S_{3/2}$ and $^2H_{11/2}$ multiplets to the $^4I_{15/2}$ multiplet, was mapped.

6.1 Erbium-doped LaBGeO$_5$ glass ceramics

As discussed in Chapter 5, under resonant excitation at low temperature, the total EFI showed a small deviation from proportionality to the erbium concentration in Er:LaBGeO$_5$ glasses and a large deviation in Er:LaBGeO$_5$ glass ceramics. Under 488nm excitation at room temperature, however, the fluorescence follows the concentration extremely well, and is shown in Figure 6.1. The reason for this is that due to the smaller collection volume and significantly lower absorption, not all of the incident light is absorbed, and the emitted intensity will remain proportional to the total number of erbium ions as in the glass. In addition to this, the excited states in this case are entirely different and have much shorter

lifetimes, and thus the non-radiative decay channels which were proposed to explain the deviation of the EFI from concentration proportionality under resonant excitation at $980nm$ may not play a role following excitation at $488nm$.

It is important to note that the total integrated EFI from the glass-ceramics is less than that of the corresponding glass. This makes sense given the two erbium incorporation sites observed in the CEES data. In the glass, the absorption is broad, but all ions have the same probability of absorbing the incident light, and as the dopant concentration increases, this probability remains the same for any erbium ions within the excitation/emission volume. Ideally, when the glass is crystallized, the dopant ions will incorporate at a single site, and the single absorption peak of the glass will simply narrow due to the presence of the crystal field and remain centered at the same energy, as depicted in Figure 6.3. In the Er:$LaBGeO_5$ glass-ceramics, however, the erbium ions are divided amongst the primary site, the secondary site, and any other tertiary sites which are not identifiable in the CEES maps. Since the glass-ceramics exhibit less fluorescence than their corresponding glasses, and the number of erbium ions at the secondary site is small, the actual absorption scenario is potentially closer to that of Figure 6.4. In this figure, hypothetical absorption curves for the primary site and secondary sites are overlayed with the measured absorbance curve for the glass. As opposed to the ideal case, the crystal field in this case shifts the absorption peak for the primary site away from $488nm$. The existence of the secondary site reduces the total number of ions at the primary site, but its absorption peak lies closer to $488nm$. Thus, in glass-ceramics containing erbium ions mostly incorporated at the primary site, the absorption will be less than in the corresponding glass, and therefore, the emission will be also be reduced, but still dominated by the primary site. If the composition of the glass causes the ratio of the number of erbium ions incorporating in the primary site compared to the secondary site, the absorption peak intensities will change, and the total EFI observed becomes greater in the glass-ceramic than in the glass. This scenario is depicted in Figure

6.5. At low temperature, the absorption peaks narrow significantly, and since the absorption of neither site overlaps perfectly with $488nm$, little to no excitation occurs, and thus little to no fluorescence emission was observed.

Raman spectra of the erbium-doped glass-ceramics are shown in Figure 6.2. Excepting the increasing incursion of the erbium fluorescence into the spectral range of the Raman modes, the spectra are all very similar, both to one another, and to the spectra of undoped $LaBGeO_5$ presented in Figure 2.5.

6.2 Undoped $LaBGeO_5$

As a baseline and standard by which to compare all of the laser-induced crystals in erbium-doped $LaBGeO_5$ glasses, Raman scans were performed on the exposed cross-sections of laser-induced crystals in undoped $LaBGeO_5$ glass. In this work these crystals will be referred to as udc-s1l2 and udc-s1l5 and were chosen for this purpose because they exhibited both the most consistent cross-section profile from end to end and the lowest power losses ($2.64dB/cm$ and $6.71dB/cm$, respectively) in waveguiding measurements (see Chapter 6 of Stone [5] for details). The growth conditions for both lines were identical and are listed in Table A.2.

Figures 6.6 and 6.7 present maps of the peak position and FWHM of the $A(LO)_{18}$ and $E(TO)_6$ Raman modes for udc-s1l2, respectively. Two maps of each spectral feature are shown: one in which the colorscale range is large, allowing comparison between the glass and crystalline regions, and one in which the colorscale range is small, allowing a better visualization of the behavior within the crystalline region. Figures 6.8 and 6.9 show the same set of maps for udc-s1l5.

The Raman modes behave the same way in both crystals; the $A(LO)_{18}$ mode shifts toward lower energies away from the center of the crystal and the $E(TO)_6$ mode shifts toward

higher energies away from the center of the crystal. Both modes broaden toward the outer edge of the crystal. Within the finer details of the crystals, these shifts and broadenings behave differently in different regions. These regions correlate well with the model of growth dynamics proposed in Chapter 5 of Stone [5], which consists of two different transverse growth zones.

Coussa *et al.* observed via *in situ* Raman spectroscopy that applying hydrostatic pressure using a diamond anvil to a $LaBGeO_5$ single crystal causes the $A(LO)_{18}$ Raman mode to shift to higher energy [94]. Considering this, and given the observed shifts within the laser-induced crystals, either the center of the crystal experiences compressive strain or the edges of the crystal experience tensile strain due to the surrounding glass. For udcs1l2, the magnitude of the shift from the center of the crystal to the edge is approximately $2.5cm^{-1}$. Based on the data of Coussa, this corresponds to a pressure of approximately $2.5cm^{-1}/3.3cm^{-1}GPa^{-1}$ =0.75GPa, which, along the 5.5μm semi-minor radius, equates to a strain gradient of $0.14GPa/\mu m$ in this direction.

The boundary between the glass and crystalline regions is of interest due to the uncertainty concerning how the transition occurs. Indeed, some of the maps in Figures 6.6 to 6.9 exhibit strange behavior at the boundary, with a region surrounding the crystal which is one or two pixels wide whose values are somewhat different than the immediately adjacent pixels in either the glass or crystal. Figure 6.10a repeats Figure 6.6a and includes an overlay of the Raman shift line profile from $y = 25\mu m$, which is characteristic of the boundary in all directions. According to the line profile, the energy of the Raman mode spikes sharply back to about the same value as in the center of the crystal before dropping off in the glassy region. To better understand this behavior, it is useful to consult the individual spectrum from this point and compare it to its surroundings. Figure 6.10c presents the boundary spectrum as well as three adjacent spectra in each direction, along with the artificial spectrum created by the initial fitting guesses. The boundary spectrum is almost

indistinguishable from the typical glass spectrum. Therefore, this phenomenon seems to be an artifact of the curve-fitting process. Figure 6.10b shows a map of the absolute value of the error reported by IGOR Pro. Within the crystalline region the error is extremely low ($< 0.1cm^{-1}$). In the glassy region the error is, unsurprisingly, large. However, at the boundary, the magnitude of the error takes an intermediate value. It is unclear why, despite the similarity of the spectrum to that of the glass, the curve-fitting procedure produces this effect at the boundary.

6.3 Erbium-doped $LaBGeO_5$

Spatially resolved maps of the chosen spectral features in laser-induced crystal lines in $Er_{.01}La_{.99}BGeO_5$ and $Er_{.04}La_{.96}BGeO_5$ glasses are presented in Figures 6.11 to 6.18. Each figure contains a spatial map of the normalized erbium fluorescence intensity in addition to the corresponding maps concerning the $A(LO)_{18}$ and $E(TO)_6$ Raman modes. A number of interesting effects are immediately apparent.

First, except for crystal er1-s2l13, shown in Figure 6.14, all of the crystal cross-sections are fairly symmetric about the longitudinal (i.e. the modifying laser incidence) axis. This is a significant difference from the asymmetric crystals produced in undoped $LaBGeO_5$ discussed previously in this section, as well as others observed by Stone [5]. The reason for this difference is unclear, but could be related to the very different writing speeds used. However, it should be noted that the writing speed is growth-limited, and therefore only a narrow range of speeds may be used to produce a continuous crystal line.

Second, although the Raman modes still shift in the same manner from the center of the crystals towards their edges, the crystals do not appear to exhibit the type of internal structure observed in the undoped crystals. This is likely an unfortunate consequence of the lower spectral resolution due to scanning these samples with the $15cm$ spectrometer,

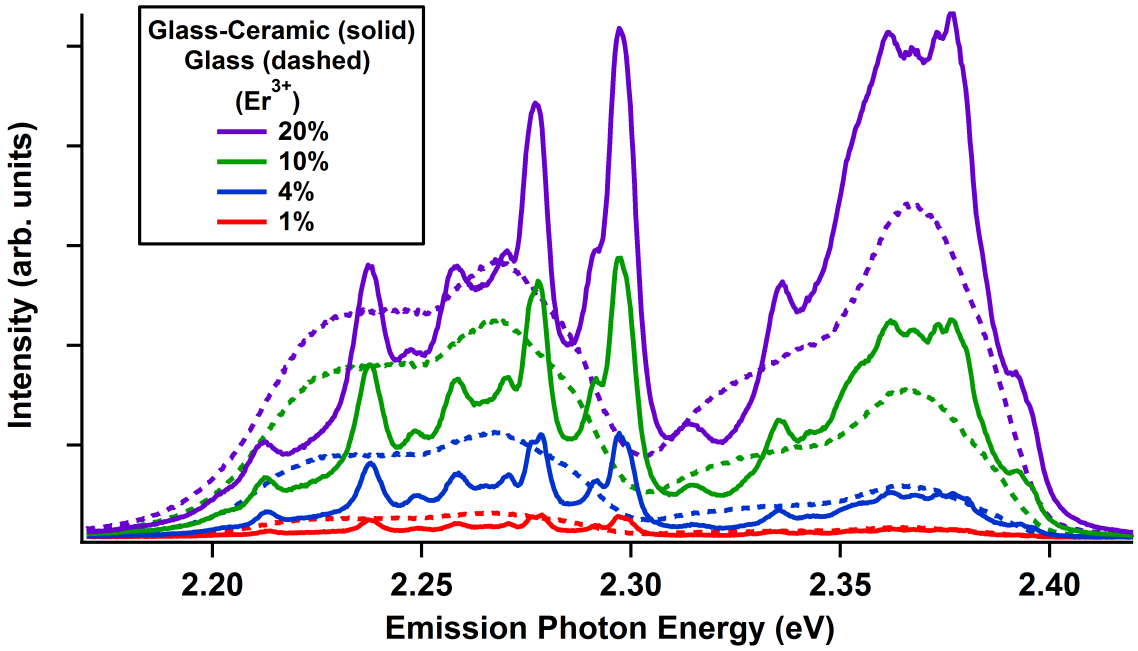

Figure 6.1: Room temperature erbium fluorescence spectra for $Er_xLa_{1-x}BGeO_5$ glass-ceramics and glasses, where x=0.01, 0.04, 0.10, and 0.20. The observed fluorescence corresponds to transitions from the $^4S_{3/2}$ and $^2H_{11/2}$ multiplets to the $^4I_{152}$ multiplet.

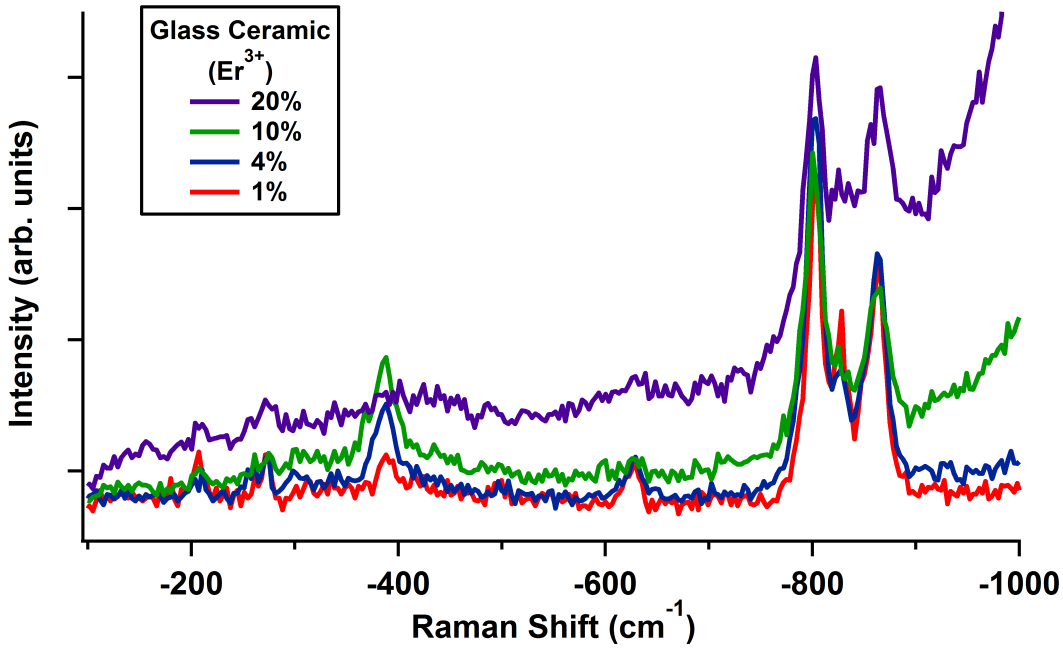

Figure 6.2: Room temperature Raman spectra for $Er_xLa_{1-x}BGeO_5$ glass-ceramics, where x=0.01, 0.04, 0.10, and 0.20.

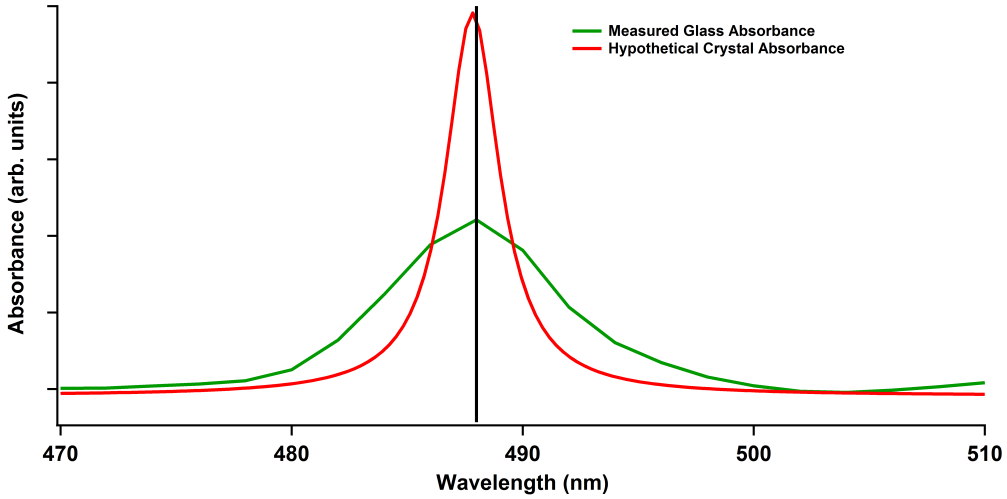

Figure 6.3: Measured absorbance curve for $Er_{.1}La_{.99}BGeO_5$ glass, and a hypothetical absorbance curve representing the ideal scenario upon crystallization. Upon crystallization the absorption peak of the glass narrows and remains centered at the same energy. Since the number of optically active ions remains the same, the area under each curve should be the same. The vertical black line denotes the location of $488nm$.

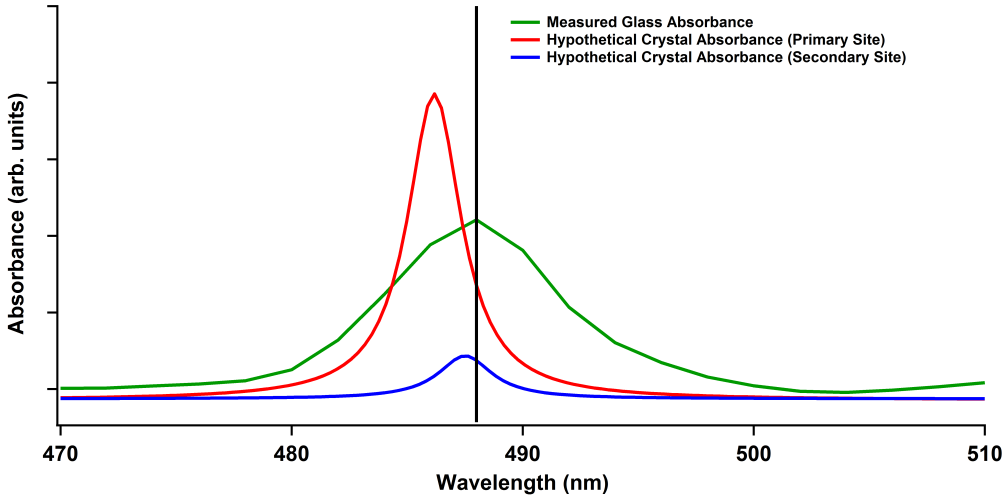

Figure 6.4: Measured absorbance curve for $Er_{.1}La_{.99}BGeO_5$ glass, and hypothetical absorbance curves representing the two different erbium incorporation sites in crystalline Er:$LaBGeO_5$. The relative intensities of the primary and secondary site are proportional to the number of erbium ions in each, with the primary site greatly outnumbering the secondary site. However, since the number of optically active ions ideally remains the same, the area under the two crystalline curves should equal the area under the glass curve. The vertical black line denotes the location of $488nm$.

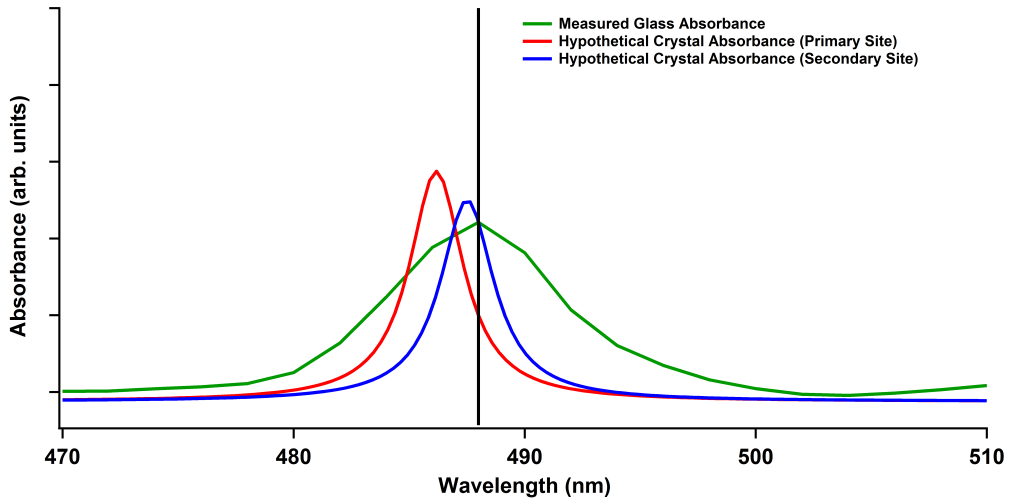

Figure 6.5: Measured absorbance curve for $Er_{.1}La_{.99}BGeO_5$ glass, and hypothetical absorbance curves representing the two different erbium incorporation sites in crystalline Er:$LaBGeO_5$. The relative intensities of the primary and secondary site are proportional to the number of erbium ions in each, with the secondary site population now approaching that of the primary site. However, since the number of optically active ions ideally remains the same, the area under the two crystalline curves should equal the area under the glass curve. The vertical black line denotes the location of $488nm$.

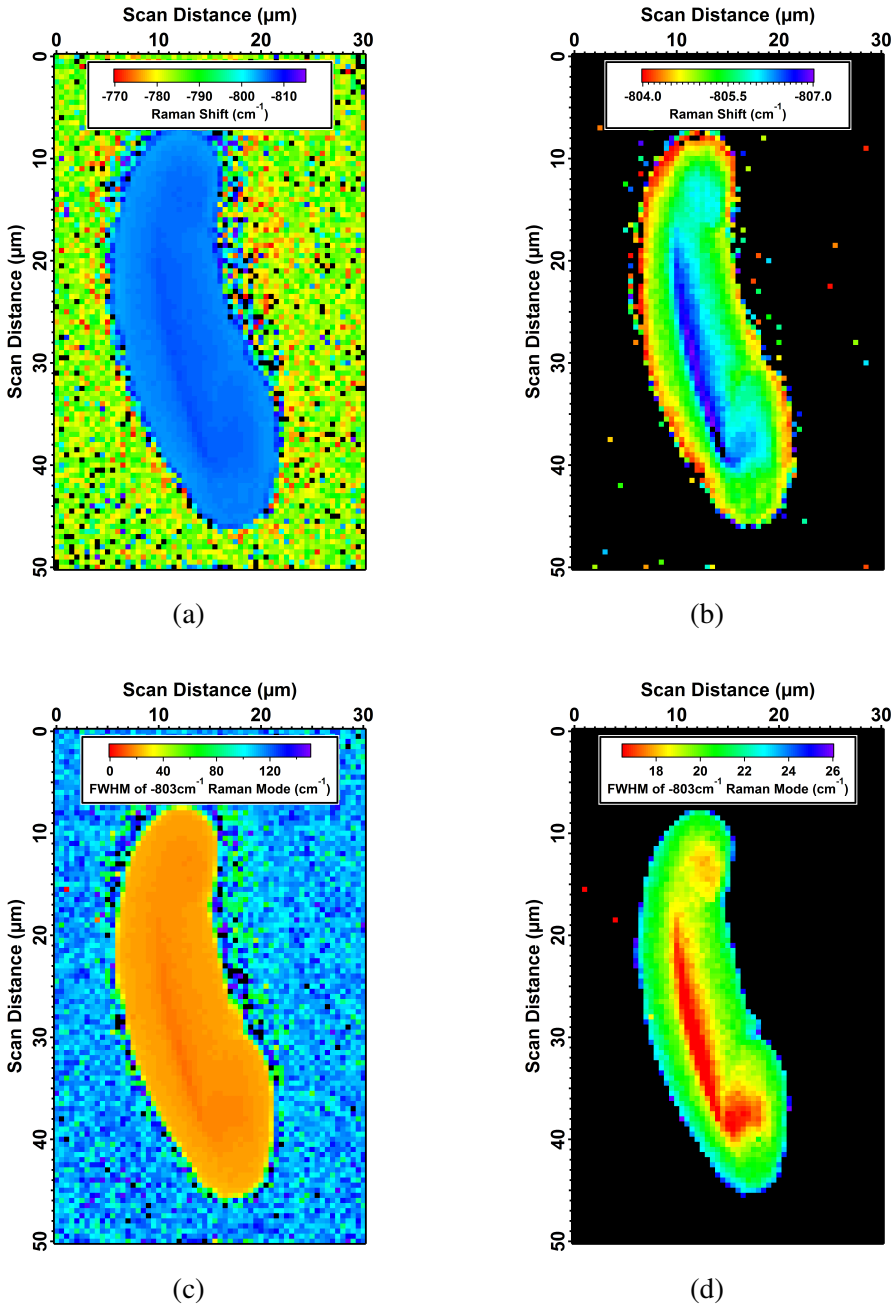

Figure 6.6: Low (a and c) and high (b and d) contrast spatially resolved maps of the peak position (a and b) and FWHM (c and d) of the $A(LO)_{18}$ Raman mode for crystal udc-s1l2.

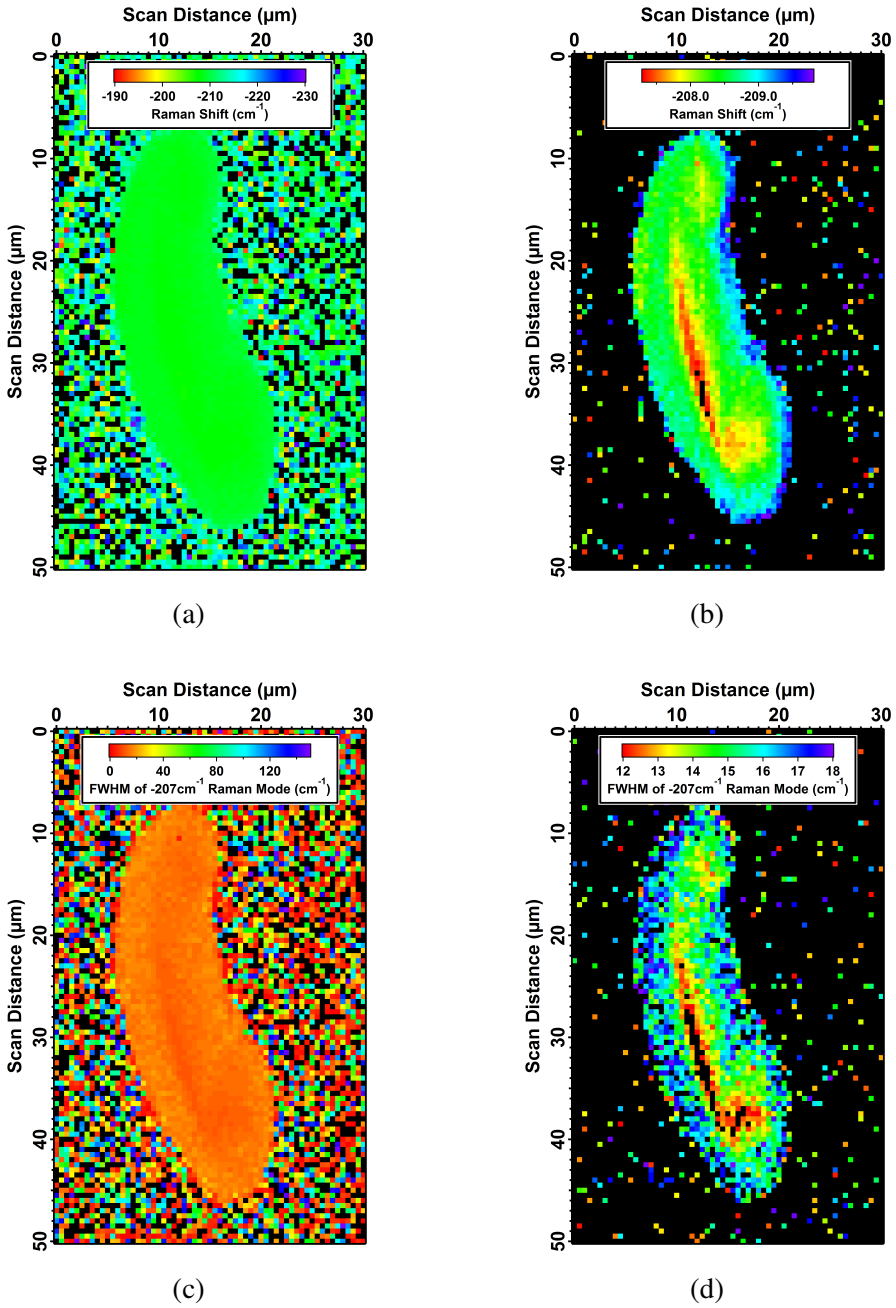

Figure 6.7: Low (a and c) and high (b and d) contrast spatially resolved maps of the peak position (a and b) and FWHM (c and d) of the $E(TO)_6$ Raman mode for crystal udc-s1l2.

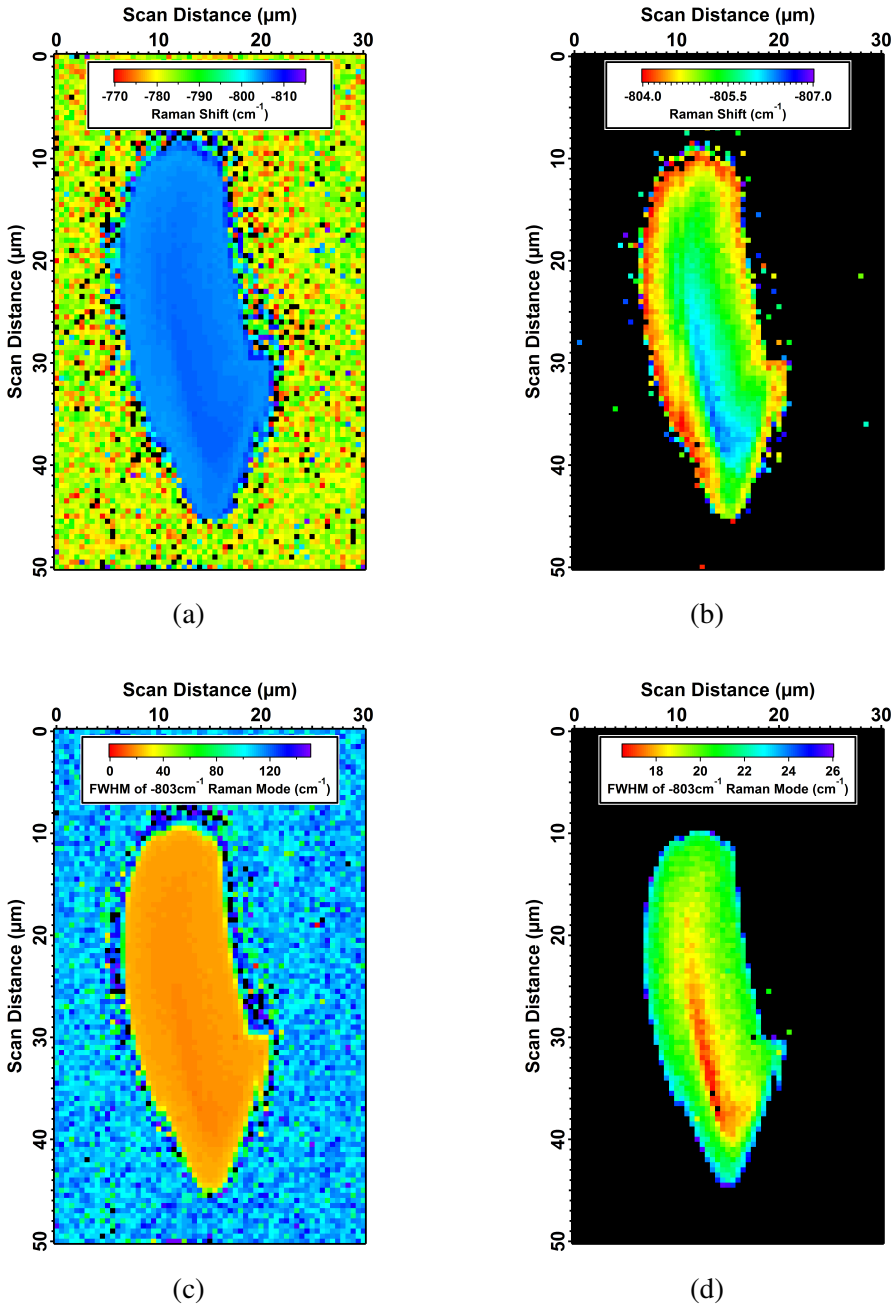

Figure 6.8: Low (a and c) and high (b and d) contrast spatially resolved maps of the peak position (a and b) and FWHM (c and d) of the $A(LO)_{18}$ Raman mode for crystal udc-s1l5.

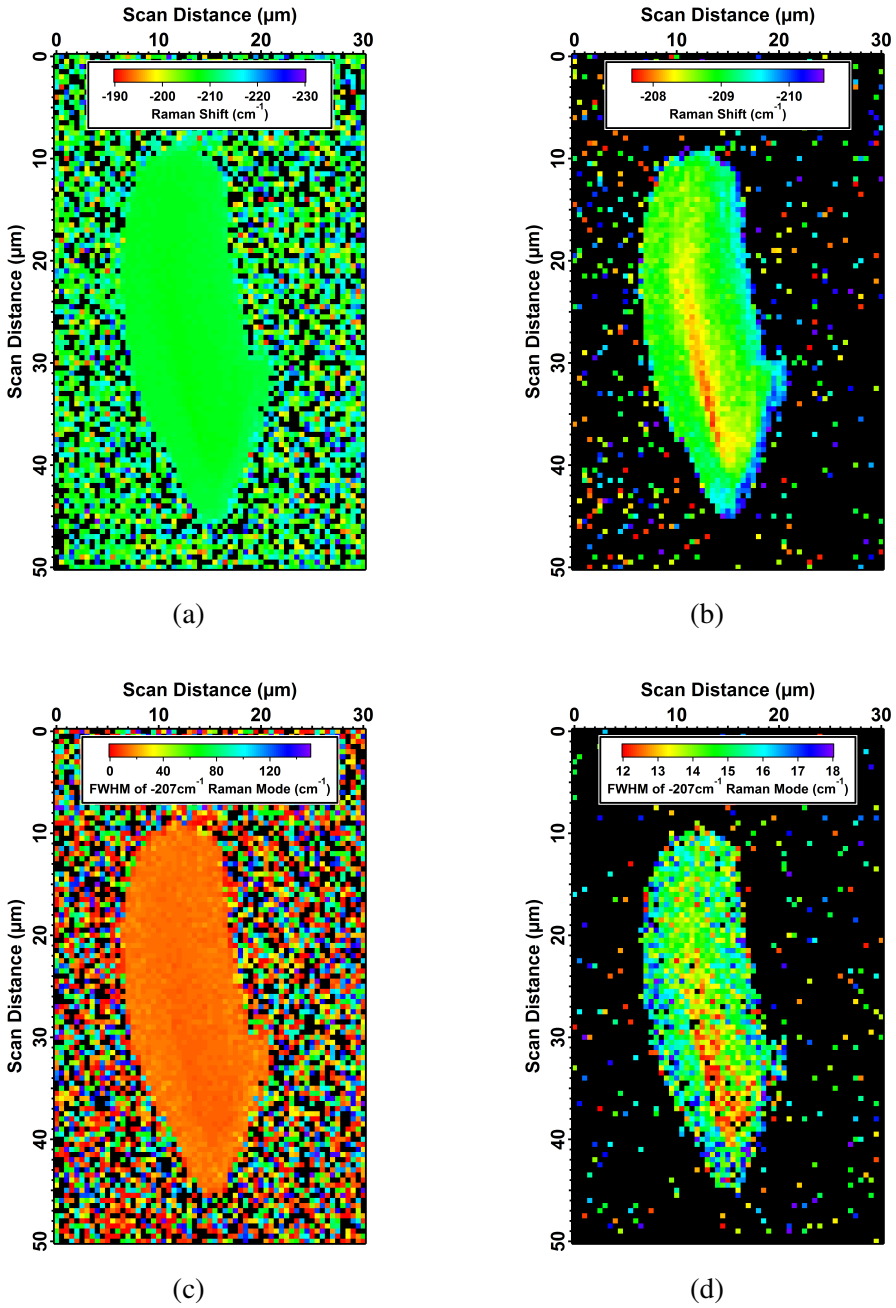

Figure 6.9: Low (a and c) and high (b and d) contrast spatially resolved maps of the peak position (a and b) and FWHM (c and d) of the $E(TO)_6$ Raman mode for crystal udc-s1l5.

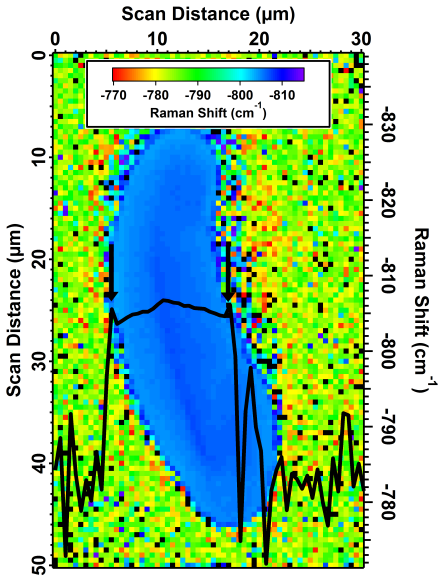

(a)

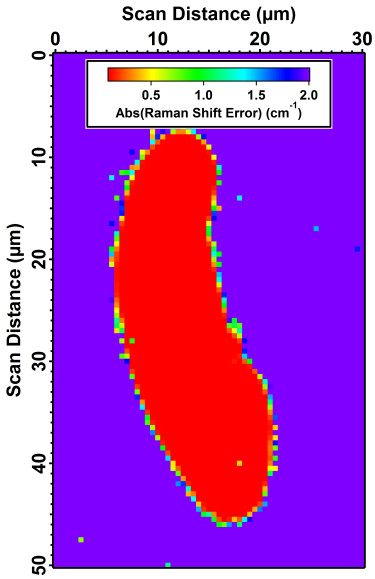

(b)

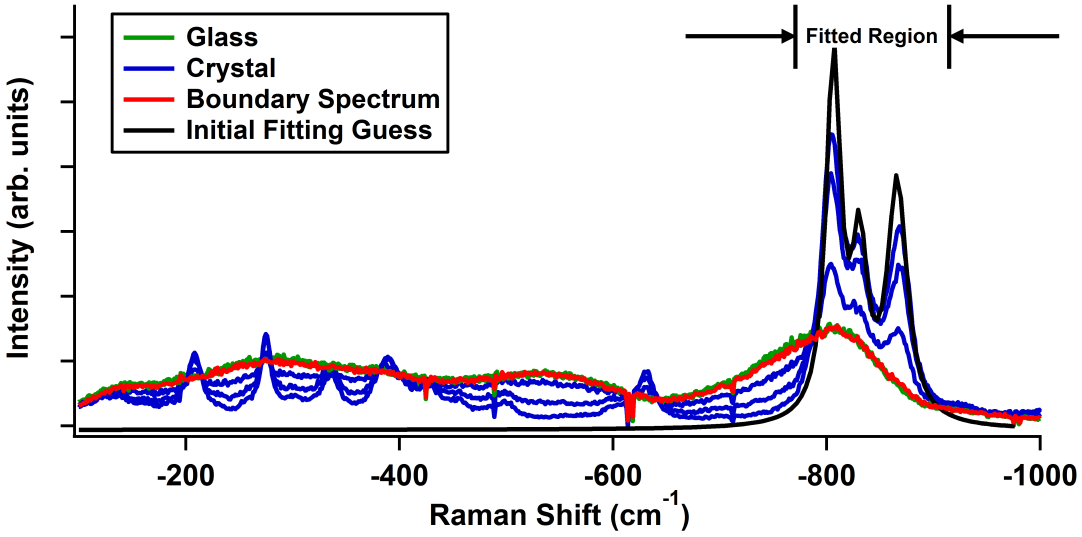

(c)

Figure 6.10: (a) Figure 6.6a overlayed with a horizontal line profile which illustrates the anomalous spike in the fitted parameter at the glass/crystal boundary. (b) The error output of the fitting procedure corresponding to Figure 6.6a. (c) Individual Raman spectra from the boundary and its surroundings, as well as the initial guess function provided to the fitting procedure.

instead of the $50cm$ spectrometer, which was used for the undoped samples, rather than a true absence of internal structure. As discussed in Chapter 3, this choice was made to enable comparison of the erbium fluorescence to the overall structure (glass vs. crystal). Macroscopically, the growth parameters and concentration, within the limited range which was investigated, do not significantly impact the energy and width of the Raman modes.

Finally, the erbium fluorescence intensity within the crystalline region is inhomogeneously distributed, and in some crystals, appears to exhibit signs of internal structure. As with the glass-ceramics, the EFI is less within the crystalline region compared to the surrounding glass. While the spectral resolution prevents correlation of some of the finer inhomogeneity of the EFI to small fluctuations of the Raman modes, crystal er1-s2l3 exhibits a strong enough inhomogeneity so as to allow comparison. Line profiles of the peak position of the $A(LO)_{18}$ Raman mode and total EFI across the cross-section of this crystal are compared in Figure 6.19. Their agreement implies a strong correlation between the frequency of the Raman modes and the amount of erbium fluorescence emission. A reasonable explanation for this phenomenon is that as the structure changes ever so slightly, the narrow absorption peaks of the erbium incorporation sites are shifted either nearer or further from the energy of the excitation source.

In addition to this effect, erbium ions may potentially have diffused outward and into the surrounding glass during the crystallization process. This possibility is strongly suggested by the EFI maps of Figures 6.11 to 6.18 and is further explored in Figure 6.20, in which a typical spectrum from the region of enhanced EFI is compared to spectra from the glass and crystal regions. While the boundary spectrum is predominantly glassy in nature, some weak crystalline features are also present. The shape of the crystalline contribution to the fluorescence in this region matches that typical of the primary site rather than he secondary site. Thus, the primary site is still the predominant site, and therefore the total EFI would be expected to be diminished. Since the secondary site is still negligible, that the intensity

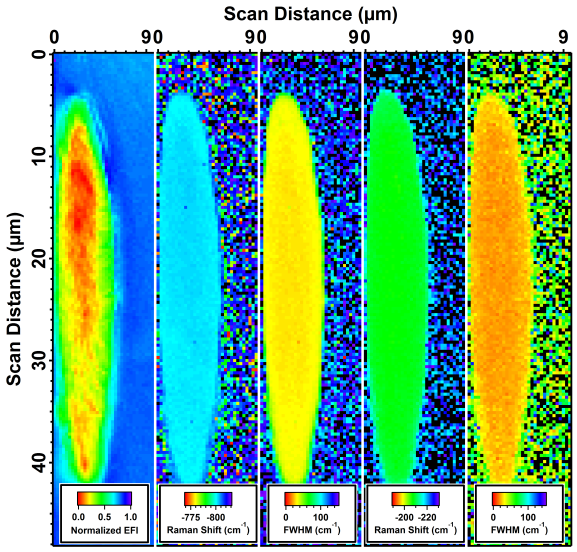

Figure 6.11: Spatially resolved maps of (L to R) erbium fluorescence intensity, A(LO)1_{18} peak position, A(LO)$_{18}$ FWHM, E(TO)$_6$ peak position, and E(TO)$_6$ FWHM for crystal er1-s1l2.

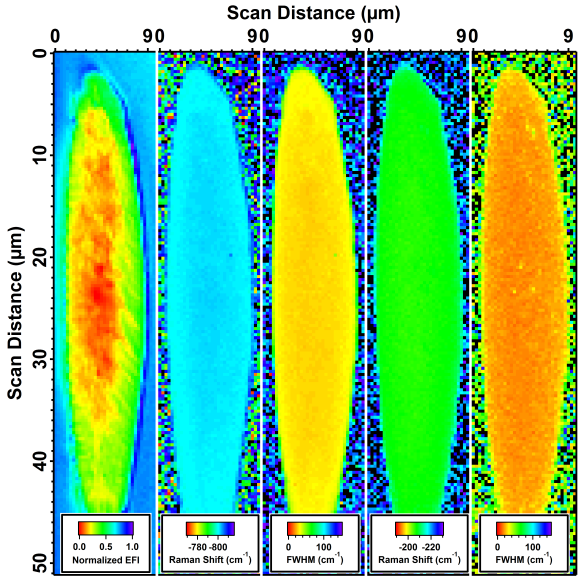

Figure 6.12: Spatially resolved maps of (L to R) erbium fluorescence intensity, A(LO)$_{18}$ peak position, A(LO)$_{18}$ FWHM, E(TO)$_6$ peak position, and E(TO)$_6$ FWHM for crystal er1-s1l6.

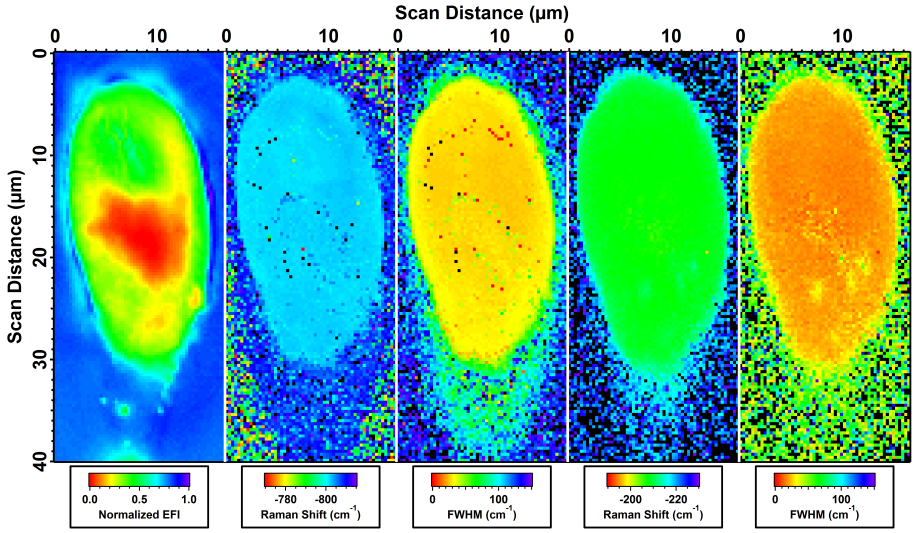

Figure 6.13: Spatially resolved maps of (L to R) erbium fluorescence intensity, $A(LO)_{18}$ peak position, $A(LO)_{18}$ FWHM, $E(TO)_6$ peak position, and $E(TO)_6$ FWHM for crystal er1-s2l3.

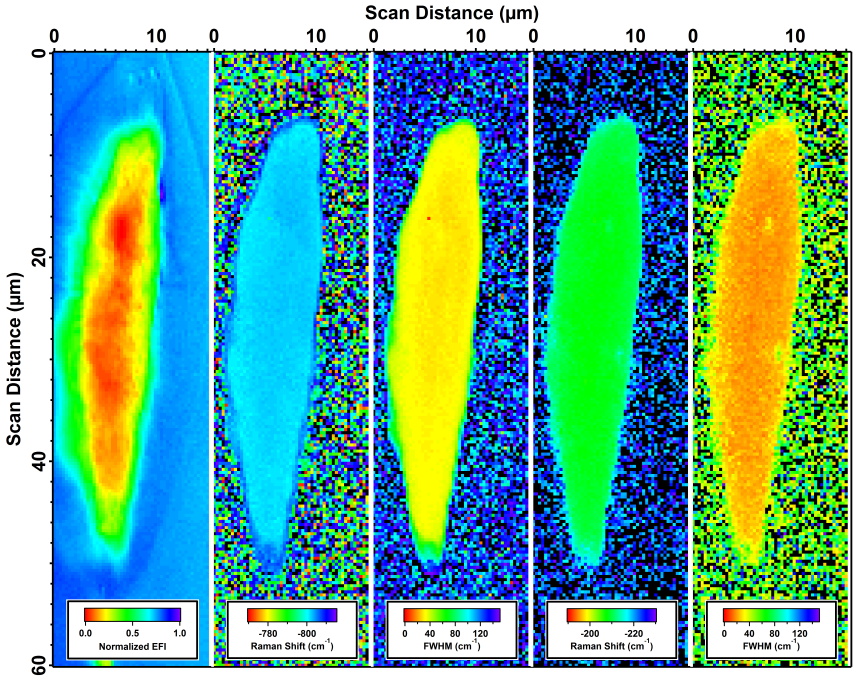

Figure 6.14: Spatially resolved maps of (L to R) erbium fluorescence intensity, $A(LO)_{18}$ peak position, $A(LO)_{18}$ FWHM, $E(TO)_6$ peak position, and $E(TO)_6$ FWHM for crystal er1-s2l13.

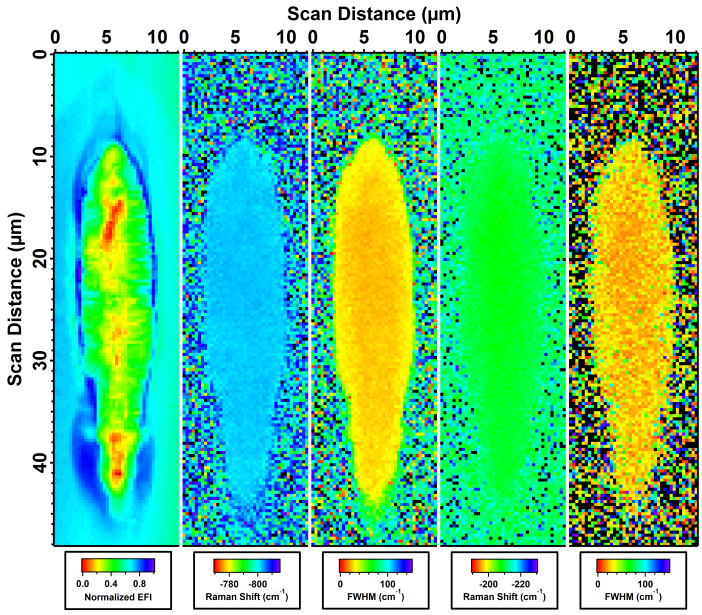

Figure 6.15: Spatially resolved maps of (L to R) erbium fluorescence intensity, $A(LO)_{18}$ peak position, $A(LO)_{18}$ FWHM, $E(TO)_6$ peak position, and $E(TO)_6$ FWHM for crystal er4-s1l2.

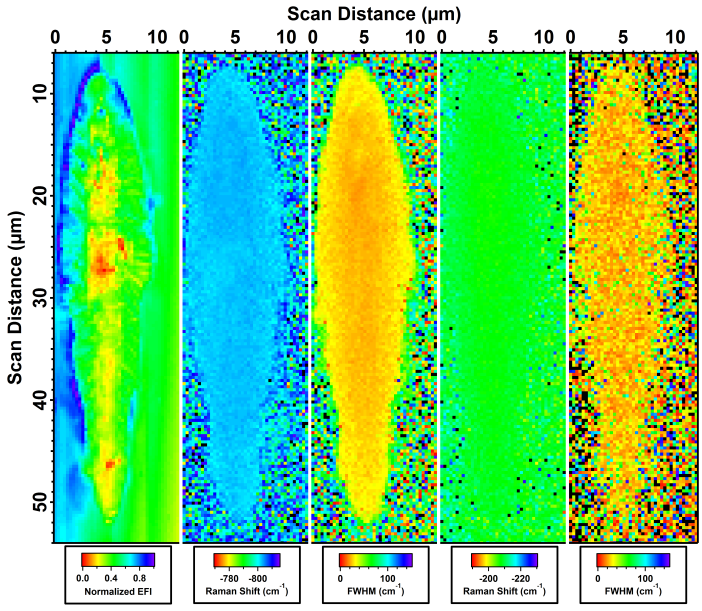

Figure 6.16: Spatially resolved maps of (L to R) erbium fluorescence intensity, $A(LO)_{18}$ peak position, $A(LO)_{18}$ FWHM, $E(TO)_6$ peak position, and $E(TO)_6$ FWHM for crystal er4-s1l6.

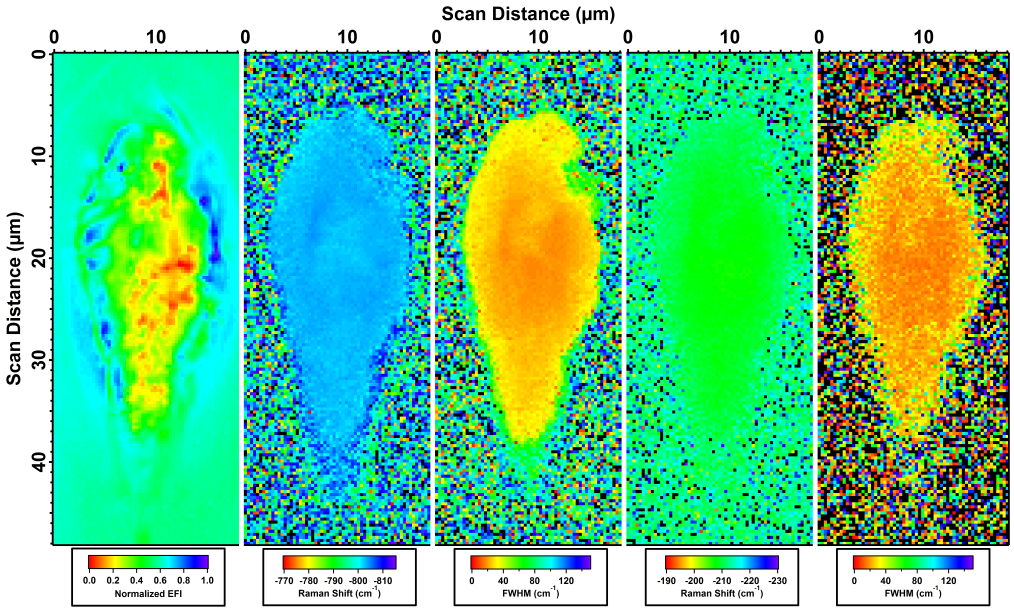

Figure 6.17: Spatially resolved maps of (L to R) erbium fluorescence intensity, $A(LO)_{18}$ peak position, $A(LO)_{18}$ FWHM, $E(TO)_6$ peak position, and $E(TO)_6$ FWHM for crystal er4-s2l1.

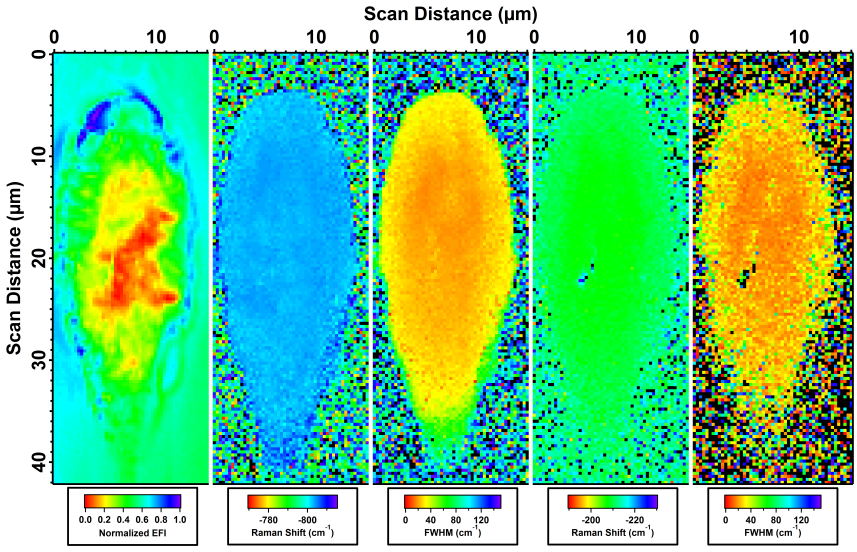

Figure 6.18: Spatially resolved maps of (L to R) erbium fluorescence intensity, $A(LO)_{18}$ peak position, $A(LO)_{18}$ FWHM, $E(TO)_6$ peak position, and $E(TO)_6$ FWHM for crystal er4-s2l5.

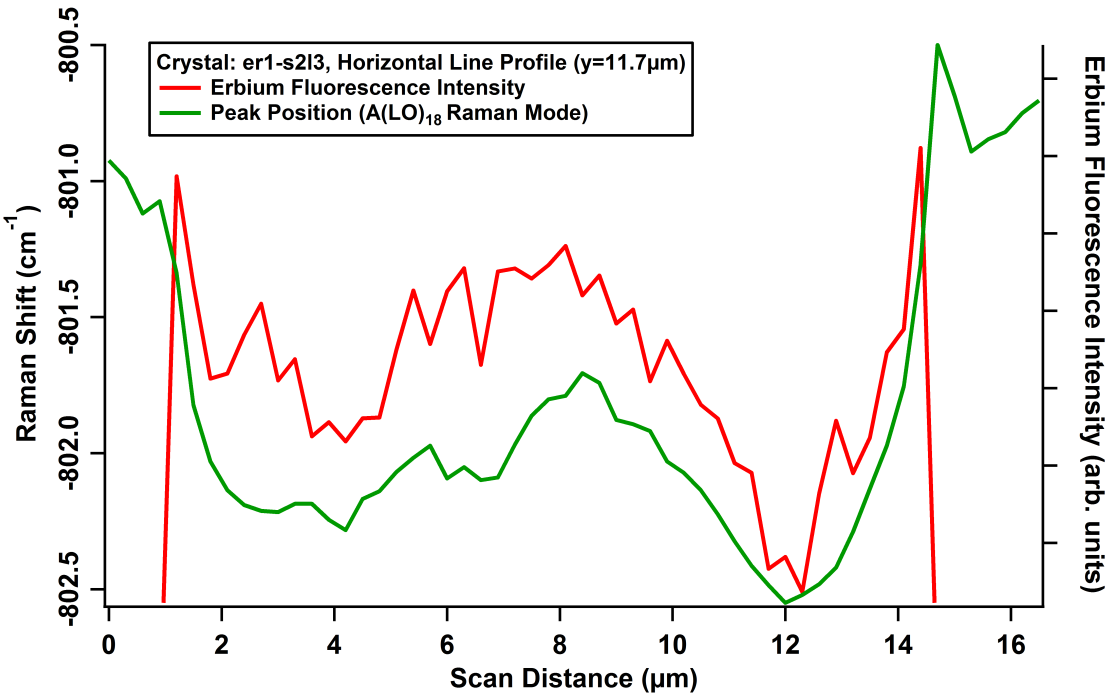

Figure 6.19: Horizontal line profiles of the erbium fluorescence intensity and peak position of the $A(LO)_{18}$ Raman mode from the cross-section of crystal er1-s2l3 illustrating the correlation between the energy of the Raman mode and the amount of erbium fluorescence emission. As the structure changes, and therefore the energy of the vibrational modes, the absorption peak of the secondary erbium site moves closer to, or farther away from, the energy of the excitation source.

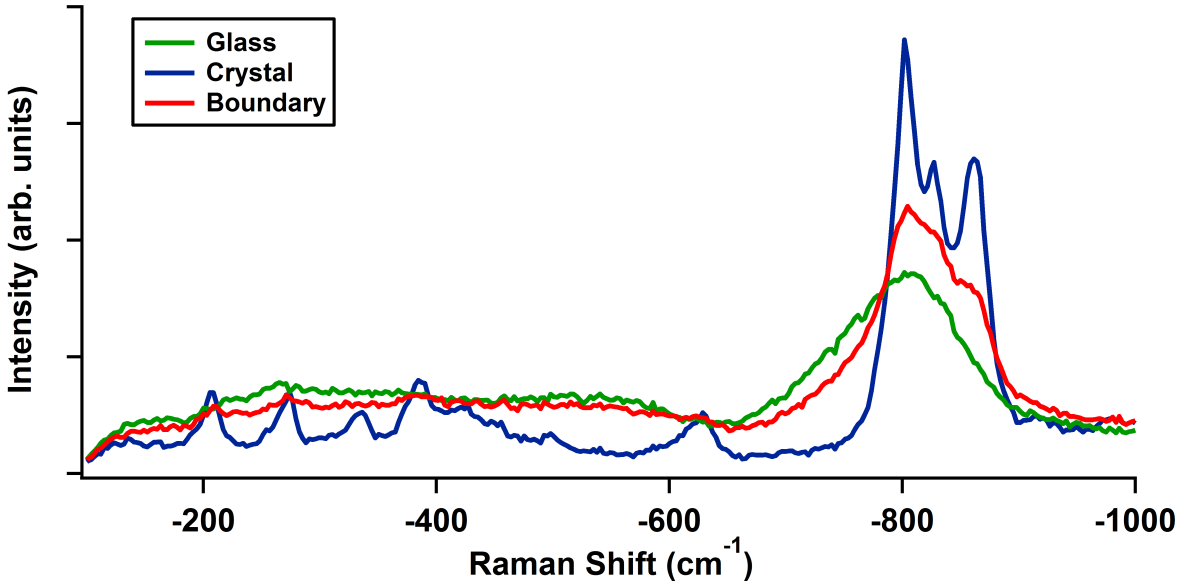

(a)

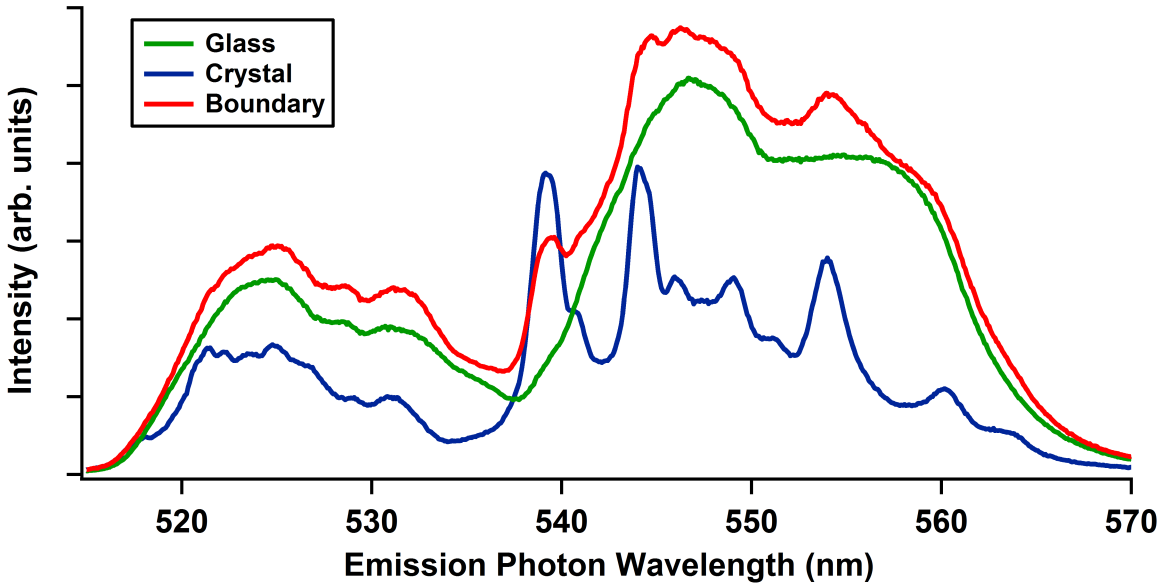

(b)

Figure 6.20: (a) Raman spectra from inside, outside, and at the glass/crystal boundary where the EFI is enhanced. The boundary spectrum is predominantly glassy in nature. (b) Erbium fluorescence spectra from the same three points as in (a). The similarity of the crystalline portion of the boundary spectrum to the nominal crystal fluorescence spectrum, combined with the enhancement, suggests that the crystal rejects erbium out into the glass.

is greater suggests an accumulation of extra erbium ions.

6.3.1 Anomalous behavior of $Er_{.002}La_{.998}BGeO_5$

At room temperature the 0.2% glass-ceramic and laser-induced crystals again present anomalous behavior. Figures 6.21 and 6.22 present the fluorescence and Raman spectra for the 0.2% glass-ceramic, as well as the corresponding spectra of the 1% glass-ceramic for comparison. The Raman spectrum of the 0.2% sample is almost identical to the higher-doped samples. On the other hand, whereas the other glass-ceramics exhibited less erbium fluorescence than their corresponding glasses, the opposite is true for the 0.2% glass-ceramic. Additionally, the shape of the fluorescence is significantly different compared to the other concentrations. Based upon the CEES results for this sample, and because the Raman spectrum matches the other compositions, this phenomenon likely confirms that the number of erbium ions occupying the secondary site is significantly greater than in other samples.

Armed with this information, it is perhaps unsurprising that the EFI from within the cross-sections of laser-induced crystals in $Er_{.002}La_{.998}BGeO_5$ glass is greater than that of the surrounding glass, as shown in Figures 6.23 and 6.24. However, in addition to this divergence from the "normal" behavior, the EFI maps, as well as the Raman maps, indicate the presence of an additional anomaly in the form of a long, narrow, filament-shaped region running vertically through the center of the crystal cross-section. Along this filament the Raman modes are shifted in energy and the EFI exhibits a slight decrease at its outer edge and a strong increase at its center.

Similar filaments were observed by Stone, and by modeling the temperature distribution during the laser irradiation process, it was determined that these regions experience temperatures which exceed the melting point of the glass (see Figure 4.11 in Stone [5]). Originally, it was thought that this region remained glassy, however, inspection of the Raman spectra reveal that it is indeed crystalline. Nevertheless, the structure within this region

is somewhat different, as at least eight new Raman modes are present in the spectra. A characteristic spectrum from this region is compared to the nominal spectrum from elsewhere in the same crystal, as well as laser-induced crystals in glasses of other compositions in Figure 6.25. The frequencies of the extra Raman modes are 288.41, 325.6, 406.44, 583.94, 714.98, 733.14, 765.77, and 787.75cm^{-1}. Of these modes, three overlap with known frequencies of $LaBGeO_5$. The 785.75cm^{-1} mode is expected for this orientation, but not typically observed. The 325.6cm^{-1} and 733.14cm^{-1} modes match modes expected in other sample orientations. The origin of the other five modes, as well as the aforementioned three if their overlap is coincidental, is unknown. The frequencies do not match those of $LaBO_3$ or LaB_2O_6 reported by Rulmont *et al.* [95] and Giesber *et al.* [96]. Neither do they match the unknown phase observed by Stone [5]. Raman spectra of other candidate phases, for example, $La_2Ge_2O_7$, could not be found in literature.

As for the behavior of the erbium fluorescence within the filament region, the origin is likely a combination of two effects. First, within the fluorescence-enhanced (above the nominal value of the non-filament portion of the crystal) part of the filament, the different structure either shifts the absorption peak of the secondary site even closer to the energy of the excitation source, or by nature includes more secondary site environments in which erbium may incorporate. Second, because the entire filament is believed to melt during the irradiation process, elemental diffusion may play a role. Whether erbium migrates outward and forms more of the primary site or migrates inward and forms more of the secondary site is unclear, though it should be noted that A. Stone [5] observed an outward migration of lanthanum.

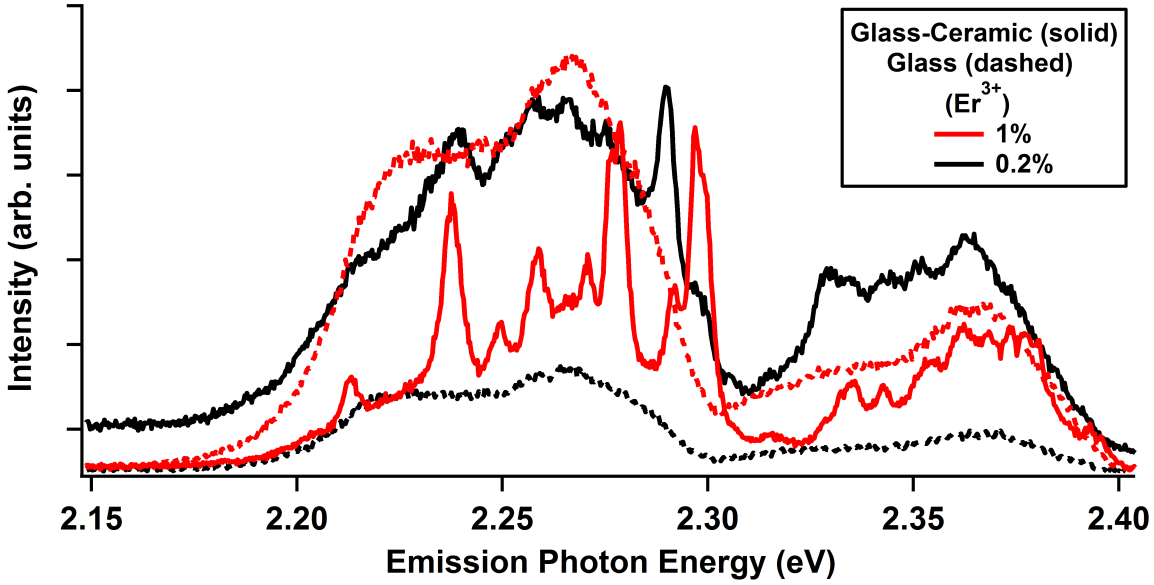

Figure 6.21: Room temperature erbium fluorescence spectra for $Er_xLa_{1-x}BGeO_5$ glass-ceramics and glasses, where x=0.002 and 0.01. The observed fluorescence corresponds to transitions from the $^4S_{3/2}$ and $^2H_{11/2}$ multiplets to the $^4I_{15/2}$ multiplet.

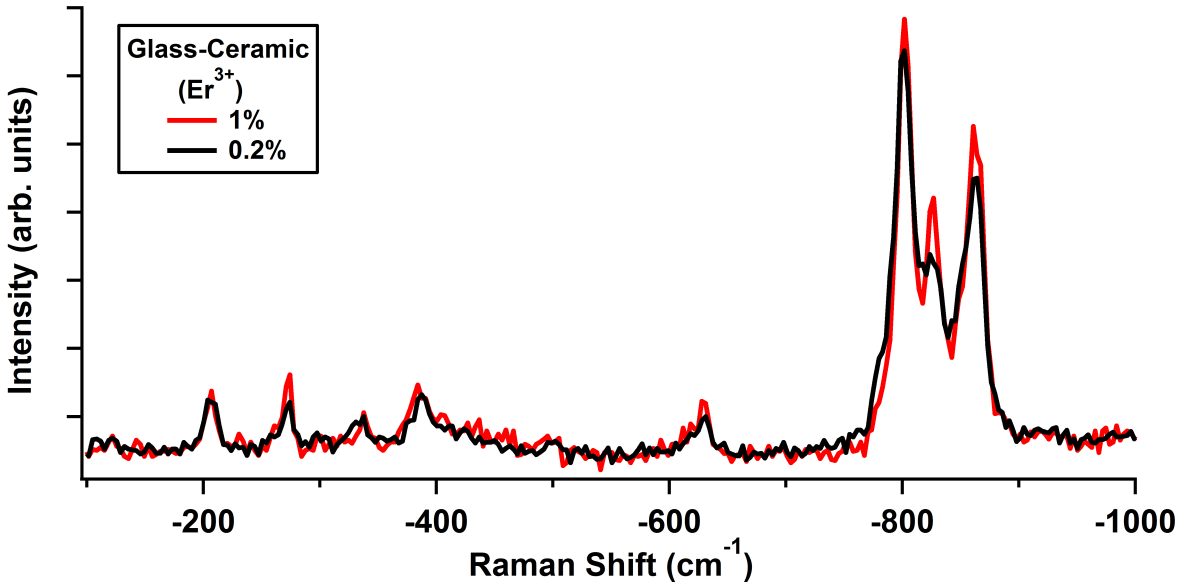

Figure 6.22: Room temperature Raman spectra for $Er_xLa_{1-x}BGeO_5$ glass-ceramics, where x=0.002 and 0.01. Unlike the more heavily doped glass-ceramics, the 0.2% glass-ceramic fluoresces more than its corresponding glass.

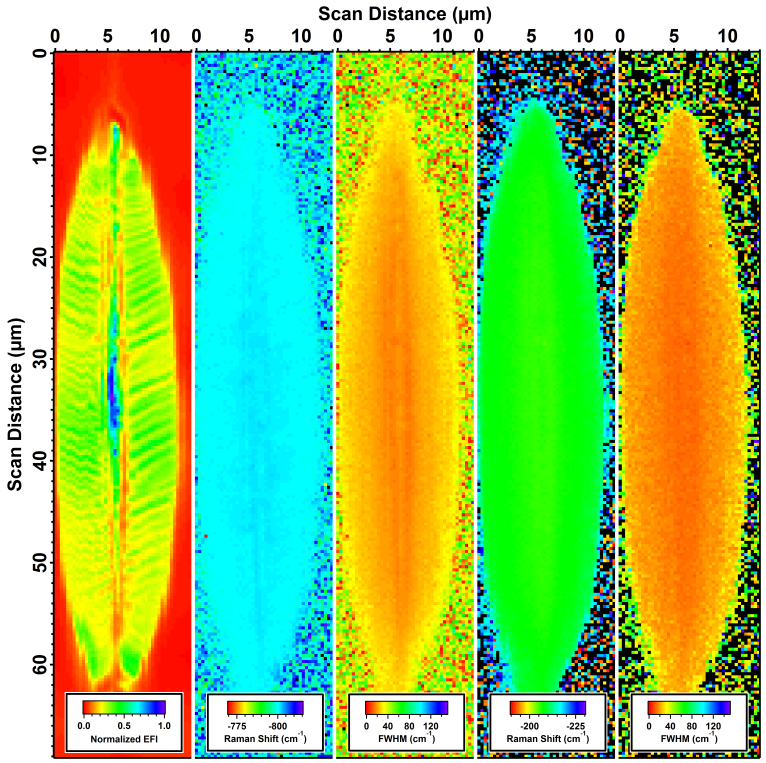

Figure 6.23: Spatially resolved maps of (L to R) erbium fluorescence intensity, $A(LO)_{18}$ peak position, $A(LO)_{18}$ FWHM, $E(TO)_6$ peak position, and $E(TO)_6$ FWHM for crystal erp2-s2l2.

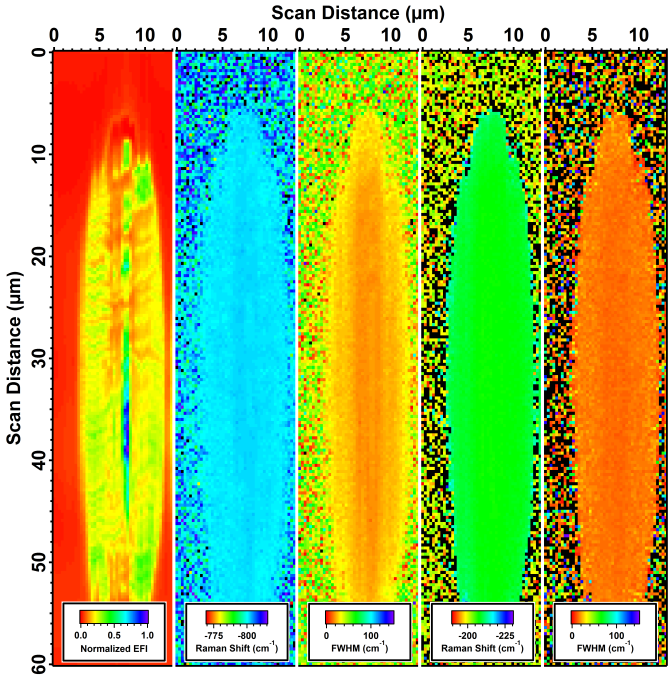

Figure 6.24: Spatially resolved maps of (L to R) erbium fluorescence intensity, $A(LO)_{18}$ peak position, $A(LO)_{18}$ FWHM, $E(TO)_6$ peak position, and $E(TO)_6$ FWHM for crystal erp2-s2l5.

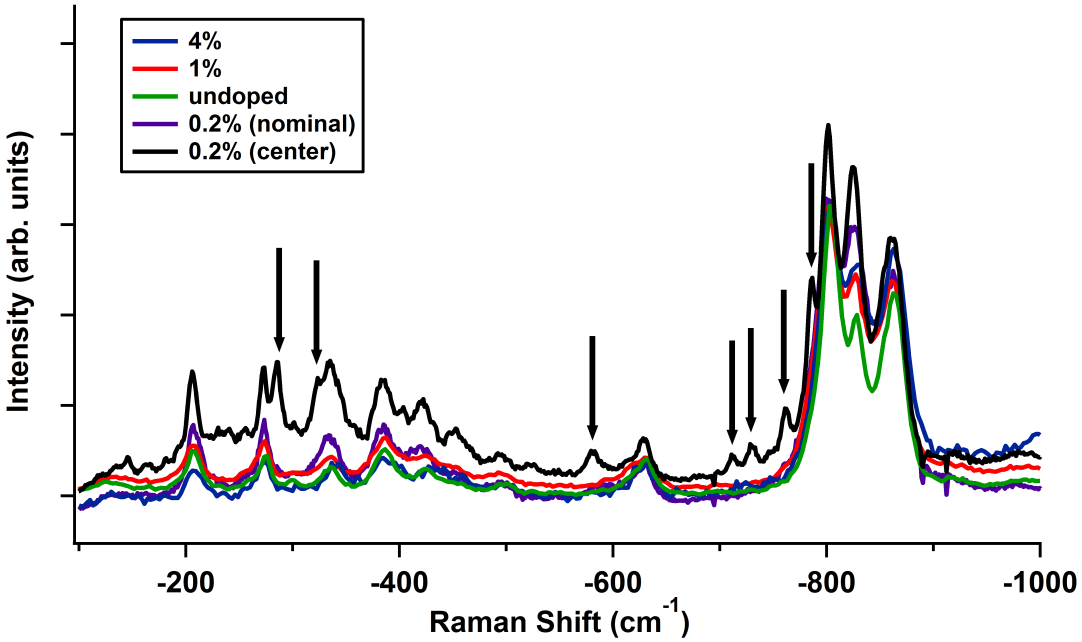

Figure 6.25: Raman spectra from the nominal portion of a laser-induced crystal in $Er_{.002}La_{.998}BGeO_5$ glass and from the anomalous central filament region exhibiting a significant erbium fluorescence enhancement. For comparison, Raman spectra from laser-induced crystals in glasses of various other compositions are also presented. The spectrum from the filament region contains at least eight new/different Raman modes which correspond to an unknown subphase of $LaBGeO_5$.

Chapter 7

Conclusions

The main overall goals of this dissertation were twofold: (1) to better understand the internal electric fields due to defects possessing local dipole moments in $LiNbO_3$ and (2) to better understand the structure and optical properties of laser-induced crystals in rare earth-doped $LaBGeO_5$ glasses.

7.1 $LiNbO_3$

In a clear manifestation of the piezoelectric effect, the Raman modes of $LiNbO_3$ were found to shift linearly with the strength of an external electric field due to an applied voltage. The slope of this response was different for different Raman modes within a particular crystal, but was consistent for a particular Raman modes in different samples, even if they varied significantly in their defect concentrations. In addition to this effect, the zero-field Raman mode frequencies following domain inversion were shifted from their original values in the as-grown state. This shift can be attributed to the presence of polar defects which create an internal electric field which does not change direction during domain inversion. The magnitude of this effect was severely underestimated by the simple model based on the coercive fields and described by Equation 4.1. Furthermore, based on the observed slope of the response of each mode, the magnitudes of their respective shifts requires an internal

electric field in excess of the coercive threshold. Because such a situation clearly cannot exist given the observed stability of ferroelectric domains in ambient conditions, the existence of additional defects with dipole moment components orthogonal to the ferroelectric axis was proposed.

The Raman modes of $LiNbO_3$ were also observed to shift in frequency due to exposure to the probe laser at lower temperature. This is attributed to the buildup of a space charge field due to photoionization of defects. During the buildup of these space charge fields, anomalous electrical breakdown was observed. The mechanism by which a discharge is initiated is yet unknown. However, discharges were not observed below a sample/defect concentration dependent threshold. Additionally, this threshold seemed to depend on whether the +c or -c surface was illuminated, and at what depth below the sample surface the illumination was focused.

7.2 $LaBGeO_5$

Erbium-doped $LaBGeO_5$ glasses and glass-ceramics were prepared, and erbium was found to incorporate within the crystal structure at predominantly one optically active site. Fluorescence from erbium incorporated at a second optically active site was also observed, though in a manner which suggests that very few erbium ions incorporate in this environment. The primary site is thought to be an unperturbed erbium ion at a lanthanum site. As $LaBGeO_5$ glass is understood to be boron deficient, the secondary site potentially consists of an erbium ion at a boron site or a boron vacancy adjacent to an erbium site, though no direct evidence exists to support these claims. A glass-ceramic with a composition of $Er_{.002}La_{.998}BGeO_5$ behaved anomalously compared to glass-ceramics with greater erbium concentrations. In this case, the fluorescence corresponding to the secondary site increased relative to that of the primary site, suggesting an increase in the relative number of er-

bium ions at the secondary site. As this glass-ceramic was prepared from a glass which pre-existed this work, this preference for a different incorporation environment can be attributed to an unknown parameter which was different during the preparation process than those used to prepare the glasses of other erbium concentrations described in Section 3.4.1.

Laser-induced crystallization was observed in $Er_{.01}La_{.99}BGeO_5$ and $Er_{.04}La_{.96}BGeO_5$ glasses. In these crystals, regardless of the irradiation conditions, erbium predominantly incorporated at the primary site, as in the glass-ceramics of corresponding composition. The irradiation conditions did, however, affect the "quality" of the resulting crystals, as the fluorescence emission was significantly broadened compared to that of the glass-ceramics. Again, the 0.2% erbium sample was anomalous, and laser-induced crystals exhibited multiple incorporation environments. Whether this can be attributed to the different host glass, or is a result of different irradiation conditions is unknown.

Room temperature Raman and fluorescence spectroscopy revealed that the structure of the glass-ceramics is unaffected by the composition and that the overall erbium fluorescence intensity is reduced in the crystal compared to the glass. On the other hand, while the structure of the $Er_{.002}La_{.998}BGeO_5$ glass-ceramic matches the other compositions, the EFI is actually greater in the crystal compared to the glass. An absorption scenario in which the absorption peak of the primary site does not overlap well with the probe laser wavelength of $488nm$, while the absorption of the secondary peak, does, is believed to be responsible. The increased number of secondary sites in the 0.2% erbium glass-ceramic thus results in a greater overall fluorescence compared to the glass, which is possible due to the much shorter radiative lifetimes in the glass-ceramic.

Spatially resolved Raman spectroscopy of laser-induced crystals-in-glass confirmed the existence of different growth zones as discussed by Stone [5], and revealed that the crystal is inhomogeneously strained across its cross-section. This strain is attributed to the strong temperature gradient during crystallization created by the femtosecond pulsed laser, as well

as the confinement of the crystal within the glass. As with $LiNbO_3$ in an external electric field, Raman mode frequencies in $LaBGeO_5$ may shift in different directions.

Similar to the glass-ceramics, the erbium fluorescence intensity within the laser-induced crystals was greater than that of the surrounding glass in the $Er_{.002}La_{.998}BGeO_5$ sample, and less in all of the other compositions. However, within the crystal cross-section, the EFI was inhomogeneous, and variations generally followed the slight shifts of the Raman mode frequencies at the same points. This implies that the strain experienced by the crystal shifts the absorption peaks of all erbium incorporation sites. Because the absorption peak of the secondary site is very close to the energy of the probe laser, small shifts result in dramatic changes in the overall EFI.

Finally, within laser-induced crystals in $Er_{.002}La_{.998}BGeO_5$ glass, a narrow filament-shaped region within the center of the crystal exhibited additional Raman modes which do not correspond to any known phase in the $LaBGeO_5$ system. Interestingly, within the region exhibiting these extra modes, the erbium fluorescence intensity was significantly greater than that of the rest of the crystal. Furthermore, this region of enhancement was immediately surrounded by a narrow area of diminished EFI, relative to the rest of the crystal. While a number of parameters which could be responsible remain hidden, temperature modeling by Stone suggests that this area of the crystal is melted during the crystallization process [5]. This melting makes elemental diffusion much easier, and, therefore, the changes in the EFI could be a result of erbium diffusion, such that the intensity is due simply to greater or less erbium, or diffusion of some other component, such as boron, which would alter which erbium site is more likely to form in a particular area.

7.3 New and Outstanding Questions

The observations and conclusions of this dissertation have provided valuable insight into the properties and behavior of the material systems studied, but have also raised new questions and left others outstanding. Therefore, future efforts should be directed toward answering the following questions:

1. What is the nature of the defect(s) in $LiNbO_3$ which have dipole moment components orthogonal to the ferroelectric axis?

2. Are the laser intensity and focal depth truly the determining parameters which influence the electrical breakdown responsible for the occasional discharging of space charge fields in $LiNbO_3$ at low temperature, and if so, what are their thresholds?

3. What is the hidden parameter which causes the ratio of the primary and secondary erbium incorporation sites in Er:$LaBGeO_5$ to change?

4. Is the strain throughout the cross-sections of laser-induced crystals tensile or compressive, and can it be controlled via the temperature profile during growth?

5. How is the laser-induced crystallization process in $LaBGeO_5$ impacted by different dopants and concentrations thereof?

6. Are laser-induced crystals-in-glass ferroelectric, or does their confinement within the glass suppress this phenomenon?

Bibliography

[1] T. Honma, "Laser-induced crystal growth of nonlinear optical crystal on glass surface", Journal of the Ceramic Society of Japan **118**, 71–76 (2010).

[2] J. D. Musgraves, K. Richardson, and H. Jain, "Laser-induced structural modification, its mechanisms, and applications in glassy optical materials", Optical Materials Express **1**, 921–935 (2011).

[3] G. Stone, Ph.D. thesis, Lehigh University, 2010.

[4] R. Shaltaf, H. Juwhari, B. Hamad, J. Khalifeh, G. Rignanese, and X. Gonze, "Structural, electronic, vibrational and dielectric properties of $LaBGeO_5$ from first principles", Journal of Applied Physics **115**, 074103 (2014).

[5] A. Stone, Ph.D. thesis, Lehigh University, 2013.

[6] C. Sandmann, Ph.D. thesis, Lehigh University, 2004.

[7] R. Weis and T. Gaylord, "Lithium niobate: Summary of physical properties and crystal structure", Applied Physics A **37**, 191–203 (1985).

[8] V. Gopalan, K. Schepler, V. Dierolf, and I. Biaggio, in *The Handbook of Photonics*, 2^{nd} ed., edited by M. Gupta and J. Ballato (CRC Press, New York, NY, 2006), Chap. 6, pp. 1–66.

[9] Y. Furukawa, K. Kitamura, E. Suzuki, and K. Niwa, "Stoichiometric $LiTaO_3$ single crystal growth by double crucible Czochralski method using automatic powder supply system", Journal of Crystal Growth **197**, 889 (1999).

[10] P. Bordui, R. Norwood, D. Jundt, and M. Fejer, "Preparation and characterization of offcongruent lithium niobate crystals", Journal of Applied Physics **71**, 875 (1992).

[11] K. Polgar, A. Peter, L. Kovács, G. Corradi, and Z. Szaller, "Growth of stoichiometric $LiNbO_3$ single crystals by top seeded solution growth method", Journal of Crystal Growth **177**, 211–216 (1997).

[12] N. Iyi, S. Kitamura, J. Imuzi, K. Yamamoto, T. Hayashi, H. Asano, and S. Kimura, "Comparitive study of defect structures in lithium niobate with different compositions", Journal of Solid State Chemistry **101**, 340–352 (1992).

[13] N. Zotov, H. Boysen, F. Frey, T. Metzger, and E. Born, "Cation substitution models of congruent $LiNbO_3$ investigated by X-ray and neutron powder diffraction", Journal of Physics and Chemistry of Solids **55**, 145–152 (1994).

[14] N. Zotov, F. Frey, H. Boysen, H. Lehnert, A. Hornsteiner, B. Strauss, R. Sonntag, H. Mayer, F. Güthoff, and D. Hohlwein, "X-ray and neutron diffuse scattering in $LiNbO_3$ from 38 to 1200 K", Acta Crystallographica Section B **51**, 961–972 (1995).

[15] H. Xu, D. Lee, J. He, S. Sinnott, V. Gopalan, V. Dierolf, and S. Phillpot, "Stability of intrinsic defects and defect clusters in $LiNbO_3$ from density functional theory calculations", Physical Review B **78**, 174103 (2008).

[16] P. Lerner, C. Legras, and J. Dumas, "Stoechiométrie des monocristaux de métaniobate de lithium", Journal of Crystal Growth **3-4**, 231–235 (1968).

[17] E. Belokoneva, W. David, J. Forsyth, and K. Knight, "Structural aspects of the $530^{\circ}C$ phase transition in $LaBGeO_5$", Journal of Physics: Condensed Matter **9**, 3503–3519 (1997).

[18] A. Kaminskii, A. Butashin, I. Maslyanizin, B. Mill, V. Mironov, S. Rozov, S. Sarkisov, and V. Shigorin, "Pure and Nd^{3+}-, Pr^{3+}-ion doped trigonal acentric $LaBGeO_5$ single crysals", Physica Status Solidi (A) **125**, 671–696 (1991).

[19] V. Sigaev, S. Stefanovich, P. Sarkisov, and E. Lopatina, "Stillwellite glass-ceramics with ferroelectric properties", Materials Science and Engineering B **32**, 17–23 (1995).

[20] V. Sigaev, A. Lotarev, E. Orlova, S. Stefanovich, P. Pernice, A. Aronna, E. Fanelli, and I. Gregora, "Lanthanum borogermanate glass-based active dielectrics", Journal of Non-Crystalline Solids **353**, 1956–1960 (2007).

[21] J. Capmany and J. G. Solé, "Second harmonic generation in $LaBGeO_5$:Nd^{3+}", Applied Physics Letters **70**, 2517–2519 (1997).

[22] S. Miyazawa, S. Ichikawa, Y. Liu, S. Ji, T. Matsuoka, and H. Nakae, "A novel substrate $LaBGeO_5$ lattice-matched to InN", Physica Status Solidi A **5**, 1195–1198 (2011).

[23] S. Stefanovich, B. Mill, and A. Butashin, "Ferroelectricity and phase transitions in stillwellite $LaBGeO_5$", Kristallografiya **37**, 965–9707 (1992).

[24] R. Pisarev and M. Serhane, "Raman scattering study of the ferroelectric $LaBGeO_5$", Fiz. Tverd. Tela **37**, 3669–3680 (1995).

[25] M. Smirnov, A. Menschikova, I. Kratochvilova-Hruba, and Z. Zikmund, "Lattice dynamics and phase transition in $LaBGeO_5$", Physica Status Solidi (B) **241**, 1017–1025 (2004).

[26] N. Horiuchi, E. Osakabe, Y. Uesu, and B. Strukov, "Nonlinear optical properties of new ferroelectric $LaBGeO_5$", Ferroelectrics **169**, 273–280 (1995).

[27] V. Sigaev, S. Stefanovich, P. Sarkisov, and E. Lopatina, "Lanthanum borogermanate glasses and crystallization of stillwellite $LaBGeO_5$: I. Specific features of synthesis and physiochemical properties of glasses", Glass Physics and Chemistry **20**, 392–397 (1994).

[28] H. Rawson, *Inorganic glass-forming systems* (Academic Press, New York, NY, 1967).

[29] L. Ivleva, I. Gorgadeze, and I. Kurdyumov, "Synthesis and crystallization of barium lanthanoborate", Izv. Akad. Nauk SSSR, Neorg. Mater. **25**, 804–807 (1989).

[30] Y. Takahashi, Y. Benino, T. Fujiwara, and T. Komatsu, "Second harmonic generation in transparent surface crystallized glasses with stillwellite-type $LaBGeO_5$", Journal of Applied Physics **89**, 5282–5287 (2001).

[31] J. Capmany, D. Jaque, J. G. Solé, and A. Kaminskii, "Continuous wave laser radiation at 524nm from a self-frequency-doubled laser of $LaBGeO_5$:Nd^{3+}", Applied Physics Letters **72**, 531–533 (1998).

[32] A. Antic-Fidancev, K. Serhan, M. Taibi, M. Lemaitre-Blaise, P. Porcher, J. Aride, and A. Boukhari, "The optical properties of Eu^{3+} embedded in the rare earth borogermanate matrix: $REBGeO_5$", Journal of Physics: Condensed Matter **6**, 6857–6864 (1994).

[33] A. Rulmont and P. Tarte, "Lanthanide borogermanates $Ln$$BGeO_5$: Synthesis and structural study by X-ray diffractometry and vibrational spectroscopy", Journal of Solid State Chemistry **75**, 244–250 (1988).

[34] S. Zhang, G. Wu, C. Duan, and J. Wang, "Novel phosphors of Eu^{3+}, Tb^{3+} or Tm^{3+} activated $LaBGeO_5$", Journal of Rare Earths **29**, 737–740 (2011).

[35] G. Malashkevich, V. Sigaev, N. Golubev, V. Savinkov, P. Sarkisov, I. Khodasevich, V. Dashkevich, and A. Mudryi, "Luminescence of borogermanate glasses activated by Er^{3+} and Yb^{3+} ions", Journal of Non-Crystalline Solids **357**, 67–72 (2011).

[36] I. Lewis and H. Edwards, *Handbook of Raman Spectroscopy: From the Research Laboratory to the Process Line* (CRC Press, New York, NY, 2001).

[37] D. Long, *The Raman Effect: A Unified Treatment of the Theory of Raman Scattering by Molecules* (John Wiley and Sons, LTD, New York, NY, 2002).

[38] R. Loudon, "The Raman effect in crystals", Advances in Physics **50**, 813–864 (2001).

[39] H. Bowley, D. Gardiner, D. Gerrard, P. Graves, J. Louden, and G. Turrell, *Practical Raman Spectroscopy* (Springer-Verlag, New York, NY, 1989).

[40] I. Hrubá, S. Kamba, J. Ptzelt, I. Gregora, Z. Zikmund, D. Ivannikov, G. Komandin, A. Volkov, and B. Strukov, "Optical phonons and ferroelectric phase transition in the $LaBGeO_5$ crystal", Phys. Stat. Sol. (B) **214**, 423–439 (1999).

[41] R. Sato, Y. Benino, T. Fujiwara, and T. Komatsu, "YAG laser-induced crystalline dot patterning in samarium tellurite glasses", Journal of Non-Crystalline Solids **289**, 228–232 (2001).

[42] T. Honma, Y. Benino, T. Fujiwara, and t. Komatsu, "Nonlinear optical crystal-line writing in glass by yttrium aluminum garnet laser irradiation", Applied Physics Letters **82**, 892–894 (2003).

[43] T. Honma, Y. Benino, T. Fujiwara, and T. Komatsu, "Transition metal atom heat processing for writing of crystal lines in glass", Applied Physics Letters **88**, 231105 (2006).

[44] M. Abe, Y. Benino, T. Fujiwara, and T. Komatsu, "Writing of nonlinear optical $Sm_2(MoO_4)_3$ crystal lines at the surface of glass by samarium atom heat processing", Jounrnal of Applied Physics **97**, 123516 (2005).

[45] R. Dongol, L. Tweeton, C. Faris, S. Feller, and M. Affatigato, "Mechanisms of laser induced modification of lead and barium vanadate glasses", Journal of Applied Physics **109**, 013521 (2011).

[46] X. Feng, J. Shi, C. Huang, P. Horak, P. Teh, S. Alam, M. Ibsen, and W. Loh, "Laser-induced crystalline optical waveguide in glass fiber format", Optics Express **20**, B85–B93 (2012).

[47] B. Franta, T. Williams, C. Faris, S. Feller, and M. Affatigato, "Laser induced modification of vanadate glasses", Physics and Chemistry of Glasses: European Journal of Glass Science and Technology Part B **48**, 357–362 (2007).

[48] P. Gupta, H. Jain, D. Williams, J. Toulouse, and I. Veltchev, "Creation of tailored features by laser heating of $Nd_{0.2}La_{0.8}BGeO_5$", Optical Materials **29**, 355–359 (2006).

[49] P. Gupta, H. Jain, D. Williams, T. Honma, Y. Benino, and T. Komatsu, "Creation of ferroelectric, single-crystal architecture in $Sm_{0.2}La_{0.8}BGeO_5$ glass", Journal of the American Ceramic Society **91**, 110–114 (2008).

[50] P. Gupta, A. Stone, N. Woodward, V. Dierolf, and H. Jain, "Laser fabrication of semiconducting ferroelectric single crystal SbSI features on chalcohalide glass", Optical Materials Express **1**, 652–657 (2011).

[51] T. Honma, Y. Benino, T. Fujiwara, and T. Komatsu, "Technique for writing of non-linear optical single-crystal lines in glass", Applied Physics Letters **83**, 2796–2798 (2003).

[52] T. Honma, K. Koshiba, Y. Benino, and T. Komatsu, "Writing of crystal lines and its optical properties of rare-earth ion (Er^{3+} and Sm^{3+}) doped lithium niobate crystal on glass surface formed by laser irradiation", Optical Materials **31**, 8315–319 (2008).

[53] T. Honma, T. Komatsu, D. Zhao, and H. Jain, "Writing of rare-earth ion doped lithium niobate line patterns in glass by laser scanning", IOP Conference Series: Materials Science and Engineering **1**, 012006 (2009).

[54] T. Honma, P. Nguyen, and T. Komatsu, "Crystal growth behavior in CuO-doped lithium disilicate glasses by continuous-wave fiber laser irradiation", Journal of the Ceramic Society of Japan **115**, 1314–1318 (2008).

[55] T. Honma, N. Hirokawa, and T. Komatsu, "Micro-architecture of nonlinear optical $Ba_2TiGe_2O_8$ crystal dots and lines on the surface of laser-induced crystallized glasses by chemical etching", Applied Surface Science **255**, 3126–3131 (2008).

[56] T. Honma and T. Komatsu, "Patterning of two-dimensional plana lithium niobate architectures on glass surface by laser scanning", Optics Express **18**, 8019–8024 (2010).

[57] R. Ihara, T. Honma, Y. Benino, T. Fujiwara, R. Sato, and T. Komatsu, "Writing of two-dimensional crystal curved lines at the surface of Sm_2O_3-Bi_2O_3-B_2O_3 glass by samarium atom heat processing", Solid State Communications **136**, 273–277 (2005).

[58] S. Kawasaki, T. Honma, Y. Benino, T. Fujiwara, R. Sato, and T. Komatsu, "Writing of crystal-dots and lines by YAG laser irradiation and their morphologies in samarium tellurite glasses", Journal of Non-Crystalline Solids **325**, 61–69 (2003).

[59] T. Komatsu, S. Kawasaki, T. Honma, Y. Benino, T. Fujiwara, and R. Sato, "Writing of crystalline dots and lines in Sm_2O_3 doped borate and tellurite glasses by YAG laser irradiation and their optical properties", Physics and Chemistry of Glasses **45**, 75–78 (2004).

[60] T. Komatsu, K. Koshiba, and T. Honma, "Preferential growth orientation of laser-patterned $LiNbO_3$ crystals in lithium niobium silicate glass", Journal of Solid State Chemistry **184**, 411–418 (2011).

[61] T. Komatsu, T. Honma, Y. Benino, and T. Komatsu, "Patterning and morphology of nonlinear optical $Gd_xBi_{1-x}BO_3$ crystals in CuO-doped glass by YAG laser irradiation", Applied Physics A **89**, 981–986 (2007).

[62] D. Savytskii, M. Sanders, R. Golovchak, B. Knorr, V. Dierolf, and H. Jain, "Crystallization of stoichiometric SbSI glass", Journal of the American Ceramic Society **97**, 198–205 (2013).

[63] H. Sugita, T. Honma, Y. Benino, and T. Komatsu, "Formation of $LiNbO_3$ crystals at the surface of TeO_2-based glass by YAG laser-induced crystallization", Solid State Communications **143**, 280–284 (2007).

[64] F. Suzuki, T. Honma, and T. Komatsu, "Laser patterning and morphology of two-dimensional planar ferroelastic rare-earth molybdate crystals on the glass surface", Materials Chemistry and Physics **125**, 377–381 (2011).

[65] E. Glezer, M. Milosavljevic, L. Huang, R. Finlay, T. Her, J. Callan, and E. Mazur, "Three-dimensional optical storage inside transparent materials", Optics Letters **24**, 2023–2025 (1996).

[66] K. Davis, K. Miura, N. Sugimoto, and K. Hirao, "Writing waveguides in glass with a femtosecond laser", Optics Letters **21**, 1729–1731 (1996).

[67] K. Hirao and K. Miura, "Writing waveguides and gratings in silica and related materials by a femtosecond laser", Journal of Non-Crystalline Solids **239**, 91–95 (1998).

[68] A. Stone, H. Jain, V. Dierolf, M. Sakakura, Y. Shimotsuma, K. Miura, and K. Hirao, "Multilayer aberration correction for depth-independent three-dimensional crystal growth in glass by femtosecond laser heating", Journal of the Optical Society of America B **30**, 1234–1240 (2013).

[69] K. Miura, J. Qiu, T. Mitsuyu, and K. Hirao, "Space-selective growth of frequency-conversion crystals in glasses with ultrashort infrared laser pulses", Optics Letters **25**, 408–410 (2000).

[70] T. Komatsu, R. Ihara, T. Honma, Y. Benino, R. Sato, H. Kim, and T. Fujiwara, "Patterning of non-linear optical crystals in glass by laser-induced crystallization", Journal of the American Ceramic Society **90**, 699–705 (2007).

[71] Y. Dai, B. Zhu, J. Qiu, B. Ma, H. an Lu, S. Cao, and B. Yu, "Direct writing three-dimensional $Ba_2TiSi_2O_8$ crystalline pattern in glass with ultrashort pulse laser", Applied Physics Letters **90**, 181109 (2007).

[72] Y. Dai, B. Zhu, J. Qiu, B. Ma, H. an Lu, and B. Yu, "Space-selective precipitation of functional crystals in glass by using a high repetition rate femtosecond laser", Chemical Physics Letters **443**, 1253–257 (2007).

[73] Y. Dai, B. Ma, H. an Lu, B. Yu, B. Zhu, and J. Qiu, "Femtosecond laser-induced oriented precipitation of $Ba_2TiGe_2O_8$", Optics Express **16**, 3912–3917 (2008).

[74] B. Fisette, F. Busque, J. Degorce, and M. Meunier, "Three-dimensional crystallization inside phtosensitive glasses by femtosecond laser", Applied Physics Letters **88**, 091104 (2006).

[75] B. Lu, B. Yu, B. Chen, X. Yan, J. Qiu, X. Jiang, and C. Zhu, "Study of crystal formation in titanate glass irradiated by 800nm femtosecond laser pulse", Journal of Crystal Growth **285**, 76–80 (2005).

[76] A. Stone, M. Sakakura, Y. Shimotsuma, K. Miura, K. Hirao, V. Dierolf, and H. Jain, "Unexpected influence of focal depth on nucleation during femtosecond laser crystallization of glass", Optical Materials Express **1**, 990–995 (2011).

[77] Y. Yonesaki, K. Miura, R. Araki, K. Fujita, and K. Hirao, "space-selective precipitation of non-linear optical crystal inside silicate glasses using near-infrared femtosecond laser", Journal of Non-Crystalline Solids **351**, 885–892 (2005).

[78] B. Zhu, Y. Dai, M. H., S. Zhang, G. Lin, and J. Qiu, "Femtosecond laser induced space-selective precipitation of nonlinear optical crystals in rare-earth-doped glasses", Optics Express **15**, 6069–6074 (2007).

[79] A. Stone, M. Sakakura, Y. Shimotsuma, G. Stone, P. Gupta, K. Miura, K. Hirao, V. Dierolf, and H. Jain, "Directionally controlled 3D ferroelectric single crsytal growth in $LaBGeO_5$ glass by femtosecond laser irradiation", Optics Express **17**, 23284–23289 (2009).

[80] A. Stone, M. Sakakura, Y. Shimotsuma, G. Stone, P. Gupta, K. Miura, K. Hirao, V. Dierolf, and H. Jain, "Formation of ferroelectric single-crystal architectures in $LaBGeO_5$ glass by femtosecond vs. continuous-wave lasers", Journal of Non-Crystalline Solids **356**, 3059–3065 (2010).

[81] V. Sigaev, E. Alieva, S. Loarev, N. Lepekhin, Y. Priseko, and A. Rasstanaev, "Local crystallization of glasses in the La_2O_3-B_2O_3-GeO_2 system under laser irradiation", Glass Physics and Chemistry **35**, 13–20 (2009).

[82] M. Sakakura, M. Terazima, "Oscillation of the refractive index at the focal region of a femtosecond laser pulse inside a glass", Optics Letters **29**, 1548–1550 (2004).

[83] S. Sundaram, C. Schaffer, and E. Mazur, "Microexplosions in tellurite glasses", Applied Physics A **76**, 379–384 (2003).

[84] M. Shimizu, M. Sakakura, S. Kanehira, M. Nishi, Y. Shimotsuma, K. Hirao, and K. Miura, "Formation mechnism of element distribution in glass under femtosecond laser irradiation", Optics Letters **836**, 2161–2163 (2011).

[85] M. Sakakura, T. Tochio, M. Shimizu, N. Yasuda, M. Ohnish, K. Miura, Y. Shimotsuma, and K. Hirao, "Control of material properties by parallel laser irradiations at multiple laser spots using a spatial light modulator", Proceedings of SPIE **8243**, 824310 (2012).

[86] E. Abbe, "Beiträge zur Theorie der Microscopie und der Microscopischen Wahrnehmung", Arch. Mikrosk. Anat. **9**, 413–468 (1873).

[87] L. Novotny and B. Hecht, *Principles of Nano-Optics* (Cambridge University Press, New York, NY, 2007).

[88] V. Gopalan, V. Dierolf, and D. Scrymgeour, "Defect-domain wall interactions in trigonal ferroelectrics", Annual Review of Materials Research **37**, 449–489 (2007).

[89] V. Dierolf, A. Kutsenko, C. Sandmann, T. Tröster, and G. Corradi, "High resolution site selective optical spectroscopy of rare earth and transition metal defects in insulators", Journal of Luminescence **87-89**, 989 (2000).

[90] V. Dierolf, T. Morgus, C. Sandmann, E. Cantelar, F. Cusso, P. Capek, J. Spirkova, K. Polgar, W. Sohler, and A. Ostendorf, "Comparative studies of Er^{3+} ions in $LiNbO_3$

waveguides produced by different methods", Radiation Effects and Defects in Solids **158**, 263 (2003).

[91] G. Stone, B. Knorr, V. Gopalan, and V. Dierolf, "Frequency shift of Raman modes due to an applied electric field and domain inversion in $LiNbO_3$", Physical Review B **84**, 134303 (2011).

[92] B. Mitchell, Ph.D. thesis, Lehigh University, 2014.

[93] N. Woodward, Ph.D. thesis, Lehigh University, 2011.

[94] C. Coussa, C. Martinet, B. Champagnon, L. Grosvalet, D. Vouagner, and V. Sigaev, "*In situ* Raman spectroscopy of pressure-induced changes in $LaBGeO_5$ glass: hysteresis and plastic deformation", Journal of Physics: Condensed Matter **19**, 266220 (2007).

[95] A. Rulmont, J. Flamme, M. Pottier, and B. Wanklyn, "Birefringence effect in the raman spectrum of a crystal which is not cut parallel to the principle axes - II. application to a single crystal of $LaBO_3$", Spectrochemica Acta Part A: Molecular Spectroscopy **35**, 635–639 (1979).

[96] H. Giesber, J. Ballato, G. Chumanov, J. Kolis, and M. Dejneka, "Spectroscopic properties of Er^{3+} and Eu^{3+} doped acentric $LaBO_3$ and $GdBO_3$", Journal of Applied Physics **93**, 8987–8994 (2003).

[97] D. Savytskii, B. Knorr, V. Dierolf, and H. Jain, "Challenges of CW laser-induced crystallization in a chalcogenide glass", Optical Materials Express **3**, 1026–1038 (2013).

[98] D. Savytskii, B. Knorr, V. Dierolf, and H. Jain, "Formation of laser-induced SbSI single crystal architecture in Sb-S-I glasses", Journal of Non-Crystalline Solids **377**, 245–249 (2013).

Appendix A

Laser-induced Crystal Nucleation and Growth Conditions

The conditions under which crystal nucleation was achieved in the various rare earth-doped $LaBGeO_5$ glasses prepared in this work were random and inconsistent. From the work of Stone, it is known that increased spherical aberration may create better nucleation conditions [5]. For this reason, a standard slide glass was sometimes placed between the microscope objective and the sample. Additionally, the modification to the glass produced at the laser focus would frequently reach an equilibrium, after which continued irradiation would fail to result in any changes. On the theory that this initial irradiation may have produced potential nucleation sites which were simply at the wrong temperature, the laser power or focal position were sometimes abruptly changed in order to stimulate further modification. The details of the conditions which successfully nucleated crystals are recounted in Table A.1. It should be noted that the laser powers listed in Table A.1, as well as Table A.2, refer to the measured value immediately following the graduated neutral density filter shown in Figure 3.6. The measured power immediately before the microscope objective was 83% of these reported values.

Once a seed crystal had been nucleated in a particular glass, the irradiation conditions which could be used to grow this crystal became much more flexible. A large area of this

parameter space was explored, and many crystals were grown in each of the glasses in which nucleation was achieved. Of these, a few were selected for study in this dissertation, and the conditions used to grow these crystals, as well as the names by which they are referred, are listed in Table A.2.

Table A.1: Conditions which resulted in laser-induced crystal nucleation in various rare earth-doped $LaBGeO_5$ glasses. All samples were at room temperature during laser irradiation.

Sample	**Power (mW)**	**Focal Depth (μm)**	**Cover Slide**	**Notes**
$Er_{.01}La_{.99}BGeO_5$	700	600	N	ramp down power to 640mW
$Er_{.04}La_{.96}BGeO_5$	750	600	N	move sample $5\mu m$ lateral, ramp power down then up to 850mW
$Er_{.10}La_{.90}BGeO_5$	-	-	-	no crystal nucleation observed
$Er_{.20}La_{.80}BGeO_5$	-	-	-	no crystal nucleation observed
$Nd_{.002}La_{.998}BGeO_5$	700	600	N	
$Nd_{.01}La_{.99}BGeO_5$	850	550	N	
$Nd_{.04}La_{.96}BGeO_5$	800	75	Y	ramp power up to 850mW
$Nd_{.10}La_{.90}BGeO_5$	850	75	Y	move sample $4\mu m$ down
$Nd_{.20}La_{.80}BGeO_5$	860	125	Y	
$Pr_{.002}La_{.998}BGeO_5$	650	600	N	move sample $4\mu m$ down, ramp power up to 760mW
$Pr_{.01}La_{.99}BGeO_5$	650	600	N	move sample $4\mu m$ down, ramp power up to 810mW
$Pr_{.04}La_{.96}BGeO_5$	650	600	N	move sample $4\mu m$ down, ramp power up to 750mW
$Pr_{.10}La_{.90}BGeO_5$	-	-	-	no attempt made
$Pr_{.20}La_{.80}BGeO_5$		-	-	no attempt made

Table A.2: Growth conditions for different laser-induced crystalline lines studied in this work. All samples were externally heated to 500°C during laser irradiation.

Name	**Sample**	**Power (mW)**	**Write Speed** $\mu m/s$	**Focal Depth** μm	**Aberration Corrected**
udc-s1l2	$LaBGeO_5$	300	44	500	Y
udc-s1l5	$LaBGeO_5$	300	44	500	Y
erp2-s2l5	$Er_{.002}La_{.998}BGeO_5$	na	20	na	N
erp2-s2l2	$Er_{.002}La_{.998}BGeO_5$	na	30	na	N
er1-s1l2	$Er_{.01}La_{.99}BGeO_5$	750	15	1200	N
er1-s1l5	$Er_{.01}La_{.99}BGeO_5$	600	15	1200	N
er1-s1l6	$Er_{.01}La_{.99}BGeO_5$	750	15	600	N
er1-s1l7	$Er_{.01}La_{.99}BGeO_5$	750	15	600	N
er1-s1l9	$Er_{.01}La_{.99}BGeO_5$	600	15	600	N
er1-s2l1	$Er_{.01}La_{.99}BGeO_5$	400	15	600	Y
er1-s2l3	$Er_{.01}La_{.99}BGeO_5$	400	10	600	Y
er1-s2l13	$Er_{.01}La_{.99}BGeO_5$	400	10	1200	Y
er4-s1l2	$Er_{.04}La_{.96}BGeO_5$	750	10	1200	N
er4-s1l6	$Er_{.04}La_{.96}BGeO_5$	750	10	600	N
er4-s2l1	$Er_{.04}La_{.96}BGeO_5$	400	10	1200	Y
er4-s2l5	$Er_{.04}La_{.96}BGeO_5$	400	10	600	Y

Appendix B

Additional $LaBGeO_5$ Data

In addition to the data already presented, additional data which did not fit elsewhere is presented in this appendix. Figures B.1 and B.2 present optical images of two selected laser induced crystals next to their respective Raman maps for comparison.

Table B.1 contains the results of wavelength dispersive spectroscopy (WDS) measurements performed on 0.2%, 1%, and 4% Er:$LaBGeO_5$ glasses. To perform this technique a Ge metal and LaB_6 crystal were used as standards. Unfortunately, no standard containing erbium was available. For this reason, two sets of data are presented: the as-collected data without considering erbium, and modified data in which the nominal erbium concentration was input as a set fraction of the detected amounts of oxygen. The accelerating voltage was $8kV$, the current was $15nA$, the exposure time was $60s$, and data were collected from 10 different locations per sample. The characteristic x-rays used were the Ge Lα, B Kα, and La Lα. Of the $60s$ exposure time, $40s$ were spent on the peak, and $10s$ were spent on each side of the peak. The samples were carbon-coated to reduce charging effects. In addition to the measured data, ratios of boron to the other elements were calculated. As discussed in the previous chapters, the 0.2% sample seems to contain relatively less boron.

Figure B.3 presents Raman spectra collected from Nd:$LaBGeO_5$ glass-ceramics with various concentrations of neodymium. Similarly, Figure B.4 presents room temperature

fluorescence spectra collected from Pr:$LaBGeO_5$ glass-ceramics with various concentrations of praseodymium.

Finally, topographic images collected using an interferometer of the endfaces of samples undoped and 1% Er $LaBGeO_5$ glasses contained laser-induced crystal are shown in Figures B.5 and B.6, respectively. Despite thorough polishing, the crystals appear to protrude from the surface of the glass. Whether this is an indication of differing abrasion rates between the glass and crystal, related to relief of longitudinal strain due to the confinement within the glass, or an artifact of the measurement technique is unknown.

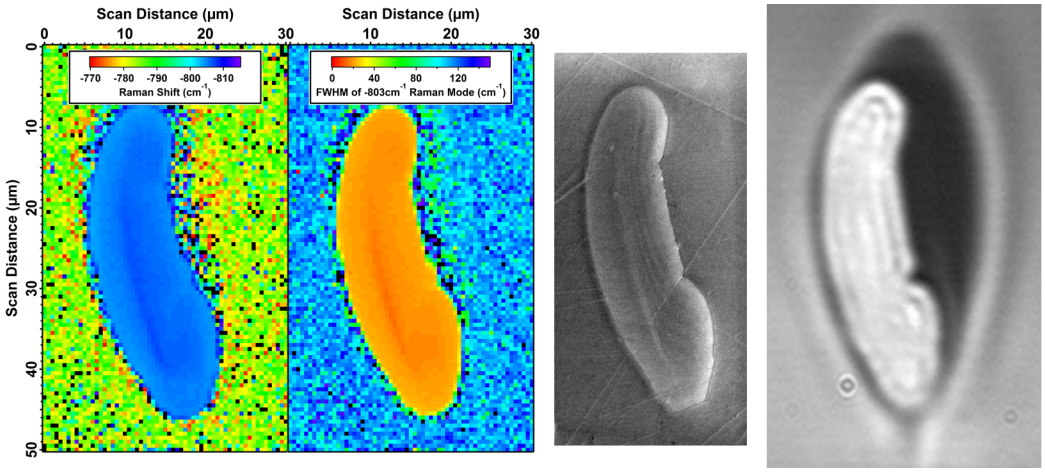

Figure B.1: Images of udc-s1l2. L to R: Map of peak position of the $A(LO)_{18}$ Raman mode, map of the FWHM of the $A(LO)_{18}$ Raman mode, charge contrast image in variable-pressure SEM (reproduced from Stone [5], and a standard optical image (reproduced from Stone [5].

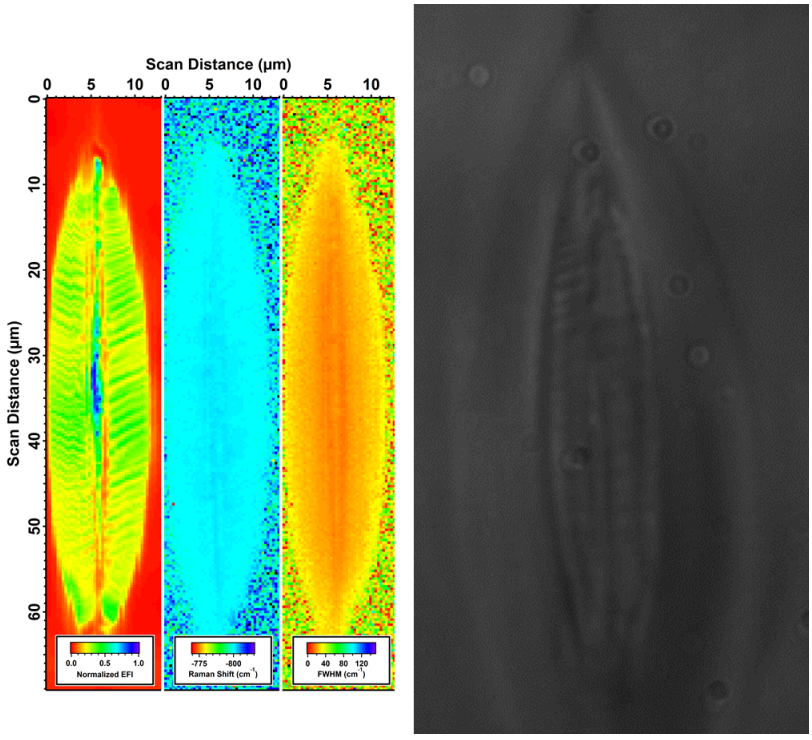

Figure B.2: Images of erp2-s2l2. L to R: Map of total integrated EFI, map of peak position of the $A(LO)_{18}$ Raman mode, map of the FWHM of the $A(LO)_{18}$ Raman mode, and a standard optical image (reproduced from Stone [5].

Table B.1: WDS data for Er:$LaBGeO_5$ glasses showing that the 0.2% sample is boron deficient.

Sample	**Ge AT%**	**B AT%**	**La AT%**	**Er AT%**	**O AT%**	**TOTAL**	**Ge %ERR**	**B %ERR**	**La %ERR**	**B/(La+Er)**	**B/Ge**	**B/O**
0.2%	12.06	11.16	14.18	0.19	62.41	100.00	0.88	1.31	2.36	0.78	0.93	0.18
1%	11.47	12.85	12.37	1.02	62.29	100.00	0.88	1.23	2.53	0.96	1.12	0.21
4%	10.17	13.25	10.96	3.59	62.03	100.00	0.88	1.18	2.62	0.91	1.30	0.21
0.2%	12.15	11.16	14.26	0.00	62.43	100.00	0.88	1.31	2.36	0.78	0.92	0.18
1%	11.96	12.87	12.77	0.00	62.39	100.00	0.88	1.23	2.53	1.01	1.08	0.21
4%	11.84	13.46	12.34	0.00	62.37	100.00	0.88	1.18	2.62	1.09	1.14	0.22

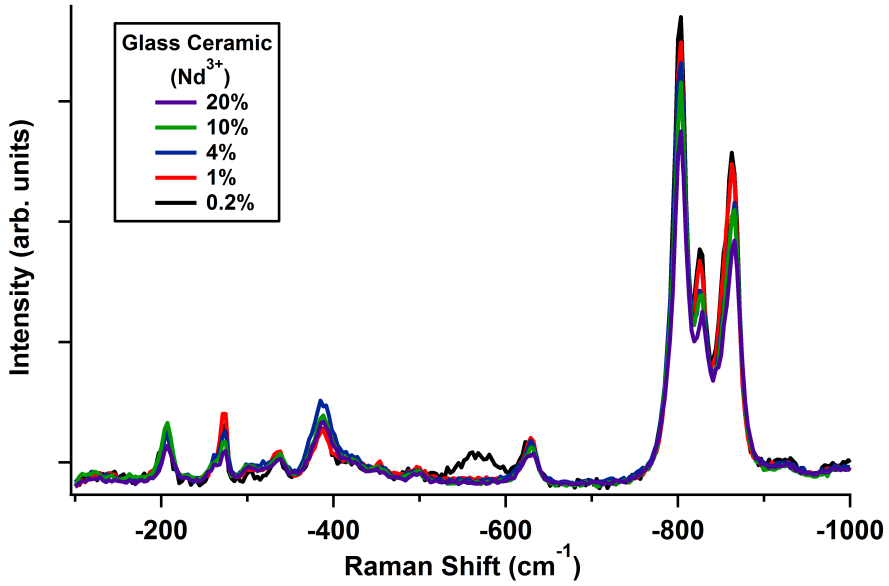

Figure B.3: Raman spectra collected from $Nd_xLa_{1-x}BGeO_5$ glass-ceramics, with x=0.002, 0.01, 0.04, 0.10, 0.20.

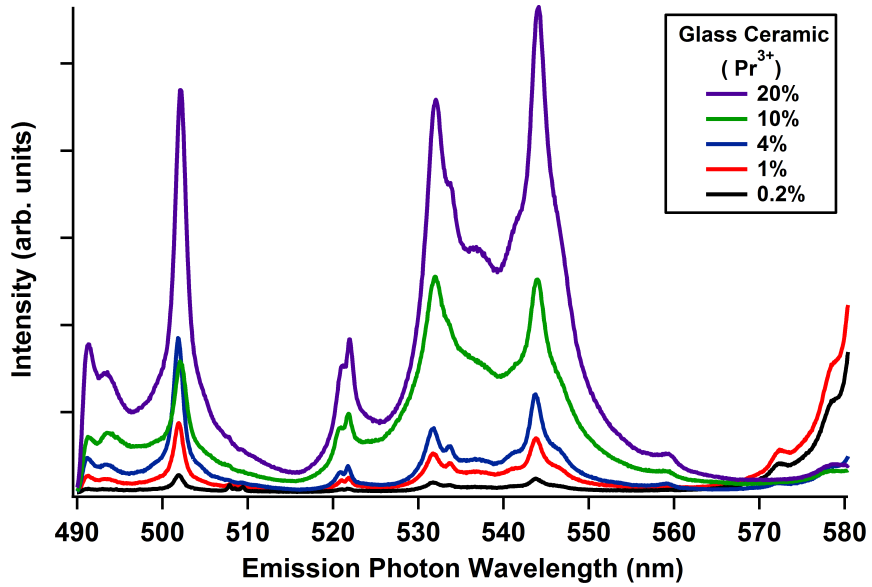

Figure B.4: room temperature fluorescence spectra collected from $Pr_xLa_{1-x}BGeO_5$ glass-ceramics, with x=0.002, 0.01, 0.04, 0.10, 0.20.

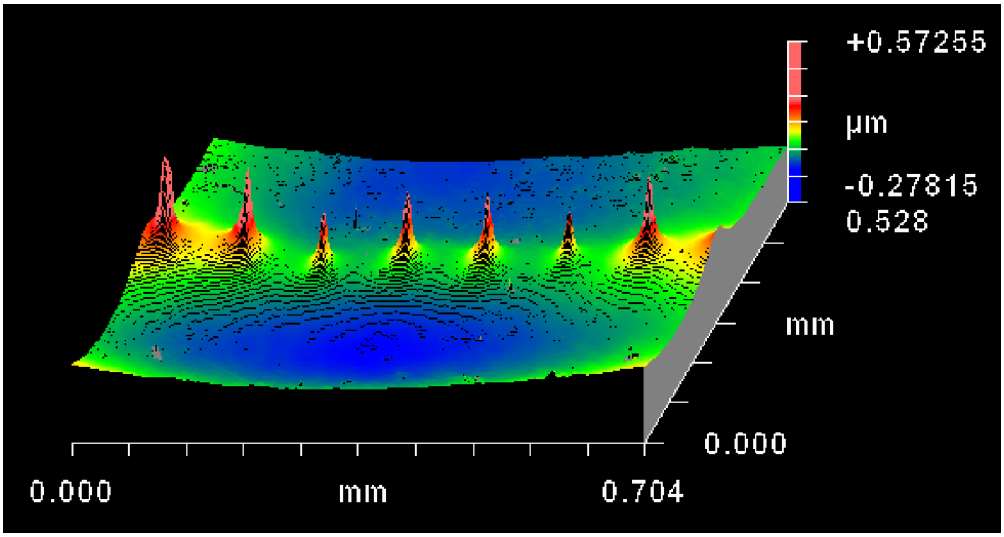

Figure B.5: Topographic image of the endface of the undoped $LaBGeO_5$ glass containing laser-induced crystals. Image courtesy of Keith Veenhuizen.

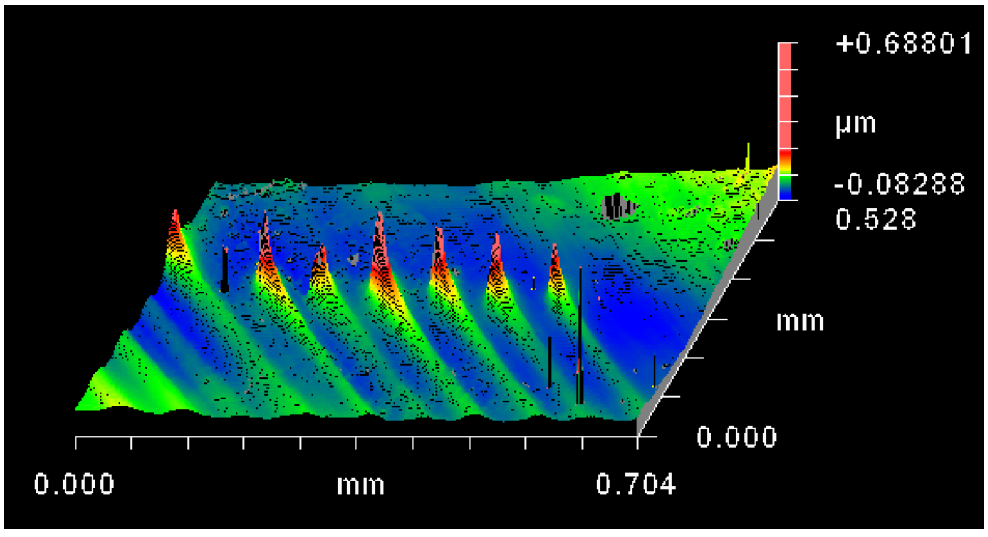

Figure B.6: Topographic image of the endface of the 1% Er doped $LaBGeO_5$ glass containing laser-induced crystals. Image courtesy of Keith Veenhuizen.

Appendix C

CW Laser-induced Crystallization of SbSI

A significant amount of work was performed in designing, constructing, and utilizing a setup for CW laser-induced crystallization of SbSI glass. The results of this work are described by Savytskii *et al.* [62, 97, 98].

Figure C.1 illustrates the CW laser crystallization setup. A laser diode operating at $785nm$ is coupled into a single mode fiber and brought to the microscope. Additionally, single mode fiber-pigtailed laser diodes operating at $514nm$ and $637nm$ are brought to the microscope and combined by a beamsplitter. These lasers can be used individually, or at the same time. Two different dichroic mirrors are used to direct the beams from all three laser diodes through a 50:50 beamsplitter and into a 50x/0.75NA microscope objective. The beamsplitter allows a white light source to also be directed through the objective. A CCD camera is used to observe the reflected white light and monitor the sample *in situ* during laser irradiation, as well as to calibrate the spot size of the $785nm$ beam in order to precisely locate the focal position of the other lasers. The sample sits on a mechanical stage which allows for hand-adjustments to the roll and pitch in order to correct for undulations of the sample surface. This stage is attached to a motorized XYZ stage which is used to translate the sample during irradiation and thereby create the desired pattern. The SbSI glasses

were found to oxidize when irradiated. Therefore a custom sample mount was constructed which allows flexible latex tubing to enclose the area surrounding the sample. Nitrogen gas is flowed through the sample mount and into this contained volume in order to limit the oxygen present near the sample. LabView is used to control all of the computerized aspects of the setup.

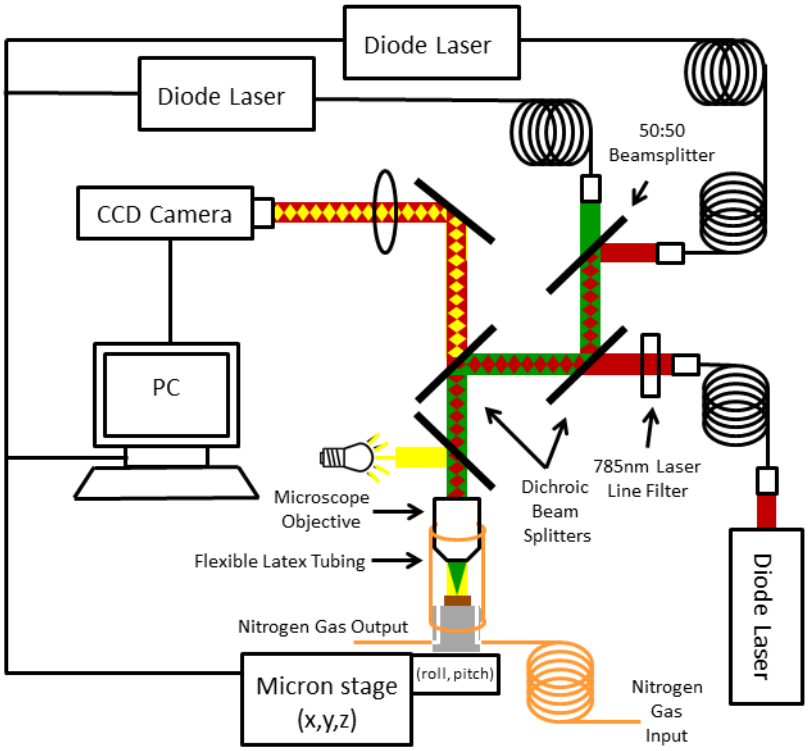

Figure C.1: Diagram of the setup used for CW laser-induced crystallization of SbSI.

Vita

Brian Knorr received a B.S. in Physics from Ramapo College of New Jersey in May 2009. He began his Ph.D. work under the advisement of Professor Volkmar Dierolf in the Physics Department at Lehigh University in May 2010. Since then he was a coauthor on several peer-reviewed journal articles on a variety of different topics. He has accepted a position as an Assistant Professor of Physics at Fairleigh Dickinson University in Madison, New Jersey.